

THESIS

SHEAR STRENGTH AND STIFFNESS OF A SAHARA SAND FROM LIBYA

Submitted by

Mahir Badanagki

Department of Civil and Environmental Engineering

In partial fulfillment of the requirements

For the Degree of Master of Science

Colorado State University

Fort Collins, Colorado

Fall 2011

Master's Committee:

Advisor: J. Antonio H. Carraro

Charles D. Shackelford

Scott Shuler

Copyright by Mahir Badanagki 2011

All Rights Reserved

ABSTRACT

SHEAR STRENGTH AND STIFFNESS OF A SAHARA SAND FROM LIBYA

Modern geotechnical analyses rely upon a rigorous characterization of the dilatancy, critical state and stiffness parameters of geomaterials. In order to generate a fundamental database for these parameters for future geotechnical projects in Libya, the shear strength and stiffness of Libyan Sahara sand were systematically studied in drained and undrained axisymmetric compression. The dry funnel deposition method was employed in this study to create homogenous specimens and simulate the natural fabric of aeolian sand deposits from Libya. The fabric of Sahara sand was examined using a Scanning Electron Microscope (SEM). Static, monotonic, isotropically-compressed drained and undrained triaxial tests were performed on specimens with nominal height and diameter equal to 140 and 70 mm, respectively, to characterize the stress-strain-volumetric (or stress-strain-excess pore pressure) response and determine the intrinsic parameters of Libyan Sahara sand. Bender element tests were also performed to measure the shear wave velocity (V_s) and estimate the small strain shear modulus (G_{max}) of Sahara sand at mean effective stress levels of 50, 100, 200 and 400 kPa.

The intrinsic parameters that characterize isotropic compression, critical-state, dilatancy and small-strain stiffness of Libyan Sahara sand were determined to allow future analyses of mechanical behavior for this soil to be carried out using a rigorous theoretical framework for granular soils. The critical state soil parameters Γ , λ and k of

the Libyan Sahara sand were determined to be equal to 1.92, 0.031 and 0.0002, respectively. The critical state friction angle (ϕ_c) of the soil was found to be equal to 31.9° based on results from both drained and undrained tests. The value of ϕ_c determined from drained tests was found to be in perfect agreement with the value of ϕ_c determined from undrained tests, as expected. The intrinsic parameters Q and R of the peak friction angle (ϕ_p) correlation (Bolton 1986) were determined to be equal to 8.5 and 0.98, respectively. This allowed prediction of ϕ_p values that differed by no more than about 1° from the actual values measured during the triaxial tests performed under a wide range of relative densities and mean effective stresses. The very small strain stiffness parameters C_g , n_g and e_g of the Libyan Sahara sand were equal to 548, 0.51 and 2.17, respectively. While the Libyan Sahara sand tested has about 25% of nonplastic fines, results from this fundamental study suggest that the isotropic compression, critical-state, dilatancy and small-strain stiffness characteristics of this soil can be reasonably interpreted according to (or predicted by) a rigorous framework that has already been validated for clean sands and/or sands containing fines.

DEDICATION

To my beloved mother, Soad

To my father, Abdelgader

To my wife, Ebtihal

To my son, Abdelgader

To my daughter, Soad

To my brother, Saied

To my sisters, Diana and Lina

To the Libyan martyrs who sacrificed themselves for the liberation of Libya from
Gaddafi

ACKNOWLEDGMENT

All praise and thanks are due to God for supporting me complete this work. I also would like to ask him that this project would be another tool to help in the human life.

There is no words can express my deep appreciation and thanks to my advisor Professor J. Antonio H. Carraro for his support, guidance and patience during my study at Colorado State University. Thanks are also extended to Professor Charles D. Shackelford and Professor Scott Shuler for being on the graduate committee for the preparation of this thesis.

Finally, I would like to thank my parents, my wife, my sisters and my brother for the support they provided me during my stay in the United States. Completion of this work would have been difficult without their sincere love and encouragement.

TABLE OF CONTENTS

LIST OF TABLES.....	viii
LIST OF FIGURES	ix
CHAPTER 1: INTRODUCTION.....	1
1.1 Problem Statement.....	1
1.2 Research Objectives.....	3
1.3 Research Scope.....	3
1.4 Manuscript Organization.....	4
CHAPTER 2: Background.....	5
2.1 Aeolion sands Deposits.....	5
2.2 Specimen Preparation.....	7
2.3 Strength and Stress-Strain Response.....	12
2.4 Critical State Soil Mechanics.....	13
2.5 Stress-Dilatancy Relationships.....	17
2.6 Axisymmetric Compression.....	21
2.6.1 Drained Loading.....	23
2.6.2 Undrained Loading.....	25
2.7 Small-Strain Stiffness of Clean and Silty Sands.....	27
CHAPTER 3: EXPERIMENTAL PROGRAM.....	29
3.1 Materials.....	29
3.1.1 Field Sampling and Location.....	29
3.1.2 Particle Size Distribution.....	31
3.1.3 Index Properties.....	32
3.1.4 Scanning Electron Microscopy.....	32
3.2 Experimental Methods.....	36
3.2.1 Specimen Preparation.....	36
3.2.2 Specimen Homogeneity.....	39
3.2.3 Triaxial Apparatus.....	41
3.2.3.1 Flushing.....	41
3.2.3.2 Back Pressure Saturation.....	43
3.2.3.3 Isotropic Compression.....	44
3.2.4 Drained Triaxial Compression.....	44
3.2.5 Undrained Triaxial Compression.....	45
3.2.5.1 Area Corrections for Triaxial Results.....	45
3.2.5.2 Membrane Corrections for Triaxial Results.....	47
3.2.6 Bender Element Testing.....	48
3.2.7 Scanning Electron Microscopy.....	48

CHAPTER 4: ANALYSIS OF RESULTS.....	50
4.1 Specimen Homogeneity.....	50
4.2 Triaxial Response.....	52
4.2.1 Saturation.....	52
4.2.2 Isotropic Compression.....	52
4.2.3 Drained Monotonic Loading.....	55
4.2.4 Undrained Monotonic Loading.....	62
4.2.5 Critical State Friction Angle.....	68
4.2.6 Stress-Dilatancy Relationship.....	71
4.2.7 Comparative Analysis of Specimens of Sahara sand with and without Fines.....	73
4.3 Small-Strain Stiffness.....	76
4.4 Scanning Electron Microscopy.....	80
CHAPTER 5: CONCLUSIONS AND RECOMMENDATIONS.....	81
5.1 Conclusions.....	81
5.1.1 Specimen Preparation.....	81
5.1.2 Isotropic Compression.....	82
5.1.3 Drained Monotonic Response.....	82
5.1.4 Undrained Monotonic Response.....	83
5.1.5 Small-Strain Stiffness.....	83
5.1.6 Intrinsic Parameters of Libyan Sahara sand.....	83
5.1.7 Scanning Electron Microscopy.....	84
5.2 Suggestions for Future Work.....	85
LIST OF REFERENCES.....	87
APPENDIX A: TRANSDUCER CALIBRATION.....	92
APPENDIX B: LIBYAN SAHARA SAND AT START AND END OF SHEARING.....	104

LIST OF TABLES

Table 3.1 Summary of calibration data for instruments.....	42
Table 4.1 Mean and Coefficient of Variation for Loose and Dense Specimens.....	50
Table 4.2 Results for the drained triaxial tests completed on Sahara sand.....	61
Table 4.3 Results for the undrained triaxial tests completed on Sahara sand.....	67
Table 4.5 Comparison of values of ϕ_p predicted using Equation 4.1 with values of ϕ_p measured in individual tests for Sahara sand.....	73
Table 4.6 Results for the drained triaxial tests completed on Sahara sand.....	74
Table 4.7 Shear wave velocity and shear modulus for loose, medium, and dense specimen.....	77
Table A.1 Pressure transducer calibration results.....	94
Table A.2 Calibration data for the Deviatoric Load Transducer.....	96
Table A.3 Calibration data for the Axial Displacement Transducer.....	97
Table A.4 Dimensions of membrane strips used to evaluate the elastic modulus of the membranes.....	102
Table A.5 Data used to determine the modulus of elasticity for the membrane.....	103

LIST OF FIGURES

Figure 1.1 Geological map of Libya (modified after Conant and Gondarzi, 1970)	2
Figure 2.1 Geological map for northern Libya (Al Farrah et al. 2011).....	6
Figure 2.2 Undrained stress-strain response of sand specimens with 12% fines reconstituted by different methods (modified after Vaid et al. 1999).....	8
Figure 2.3 Three dimensional view of the critical state and normal compression lines in q, p', v space (Wood 1990).....	14
Figure 2.4 Influence of initial state of soil on the stress strain and volume change or pore pressure response required to reach the critical state line (Mitchell and Soga 2005).....	16
Figure 2.5 The saw blade model of dilatancy (Modified after Bolton 1986).....	18
Figure 2.6 Axisymmetric compression effective stress paths for drained and undrained triaxial compression tests of Weald clay in (a) q, p' space and (b) v, p' space at low and high mean effective confinement stress (Modified after Wood 1990).....	22
Figure 2.7 Effect of fines plasticity on the stress-strain-volumetric behavior of sands in drained axisymmetric compression (Carraro et al. 2009).....	24
Figure 2.8 (a) Typical stress-strain curves and (b) stress paths from tests on Ottawa sand with 0% and 10% nonplastic silt content, and void ratios around 0.6 (Murthy et al. 2007).....	26
Figure 2.9 Typical stiffness variation and strain ranges (After Atkinson 2000).....	28
Figure 3.1 Location of soil sample.....	30
Figure 3.2 Particle size distribution curves for Libyan Sahara sand.....	31
Figure 3.3 SEM microphotograph of Libyan Sahara sand under X60 magnification.....	33
Figure 3.4 SEM microphotograph of Libyan Sahara sand under X200 magnification.....	34
Figure 3.5 SEM microphotograph of Libyan Sahara sand under X800 magnification.....	35
Figure 3.6 (1) Split mold, (2) Hand-held vibrator, (3) Collar, (4) Cylindrical compaction arm, (5) Rigid steel plug, (6) Surcharge.....	38
Figure 3.7 Set up of the equipments used to create dense specimen.....	39
Figure 3.8 collar apparatus for specimen uniformity checks.....	41
Figure 3.9 Triaxial apparatus used in the study.....	42
Figure 3.10 Scanning Electron Microscope device used in this study.....	49
Figure 4.1 Variation of (a) fines content and (b) relative density over the specimen height.....	51
Figure 4.2 Isotropic compression data for Sahara sand specimens. Values of p' and D_R represent the final specimen state at the end of isotropic compression, before drained shearing.....	53

Figure 4.3 Isotropic compression data for Sahara sand specimens. Values of p' and D_R represent the final specimen state at the end of isotropic compression, before undrained shearing.....	54
Figure 4.4 Deviatoric stress versus axial strain for isotropically consolidated drained triaxial tests. Values of p' and D_R represent the final specimen state at the end of isotropic compression, before shearing.....	56
Figure 4.5 Volumetric strain versus axial strain. Values of p' and D_R represent the final specimen state at the end of isotropic compression, before shearing.....	57
Figure 4.6 Sahara sand specimens in $\ln(p') - v$ space during drained axisymmetric Compression.....	59
Figure 4.7 Drained effective stress paths. Values of p' and DR represent the final specimen state at the end of isotropic compression, before shearing. The two data points for each test correspond to peak and critical state stress states.....	60
Figure 4.8 Deviatoric stress versus axial strain for consolidated isotropically undrained triaxial tests. Values of p' and D_R represent the final specimen state at the end of isotropic compression, before shearing.....	62
Figure 4.9 Axial strain versus excess pore pressure for consolidated isotropically undrained triaxial tests. Values of p' and D_R represent the final specimen state at the end of isotropic compression, before shearing.....	63
Figure 4.10 Undrained effective stress paths. Values of p' and D_R represent the final specimen state at the end of isotropic compression, before shearing. The data point for each test corresponds to critical state stress states.....	65
Figure 4.11 Sahara sand specimens in $\ln(p') - v$ space during undrained axisymmetric compression.....	66
Figure 4.12 CSL in $\ln(p') - v$ space for Sahara sand specimens used to determine the critical state parameters Γ_{cs} and λ_{cs}	69
Figure 4.13 CSL in $p'-q$ space for Sahara sand with a linear best-fit value of M and the corresponding value of ϕ_c	70
Figure 4.14 Visual illustration of best-fit Q and R values for drained triaxial tests on Libyan Sahara sand.....	72
Figure 4.15 Deviatoric stress versus axial strain for consolidated isotropically drained triaxial tests. Values of p' and D_R represent the final specimen state at the end of isotropic compression, before shearing.....	75
Figure 4.16 Volumetric strain versus axial strain. Values of p' and D_R represent the final specimen state at the end of isotropic compression, before shearing.....	76
Figure 4.17 Stiffness degradation response of Libyan Sahara sand in undrained triaxial compression at mean effective stress of $p' = 400$ kPa	77

Figure 4.18 Shear wave velocities with mean effective confinement for loose, medium, and dense specimens.....	79
Figure 4.19 Shear modulus with mean effective confinement for loose, medium, and dense specimens.....	80
Figure A.1 Calibration plot for cell pressure transducer.....	93
Figure A.2 Calibration plot for pore water pressure transducer.....	94
Figure A.3 Calibration plot for the deviatoric load transducer.....	95
Figure A.4 Calibration plot for the axial displacement transducer.....	97
Figure A.5 Regular triaxial cell volume changes with pressure changes (short term)....	99
Figure A.6 Regular triaxial cell volume changes with time (long term).....	99
Figure A.7 Bender element cell volume changes with pressure changes (short term)....	100
Figure A.8 Bender element cell volume changes with time (long term).....	100
Figure B.1 Consolidated drained triaxial specimen at start and end of shearing ($D_R = 88\%$ and $p' = 400\text{kPa}$).....	104
Figure B.2 Consolidated undrained triaxial specimen at start and end of shearing ($D_R = 62\%$ and $p' = 200\text{kPa}$).....	105

CHAPTER 1: INTRODUCTION

1.1 Problem Statement

There is limited data available in the literature on the geotechnical properties of the Sahara sand of Tripoli. Likewise, no fundamental, systematic studies have been done to assess the shear strength and stiffness of Sahara sand from Libya and characterize its stress-strain behavior.

Libya is located in the north-central part of Africa between longitudes $9^{\circ} 50'$ E- 25° E and latitudes $18^{\circ} 45'$ N- 33° N. It is bounded to the north by the Mediterranean Sea, to the east by Egypt, to the west by Tunisia and Algeria, and to the south by Sudan, Chad, and Niger. The approximate area of Libya is $1,775,500 \text{ km}^2$. The capital city is Tripoli (Tarabulus). Paleozoic, Mesozoic, and Cenozoic rocks are exposed in the country, as shown in Figure 1.1. The quaternary deposits of Tripoli consist mainly of fluvio-aeolian sands and silt deposits (Anketell and Ghellali 1991; Schlüter 2006; Tawadros 2001). About 95% of Libya is covered by the Sahara of which 20% rises as sand dunes and it has 1770 km-long coastline bordering the Mediterranean Sea (Ham 2007).

One of the goals of this research is to fill the technical gap encountered in the Libyan geotechnical literature by characterizing the mechanical behavior assessing the shear strength and stiffness parameters of a Sahara sand from Libya.

It is hoped that this study will provide a ready source of reference for geotechnical engineers and companies that wish to obtain a rigorous characterization of the geotechnical properties of the Sahara sand of Tripoli. This may be especially useful given the large volume of construction that is taking place in Tripoli nowadays.

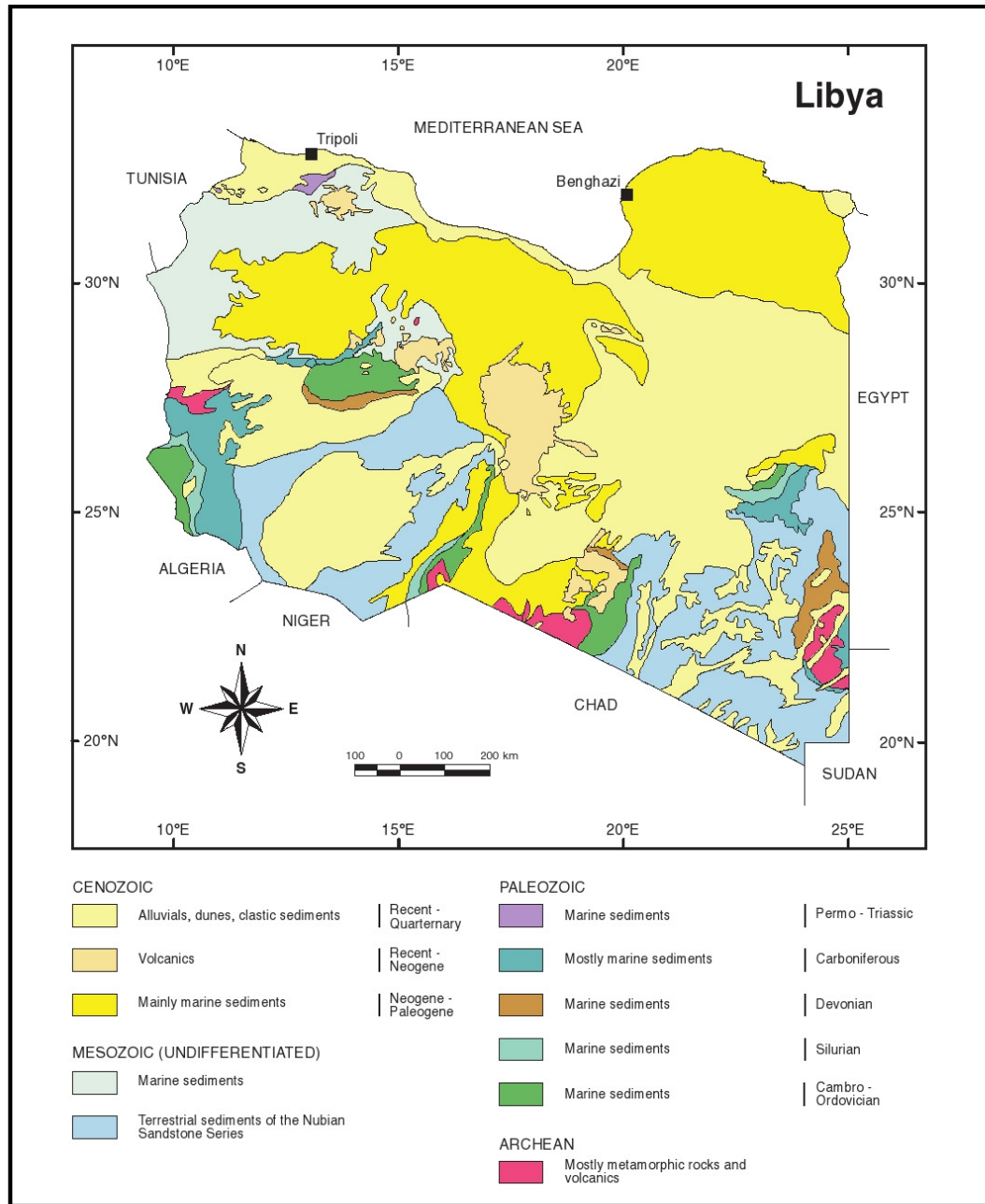


Figure 1.1 Geological map of Libya (modified after Conant and Gondarzi, 1970)

1.2 Research Objectives

The primary objectives of this fundamental study are to study the mechanical behavior of Sahara sand in drained and undrained triaxial compression and to determine its shear strength and stiffness parameters in order to generate a rigorous database for these parameters for future geotechnical projects in Tripoli, Libya. A systematic experimental study was conducted to characterize the mechanical response of the Sahara sand tested. State parameters such as relative density and mean effective stress were varied systematically to study the effect of each parameter on the mechanical behavior of the Sahara sand. As part of the study, a dry funnel deposition technique was used to prepare the specimens of Sahara sand with fines that (1) produces uniform specimens, (2) eliminates the problem of particle segregation, and (3) replicates the natural fabric and stress-strain behavior of Sahara sand deposit formed by wind.

The specific objectives of this study were to:

1. Characterize the stress-strain-volumetric response of Sahara sand in drained and undrained triaxial compression;
2. Evaluate the small-strain shear modulus of Sahara sand;
3. Investigate its intrinsic parameters (e_{\min} , e_{\max} , Γ , λ , k , M , Q , R , C_g , n_g , e_g) and other material properties for this soil.

1.3 Research Scope

This fundamental study focuses on the mechanical behavior of a Sahara sand from Libya containing about 25% of nonplastic silt. An appropriate specimen preparation method was adopted to simulate or mimic the natural deposition processes of Sahara sand

deposits formed by wind. These specimens were then tested in drained and undrained monotonic axisymmetric compression, where the mean effective stress at the end of consolidation was equal to 100, 200 or 400 kPa. Bender element tests were conducted to determine the small strain stiffness. These tests were conducted on samples at four different mean effective confining stresses to characterize the maximum shear modulus at mean effective stresses equal to 50, 100, 200, and 400 kPa.

1.4 Manuscript Organization

Five other chapters are included in this thesis in addition to the Introduction. In Chapter 2, an extensive literature review on silty sand behavior is presented with a focus on desert sands. In Chapter 3, the experimental program used to characterize the mechanical behavior of Sahara sand is described. The results of the experimental program are then presented and discussed in Chapter 4. Finally, Chapter 5 presents the summary and conclusions of this research as well as recommendations for further studies.

CHAPTER 2: Background

2.1 Aeolian Sand Deposits

Aeolian processes, which is a name derived from Aeolus, the Greek God of the winds, are defined as the activity which pertains to wind action. Erosion, transport, and sedimentation are the main groups of aeolian processes arising from the movement of air over the earth's surface (Pye and Tsoar 2009). Erosional processes include (1) deflation of loose sediment because of direct wind draw, (2) entrainment of loose sediment by impaction grains in the wind stream, and (3) abrasion of hard surfaces by particles entrained in the flow. Aeolian transport processes include individual grains movement and the migration of bed forms. Sedimentation processes are associated with individual grains, which involve stabilization of bed forms (Pye and Tsoar 2009).

Aeolian sand deposits cover about 6% of the global land surface area, about 97% of which occur in large arid zone sand seas, and about 20% of the world's arid zones are covered by aeolian sand (Pye and Tsoar 2009). The main categories of aeolian deposits are: (1) sand dunes, which are hills or ridges formed by wind deposition of loose sand; (2) sand sheets, which are combinations of windblown sand that has a gently wavy surface without important development of dune topography; (3) loess blankets, which are deposits of windblown dust containing mainly silt size particles that might be flat, gently wavy, or deeply dissected; (4) fluvio-aeolian deposits, which are interbedded or reworked admixtures of fluvial and aeolian sediments (Pye and Tsoar 2009).

The fluvio-aeolian sands and silt deposits are frequently found in the eastern Jifarah Plain in Libya, both in coastal cliffs and in a number of deeply incised valleys which extend from the mountain to the sea (Anketell and Ghellali 1991). Aeolian deposits appear as sand dunes and sheets covering large areas in the Jifarah plain, as shown in Figure 2.1, as well as patches of the coastal strip (Al Farrah et al. 2011).

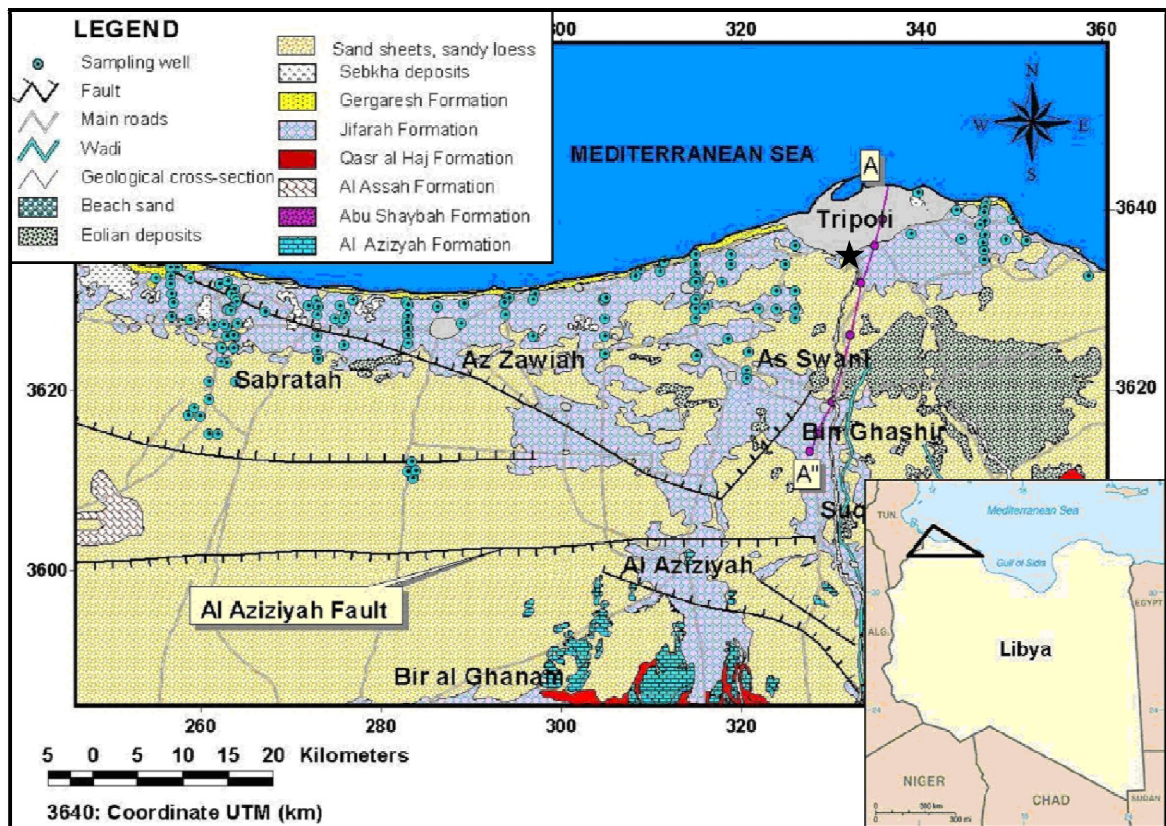


Figure 2.1 Geological map for northern Libya (Al Farrah et al. 2011)

2.2 Specimen Preparation

Most laboratory tests on granular soils are performed on reconstituted specimens due to the fact that obtaining samples of these materials in their undisturbed and natural state is very difficult. Several reconstitution techniques have been developed to reconstitute laboratory soil specimens with fabric similar to the fabric of natural soil deposit in site.

The method of reconstitution used to prepare granular soil specimens in the laboratory strongly affects the structure and the mechanical behavior of the granular soils (Ghionna and Porcino 2006; Vaid et al. 1999; Yamamuro et al. 2008; Yamamuro and Wood 2004). For this reason, the method selected for specimen reconstitution should attempt to simulate the soil fabric and behavior of natural soil deposits as closely as possible. For example, laboratory pluviation methods through air or water might be suitable to mimic natural aeolian or alluvial clean sand deposits (Frost and Park 2003; Vaid and Sayao 1995), respectively. In the case of specimens of sands containing fines, specimen reconstitution becomes a much more critical factor. Figure 2.1 illustrates the typical undrained simple shear response of Syncrude sand specimens at $D_R \approx 44\%$ containing about 12% fines for different techniques of specimen preparation.

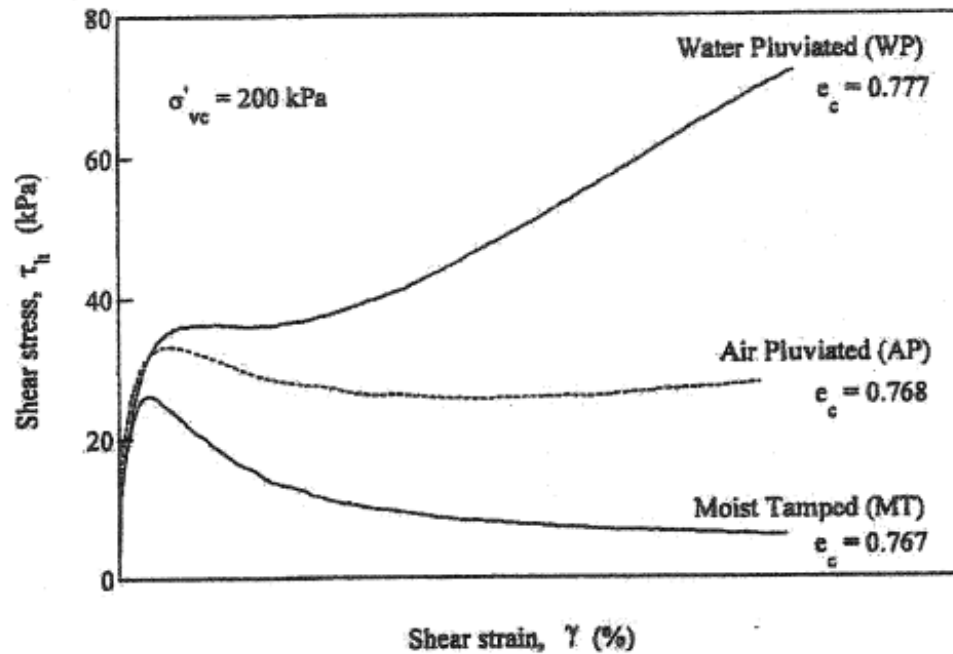


Figure 2.2 Undrained stress-strain response of sand specimens with 12% fines reconstituted by different methods (modified after Vaid et al. 1999)

The figure indicates the technique of specimen reconstitution in the laboratory has a strong influence on the static undrained behavior of sands. The MT specimens of sand may be noted to be the most contractive and shows strain-softening behavior under undrained monotonic triaxial compression. In contrast, the WP does not exhibit any strain softening and behaves dilatively.

The most widely used techniques to reconstitute sands specimens with or without fines are: (1) moist tamping (MT) (Frost and Park 2003; Ladd 1974; Mulilis et al. 1977; Tatsuoka et al. 1986; Ishihara 1993; Jang and Frost 1998); (2) air (or dry) pluviation (AP) (Kuerbis and Vaid 1988; Miura and Toki 1982; Vaid and Negussey 1984b; Rad and Tumay 1987); (3) water (or wet) pluviation (WP) or slurry deposition (SD) (Kuerbis and

Vaid 1988; Carraro and Prezzi 2008;); and (4) dry funnel deposition (DFD)(Bahadori et al. 2008; Ishihara 1993; Lade and Yamamuro 1997; Wood et al. 2008; Zlatovic and Ishihara 1995). Use of MT for sands containing fines has been subjected to some criticism due to the problems associated with reconstituting homogeneous samples, specimen uniformity, and density variations along the specimen height (Mulilis et al. 1977, Frost and Park 2003). Furthermore, loose, saturated specimens using the MT technique for sands containing fines are typically the most contractive (Frost and Park 2003; Thevanayagam et al. 2002; Vaid 1994; Vaid et al. 1999; Jang and Frost 1998).

Moist-tamped specimens are reconstituted by compacting several layers of moist sandy soil into a membrane lined split mold with a circular tamper. This has been found to result in the lower layers of the specimen becoming denser than the top layers if the same compaction effort is applied to all layers (Ladd 1978). Undercompaction was developed to overcome this problem and produce more uniform specimens (Ladd 1978; Mulilis et al. 1975). In this technique, the lower layers are compacted more loosely than the final desired density by predetermined amounts so that the final density of each layer is equal to the target density. Yet, even if the effort of compaction is varied, MT may still produce density variations along the specimen height (Mulilis et al. 1977; Frost and Park 2003). Despite the aforementioned limitations, being able to achieve a wide range of densities during specimen reconstitution is the major advantage of this method.

AP specimens are prepared by raining dry sand particles through air from a controlled height into a membrane-lined mold. This technique is most suitable to mimic the fabric of aeolian deposits of uniform sand or silt (Kuerbis and Vaid 1988). A range of initial relative densities can be achieved by controlling drop height and pouring rate in air

(Vaid and Negussey 1988). The main disadvantage of the AP method is that particle segregation will be present if the specimen is well-graded or has a high fines content (*FC*) (Kuerbis and Vaid 1988). Another disadvantage of AP is the likely need of a long saturation procedure since the initial pore pressure coefficient *B* (Skempton 1954) at zero back pressure (BP) may be as low as 10%-20%. Thus, obtaining a *B* value of 98% or higher may require long periods of time with large BPs.

WP consists of raining dry clean sand into a mold previously filled with de-aired (DA) water (Vaid et al. 1999). WP simulates the fabric and behavior of natural alluvial soils (Oda et al. 1978). WP produces initially saturated specimens (Vaid and Negussey 1988) which in turn will decrease the effort and time required to saturate them. In addition, WP produces uniform clean sand specimens (Kuerbis and Vaid 1988; Vaid et al. 1999). If a higher relative density is desired, it can be obtained by tapping on the side of the mold. Despite these advantages, WP may cause segregation for specimens of sand containing fines (Kuerbis and Vaid 1988).

SD is another commonly used specimen preparation method for sand containing fines (Kuerbis and Vaid 1988). The procedure involves: (1) creating homogenous sand-fines slurry (prepared with DA water) in a mixing tube; (2) placing the mixing tube filled with the slurry vertically inside a mold; and (3) transferring the sample to the saturated mold (Kuerbis and Vaid 1988; Carraro and Prezzi 2008). Dense specimens can be achieved by vibrating the base and side of the mold (Carraro and Prezzi 2008). The major advantages of the SD method are: (1) it reconstitutes homogenous sands specimens containing fines in the laboratory; (2) it produces specimens with a high initial degree of saturation; (3) specimen preparation can be achieved within 2 to 4 h (Carraro and Prezzi

2008); (4) the typical stress-strain response of the specimens simulates the stress-strain response of natural soil deposits formed underwater (Ghionna and Porcino 2006; Vaid et al. 1999). On the other hand, Ishihara et al. (1978) found some problems with this method. They showed an SD technique for silty sand and sandy silt, but their reconstituted specimens with *FC* between 30 and 80% did not result in very homogenous specimens. This method has been validated for sands with nonplastic (Kuerbis and Vaid 1988, Yamamuro and Wood 2004) and plastic (Carraro and Prezzi 2008) fines. Those researchers successfully made uniform specimens using this reconstitution technique.

The DFD technique is commonly used for reconstituting plastic and nonplastic silty sands (Ishihara 1993) and nonplastic silty sand (Lade and Yamamuro 1997; Yamamuro and Lade 1997; Wood et al. 2008; Yamamuro and Covert 2001; Zlatovic and Ishihara 1997). DFD specimens are prepared by initially placing the spout of a funnel filled with uniform silty sand on the bottom of a mold and then slowly raising it along the specimen axis of symmetry. Dense specimens can be achieved by tapping in a symmetrical pattern (Lade and Yamamuro 1997). This method of reconstitution was named tapped funnel deposition (TFD) by Wood et al. (2008). A variation of this technique was later used to reconstitute specimens by raising the funnel faster, which requires less tapping, and this alternative technique is referred to as fast funnel deposition (FFD). The major advantages of this method are: (1) DFD is simple, yet consistent and reliable (Wood et al. 2008); (2) DFD specimens show a smaller degree of segregation (Wood et al. 2008). Despite these advantages, DFD technique can't be used to reconstitute alluvial sand because it does not represent the field's condition.

2.3 Strength and Stress-Strain Response

The stability and life of any structure depend on the strength of the soil. If the soil fails, structures founded on or within it will fail, possibly causing loss of lives and economic damage regardless of how well these structures are designed from a structural engineering point of view. The shear strength of soils is therefore one of the most important aspects for consideration in geotechnical engineering analyses such as the bearing capacity of shallow and deep foundations, slope stability analyses, and retaining wall design.

In modern soil mechanics, the shear strength of soil with strong grains is associated with frictional resistance to sliding and interlocking of soil particles (Schofield and Wroth 1968; Taylor 1948). If dilatancy effects are neglected, the shear strength of soil can be solely associated with the maximum internal frictional resistance to shearing forces (Schofield and Wroth 1968).

The shear strength of an uncemented soil with strong grains can be defined using the Mohr-Coulomb failure criterion with zero cohesive intercept as:

$$s = \sigma' \tan \phi$$

where s = shear strength

σ' = normal effective stress on the plane of shearing

ϕ = friction angle

Casagrande conducted consolidated drained triaxial tests on both loose and dense sands and concluded in 1937 that loose sand exhibited contractive behavior, while dense sands showed dilative behavior, which nowadays can be incorrect due to other factors, such as confining pressure. He also performed undrained triaxial tests with pore water

pressure measurements during these days of geotechnical engineering development (Casagrande 1975). In general, dense sands tend to show peak shear stresses and expand. Loose sands, on the other hand, do not show peak shear stresses except at very low normal effective stresses, and they tend to contract. The extent of contraction or dilatancy depends on the combined effect of density and effective confining stress (Schofield and Wroth 1968).

2.4 Critical State Soil Mechanics

In this study the critical state soil mechanics framework was used to analyze and define the mechanical behavior of the consolidated isotropically drained and undrained triaxial tests on specimens of Sahara sand. The critical state is defined as the state at which the soil continues to shear without further changes in the deviatoric stress, mean effective stress, and volume. One important characteristic of critical state soil mechanics is that it includes the volume change in the failure criterion, unlike the traditional Mohr-Coulomb failure, which gives only a stress value for failure along a shear plane (Budhu 2007). The main idea in the critical state concept is that all soils have a unique failure line that exists in q, p', v space, where q is the deviatoric stress $= \sigma_1 - \sigma_3$, p' is the mean effective stress $= \frac{\sigma_1 + 2\sigma_3}{3}$, and v is the specific volume $= 1 + e$, which will control soil behavior at large strains after removing the effect of initial soil state (Schofield and Wroth 1968).

The critical state line (CSL) can be represented in three-dimensional space, as shown in Figure 3.1. The CSL becomes a critical state surface in (q, p', e) space (Budhu 2007). According to Schofield and Wroth (1968), the failure surface is typically

represented by projecting the CSL onto two axes, where two simple equations can be employed to determine the failure conditions:

$$q = M p' \quad \text{Equation 2.1}$$

$$v = \Gamma + \lambda \ln p' \quad \text{Equation 2.2}$$

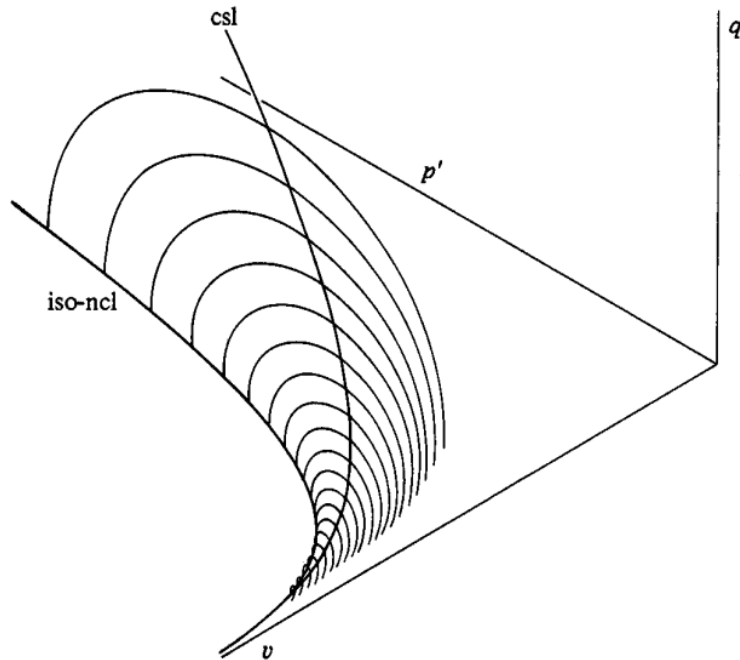


Figure 2.3 Three dimensional view of the critical state and normal compression lines in q , p' , v space (Wood 1990)

where M , Γ , and λ are critical state soil parameters. The M parameter defines the stress ratio q/p' that represents the slope of the critical state line in (q, p') space, which is related to the critical state friction angle of the soil (ϕ_c). The λ parameter relates to the slope of the critical state line in $(e, \ln p')$ space, which is assumed to be parallel to the normal consolidation line. The Γ parameter is the specific volume intercept at unit reference

stress ($p'=1$) in ($e, \ln p'$) space (Schofield and Wroth 1968). For triaxial compression, the relationship between M and ϕ_c is given by:

$$\sin \phi_c = \frac{3M}{6+M} \quad \text{Equation 2.3}$$

Figure 2.4 briefly explains the uniqueness of the critical state line (Mitchell and Soga 2005). The figure illustrates the existence of a unique critical state for any soil for a given mode of deformation. If the soil is on the critical state line, there is no change in volume or pore pressure during shear deformation. When the soil has an initial state above and to the right of the critical state line (“wet” of critical state), the soil contracts during shear at a slow strain rate, or positive pore pressures will be generated if the soil is sheared at a rapid strain rate. On the other hand, if the soil has an initial state below and to the left of the critical state line (“dry” of critical state), the soil dilates during shear at a slow strain rate, or negative pore pressures will be generated if the soil is sheared at a rapid strain rate.

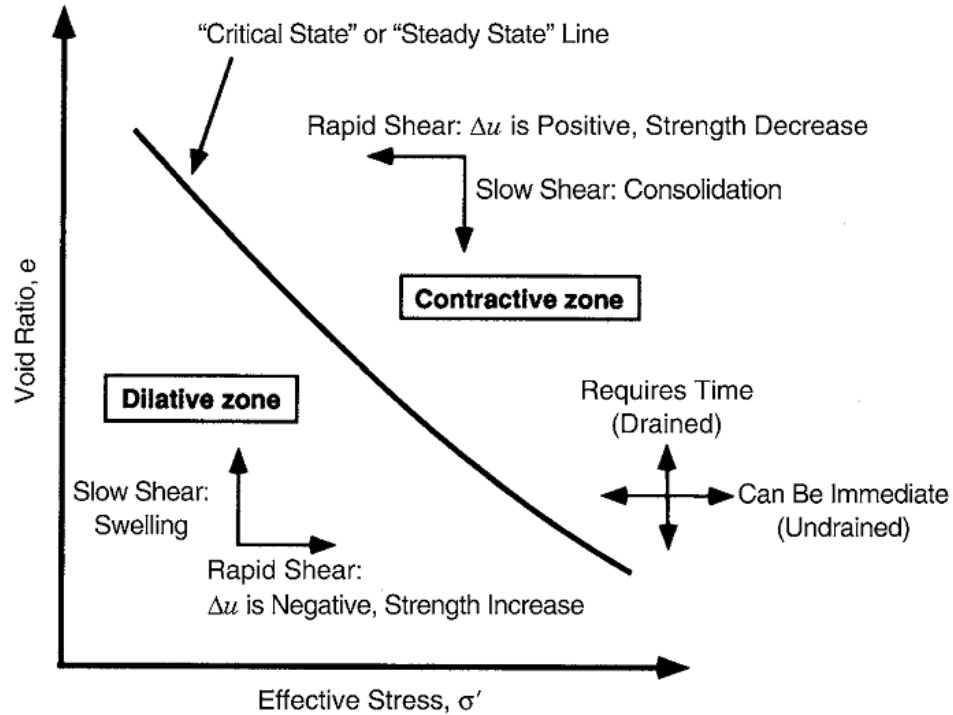


Figure 2.4 Influence of initial state of soil on the stress strain and volume change or pore pressure response required to reach the critical state line (Mitchell and Soga 2005)

Under drained conditions, if a loose sample is sheared under high effective confining stress, the shear stress increases monotonically until it reaches a plateau, then the sample continues to undergo shear straining without any change in shear stress or volume of sample. The sample is then said to have attained the critical state, and the corresponding friction angle is referred to as the critical-state friction angle ϕ_c . On the other hand, dense sand specimens may contract initially and then dilate upon shearing depending upon the initial soil state. The critical-state friction angle acquired from triaxial tests is commonly taken as a unique value for a given granular soil, regardless of the initial relative density and initial confining stress (Schofield and Wroth 1968).

Under undrained conditions, strain softening response is observed for loose specimens, whereas strain hardening is often observed for dense specimens. If a loose sample is sheared under low effective confining stress, the strength of the soil increases with shearing until reaching peak strength. After reaching the peak, the strength of the soil reduces towards a constant value (Ishihara et al. 1975). On the other hand, dense sand specimens do not exhibit any loss of strength during shearing and develop initially positive excess pore pressure and then it develops large negative excess pore pressure (Ishihara et al. 1975). Dense sand specimens may therefore show contractive behavior initially and dilative behavior at large strain level. The undrained behavior of sand specimens is highly dependent on fabric, and hence the specimen reconstitution method can significantly affect the type of response (Vaid et al. 1999).

2.5 Stress-Dilatancy Relationships

Soil dilatancy refers to the change in volume that is associated with shear deformation. This idea was first studied in 1885 by Osborne Reynolds. He found that dilative sands increase in volume during shearing. Taylor (1948) found that the shear strength of soil is associated with two components: frictional resistance between grains, which is a combination of rolling and sliding friction, and interlocking. According to Taylor (1948), volume change occurs in soils due to interlocking, which causes dilation in dense sands and contraction in loose sands.

Stress-dilatancy relationships describe the relation between the friction and dilatancy angles ϕ and ψ , respectively (Salgado et al. 2000). Figure 2.5 illustrates the concept of dilatancy through the saw-blade model. During shearing, slippage takes place

when friction between two blocks is overcome and the two blocks move apart. When the shear force is increased, the sand particles roll over one another, and volume change must occur if the shearing is to be continued in the horizontal direction.

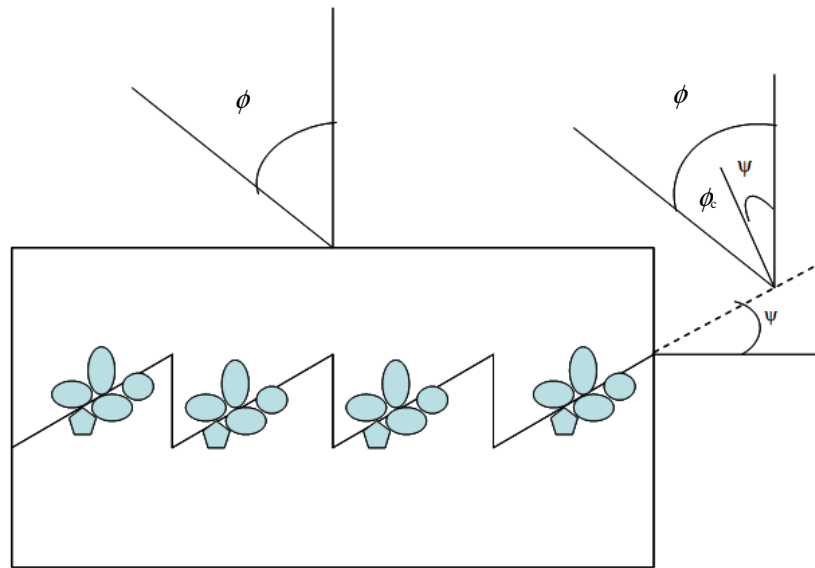


Figure 2.5 The saw blade model of dilatancy (Modified after Bolton 1986)

A simple view of the friction-dilatancy relation in plane-strain loading conditions, which does not account for the direction of the principal stress and strain increments, may be expressed as follows (Bolton 1986):

$$\phi = \phi_c + \psi \quad \text{Equation 2.4}$$

Where ϕ is the effective friction angle, ϕ_c is the critical state friction angle, and ψ is the dilatancy angle.

De Josselin de Jong (1976) proved that the same relation can be derived without resorting to the energy minimization principle by relying on friction laws. According to Salgado et al. (2000), the theory is superior to all other attempts to relate shear strength to dilation and can be best expressed in the form:

$$N = M \cdot N_c \quad \text{Equation 2.5}$$

where N = flow number = σ'_1/σ'_3 = stress obliquity; N_c = critical-state flow number = $(\sigma'_1/\sigma'_3)_c$ = stress obliquity at critical state; M = dilatancy number = $1 - d\varepsilon_p/d\varepsilon_1$; $d\varepsilon_p$ = volumetric strain increment; and $d\varepsilon_1$ = major principal strain increment = axial strain increment in triaxial compression tests. N , M , and N_c are given in terms of ϕ , ϕ_c and ψ by the following expressions:

$$N = \frac{1 + \sin \phi}{1 - \sin \phi} = \tan^2 \left(45^\circ + \frac{\phi}{2} \right) \quad \text{Equation 2.6}$$

$$N_c = \frac{1 + \sin \phi_c}{1 - \sin \phi_c} = \tan^2 \left(45^\circ + \frac{\phi_c}{2} \right) \quad \text{Equation 2.7}$$

$$M = \frac{1 + \sin \psi}{1 - \sin \psi} = \tan^2 \left(45^\circ + \frac{\psi}{2} \right) \quad \text{Equation 2.8}$$

The dilatancy angle is defined as

$$\sin \psi = - \frac{\frac{d\varepsilon_1}{k \cdot d\varepsilon_3} + 1}{\frac{d\varepsilon_1}{k \cdot d\varepsilon_3} - 1} \quad \text{Equation 2.9}$$

where $d\varepsilon_1$ and $d\varepsilon_3$ = principal strain increments; $k = 1$ for plane strain and 2 for triaxial test conditions.

Bolton (1986) compared Equation 3.4 with Rowe's stress-dilatancy relation for plane strain for typical quartz sand and, after analyzing a large dataset for quartz sands, found that an overestimation of about 20% results for values of $\phi - \phi_c$. Based on this observation, he suggested a simpler relationship between ϕ , ϕ_c and ψ as follows:

$$\phi = \phi_c + 0.8\psi \quad \text{Equation 2.10}$$

Bolton (1986) conducted a detailed analysis of the strength and dilatancy of 17 quartz sands in axisymmetric and plane strain conditions at different densities for various confining pressures, and he extended that relationship to determine for both triaxial and plane-strain conditions, as follows:

$$\phi_p - \phi_c = b \cdot I_R \quad \text{Equation 2.11}$$

where ϕ_p is the peak-friction angle, b is equal to 3 or 5 for triaxial or plane strain conditions, respectively, and I_R is the relative density index given by:

$$I_R = \frac{D_R}{100} \left(Q - \ln \frac{100 \cdot p'_p}{p_A} \right) - R \quad \text{Equation 2.12}$$

where D_R = relative density of the soil (%); p'_p = mean normal effective stress at peak strength; p_A = reference stress (=100 kPa) in the same units as p'_p ; and Q and R =intrinsic parameters of the soil. Bolton's empirical relation is valid for dilatancy angles between 0 and 20° and I_R between the values of 1 and 4. Bolton's relation is used in this thesis also to estimate ϕ_p and then compare it to ϕ_p that was measured from the actual triaxial tests.

2.6 Axisymmetric Compression

Consolidated isotropically drained and consolidated isotropically undrained are the two axisymmetric compression test methods that will be discussed in this section. There have been several studies presented in the literature that examined the drained and undrained axisymmetric compression behavior of clean sands and pure clays. According to Carraro 2004, there are very few systematic studies on a combination of these two materials (plus silt and gravel) due to the fact that specimen reconstitution and testing of these soils involves additional experimental difficulties.

Figure 2.6 shows the typical behavior and the expected stress paths for drained and undrained axisymmetric compression tests at low and high mean effective stresses on Weald clay. It serves as an idealized representation of the critical state framework with real data that can be capable of predicting soil response in triaxial compression. All tests performed come close to reaching the CSL in Figure 2.6 (a), which is illustrated by the dashed line. At large strains, all test results will converge to a unique CSL.

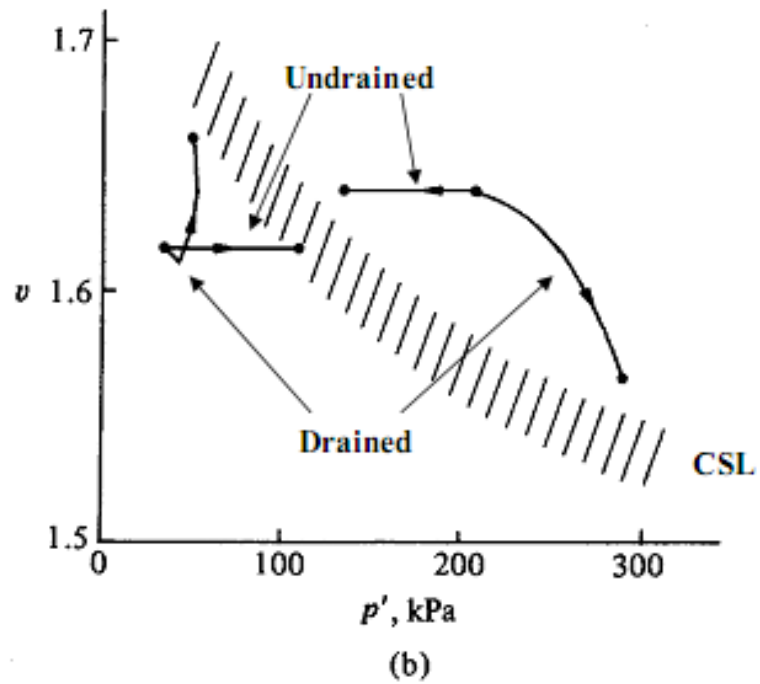
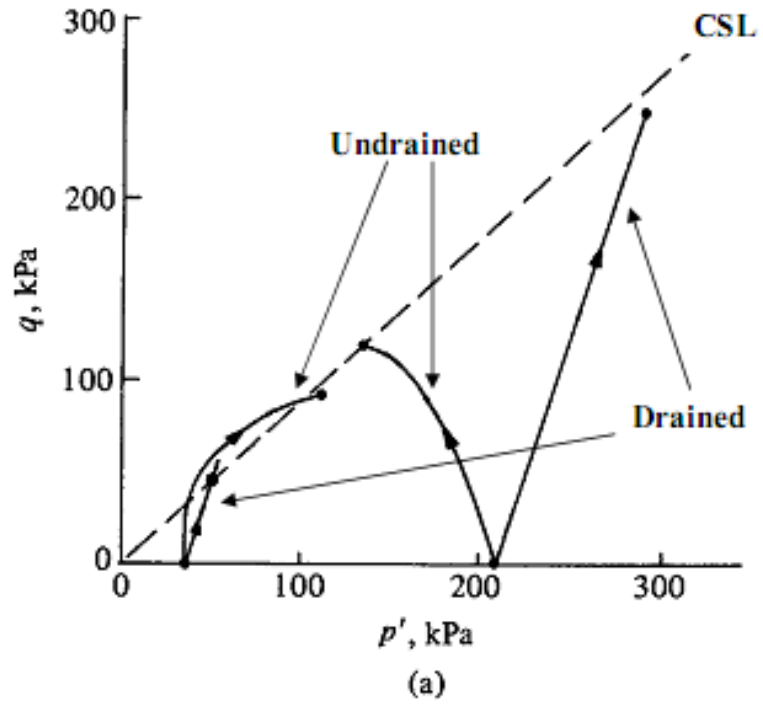


Figure 2.6 Axisymmetric compression effective stress paths for drained and undrained triaxial compression tests of Weald clay in (a) q, p' space and (b) v, p' space at low and high mean effective confinement stress (Modified after Wood 1990)

In drained triaxial compression tests, the effective stress paths in q, p' space have 3:1 slope during the shearing stage and no development of excess pore water pressure. On the other hand, for undrained triaxial compression tests, the effective stress paths in q, p' space vary based on the excess pore water pressures generated during shearing which is related to the soil state (Budhu 2007). In v, p' space, the effective stress paths change based on the contraction or dilatancy behavior of the soil during the drained compression test. For the undrained compression test, the effective stress paths have a zero slope and no volume change during shearing (Wood 1990). The effects of drainage conditions on the triaxial compression response of materials similar to the ones tested in the present study are summarized next.

2.6.1 Drained Loading

Figure 3.5 shows typical stress-strain-volumetric drained behavior of sands containing fines in axisymmetric compression. Carraro et al. (2009) performed 72 drained static monotonic triaxial compression tests on Ottawa sand containing various amounts of nonplastic silt or kaolin clay to investigate the effects of the fines on the stress-strain-volumetric behavior. They found that both the peak and critical-state friction angles continuously increase with increasing nonplastic silt content due to the interaction of nonplastic silt with irregularities on the sand particles surface, which mostly leads to dilative behavior at high D_R and relatively low p' . Conversely, addition of the same amount of kaolin clay to the host sand decreases both the peak and critical-state friction angles of the soil because the clay particles would tend to lubricate or “oil” the defects and asperities on the surfaces of the sand particles and provide an intergranular

matrix that is intrinsically more contractive than its nonplastic silt counterpart and lead to contractive behavior. Also, Salgado et al. (2000) studied the effects of nonplastic fines on the shear strength of sands using drained triaxial tests on isotropically consolidated specimens. It was found that the addition of even small percentages of nonplastic silt to clean sand increases both the peak and the critical-state friction angles at a given initial relative density and stress state.

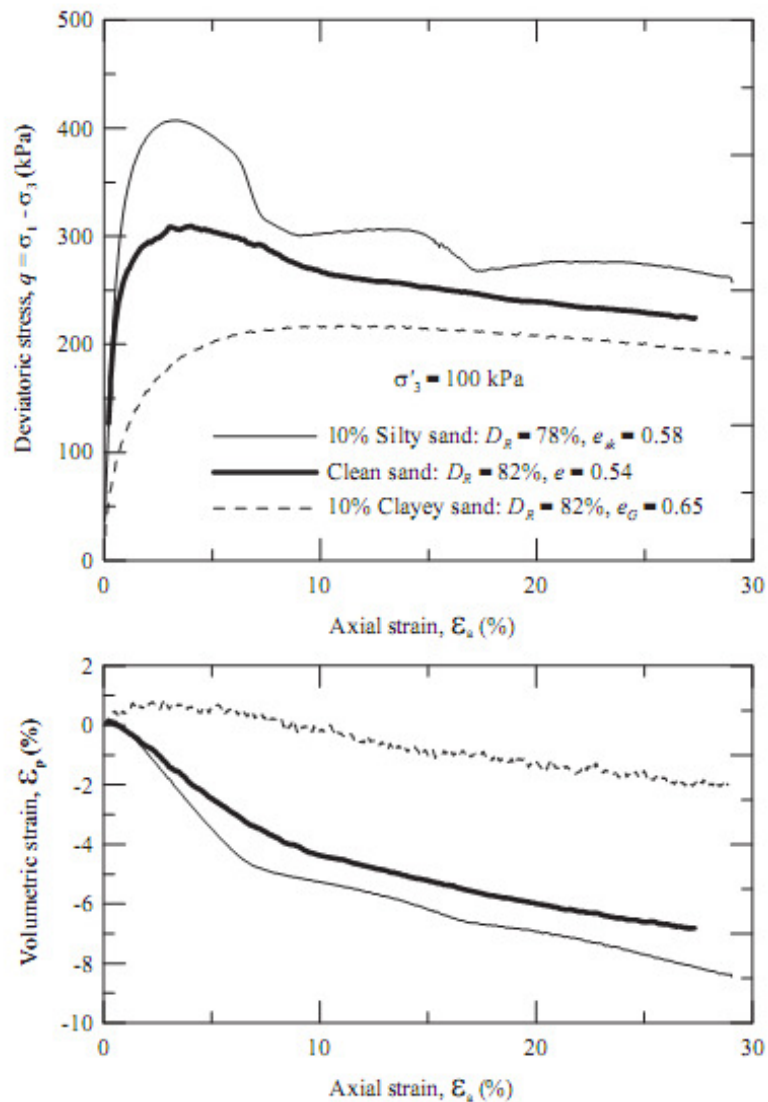


Figure 2.7 Effect of fines plasticity on the stress-strain-volumetric behavior of sands in drained axisymmetric compression (Carraro et al. 2009)

2.6.2 Undrained Loading

The main difference between drained and undrained triaxial compression tests is that, for drained triaxial compression tests, volume change can occur, whereas, for undrained triaxial compression tests, no volume change can occur. Figure 2.8 illustrates the typical stress-strain-volumetric undrained behavior of sands containing nonplastic silt in triaxial compression.

Murthy et al. (2007) carried out 59 undrained monotonic triaxial compression tests on mixtures of Ottawa sand with non plastic silt to study the monotonic undrained response of such sands containing 0, 5, 10 and 15% of non plastic silt. They found that the critical state from undrained tests is in agreement with that found from drained tests. Also, They found that increasing the nonplastic fines content leads to a downward shift of the critical-state line and an increase in the critical-state friction angle. The typical test results from their study are presented in Figure 2.8.

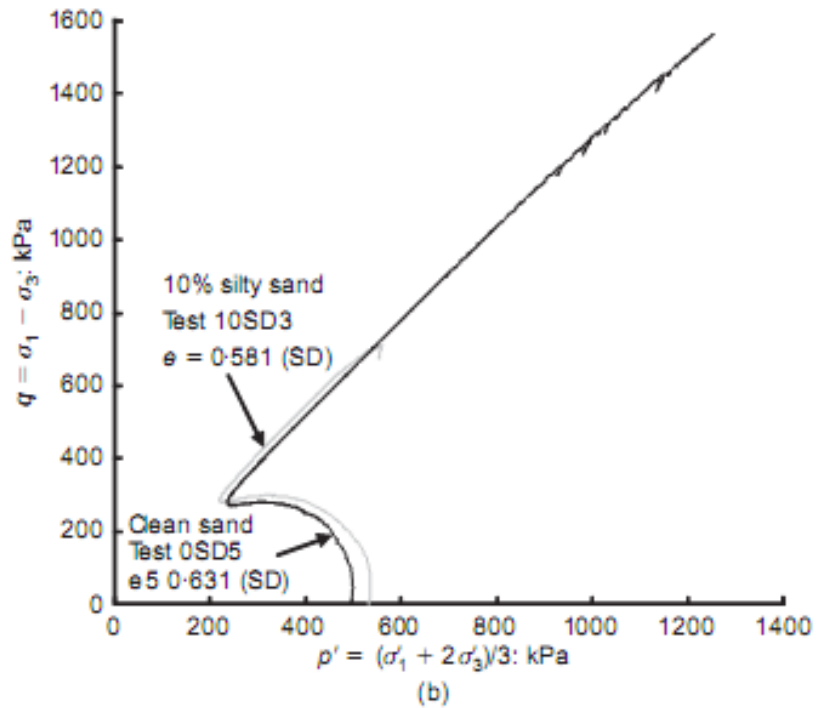
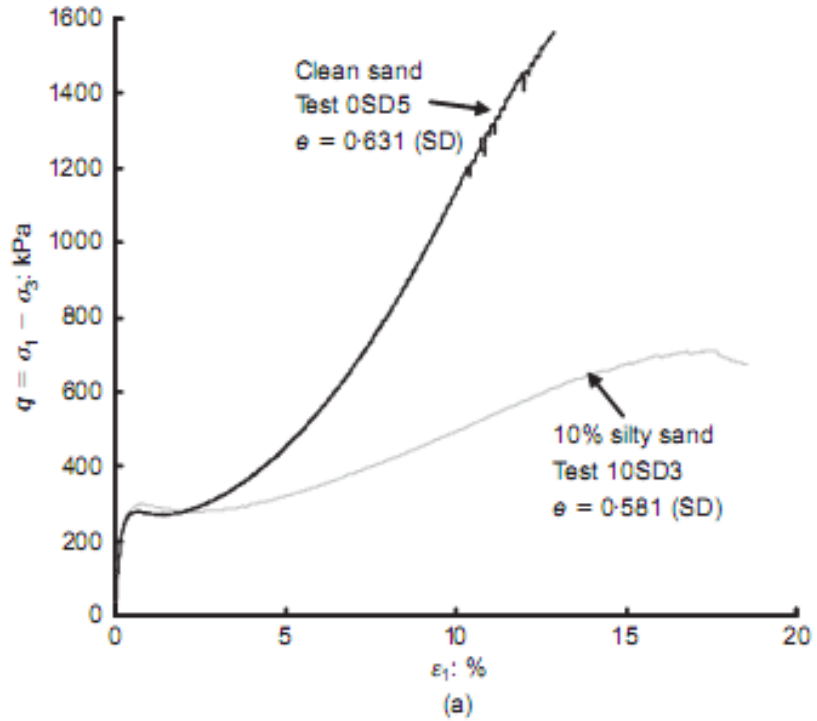


Figure 2.8 (a) Typical stress-strain curves and (b) stress paths from tests on Ottawa sand with 0% and 10% nonplastic silt content, and void ratios around 0.6 (Murthy et al. 2007)

2.7 Small-Strain Stiffness of Clean and Silty Sands

The stiffness at very small strains of a soil is associated with the range of strain where linear elastic response is observed. The stiffness of soil at these strains can be measured by dynamic laboratory techniques. The maximum shear modulus (G_{\max}) may, for practical purposes, be considered constant at very small strains, but then it decreases with increasing shear strain by orders of magnitude (Atkinson 2000). Figure 3.3 illustrates a typical stiffness-strain curve for soil that can be measured using dynamic methods, local gages and conventional gages.

The shear modulus of a soil is an important parameter to analyze various types of geotechnical design applications, including foundation stability for superstructures and deep foundation systems, soil-structure interaction during earthquakes, and machine foundation design (Gazetas, 1982; Dyvik and Madshus 1985)

The common methods for measuring G_{\max} in the laboratory are the resonant column and bender elements techniques. The bender element test is much simpler and more direct than the resonant column test (Dyvik and Madshus 1985). The maximum shear strains generated by the passage of a shear wave are on the order of 0.001%, which is well within the elastic range for soils, and it can therefore be concluded that the bender element method can be used to assess the maximum shear modulus (G_{\max}) for the soil (Dyvik and Madshus 1985). The mapping of the two extremes of the stiffness variation curve can be done by determining both the small strain shear modulus from bender element tests and the large strain stiffness from conventional displacement transducers used in triaxial tests.

In the bender element test, a shear wave is generated at one end of the specimen and its arrival time measured at the other end. The shear wave velocity can be calculated from the consolidated length of the soil specimen and travel time, and it is related to the maximum shear modulus (Viggiani and Atkinson 1995b) according to:

$$G_{\max} = \frac{\gamma}{g} V_s^2 \quad \text{Equation 2.13}$$

where γ is the total unit weight of the soil, V_s is the shear wave velocity, and g is the acceleration of the Earth's gravity.

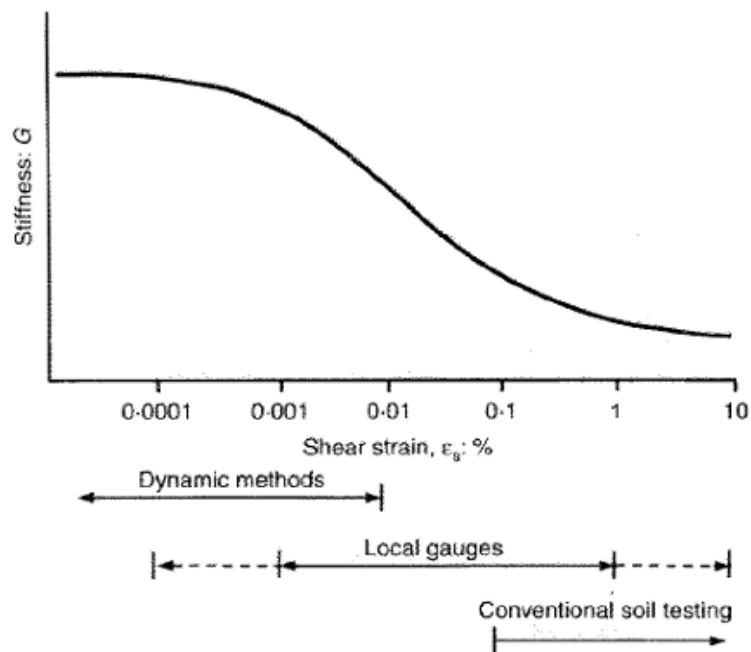


Figure 2.9 Typical stiffness variation and strain ranges (After Atkinson 2000)

This approach has been employed by many researchers (Dyvik and Madshus 1985; Viggiani and Atkinson 1995a,b; Salgado et al. 2000; Carraro 2009), and it is also employed in the present study.

CHAPTER 3: EXPERIMENTAL PROGRAM

3.1 Materials

3.1.1 Field Sampling and Location

The Sahara sand sample used in this study was collected from Tripoli, in north western Libya ($32^{\circ} 51' 05.67''$ N and $13^{\circ} 13' 19.92''$ E), as shown in Figure 3.1. A 45 kg bulk sample of Sahara sand was collected from depths between 0.5 m and 1.0 m below the ground surface. The sample was shipped via express mail from Tripoli, Libya to Colorado State University's geotechnical laboratory.

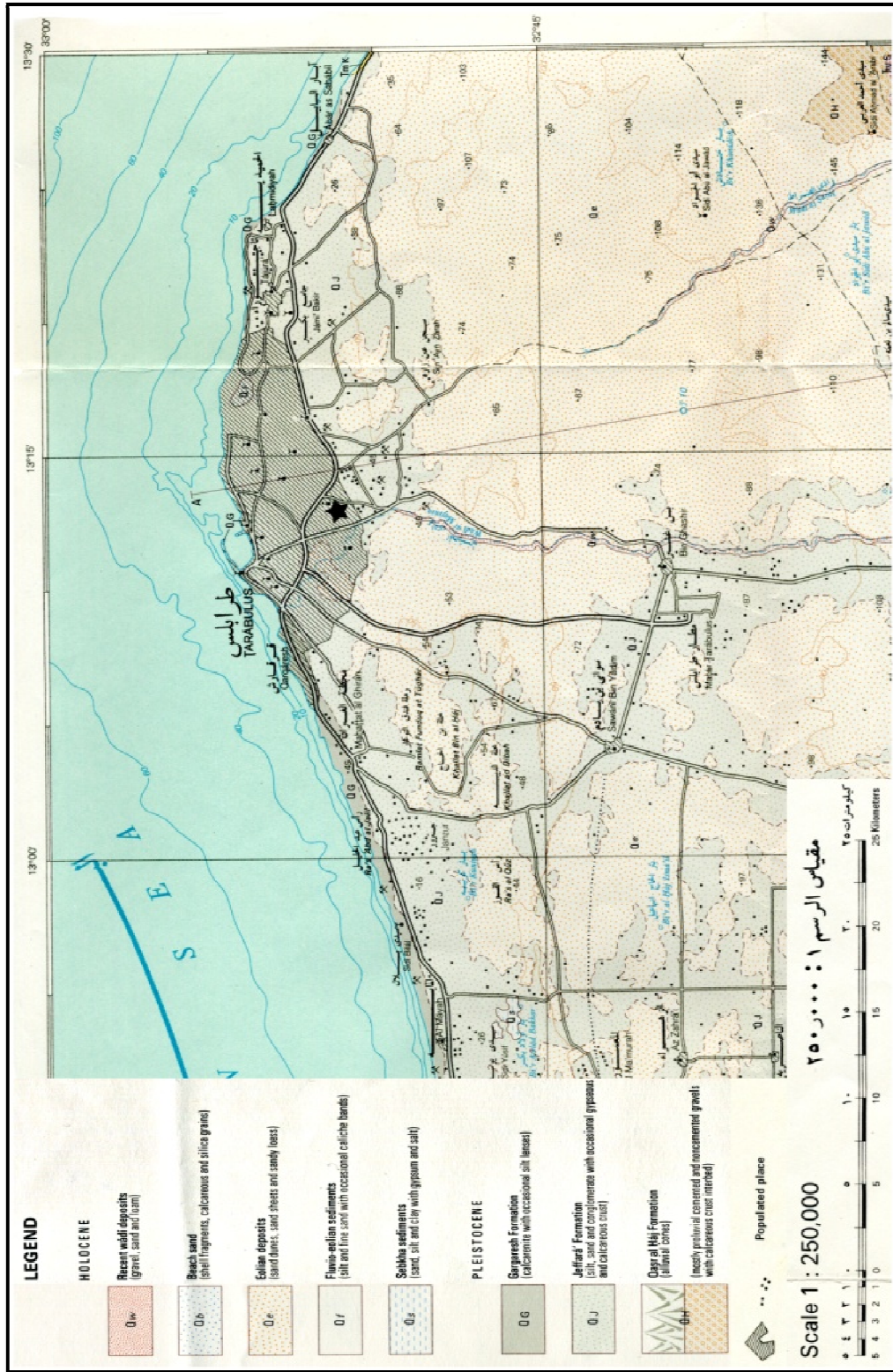


Figure 3.1 Location of soil sample

3.1.2 Particle Size Distribution

The grain size distribution of Sahara sand was determined from both sieve and hydrometer analyses and it is presented in Figure 3.2. The grain size distribution resembles that of a uniform poorly-graded sand with fines. Most particles were retained on #200 sieve. The majority of the particles had diameters between 0.075 and 0.150 mm. Based on the grain size distribution curve, shown in Figure 4.1, the mean grain size D_{50} is 0.10 mm, the coefficient of uniformity C_u is 1.83, the coefficient of curvature C_c is approximately 0.97, and the fines content FC is 24.8%.

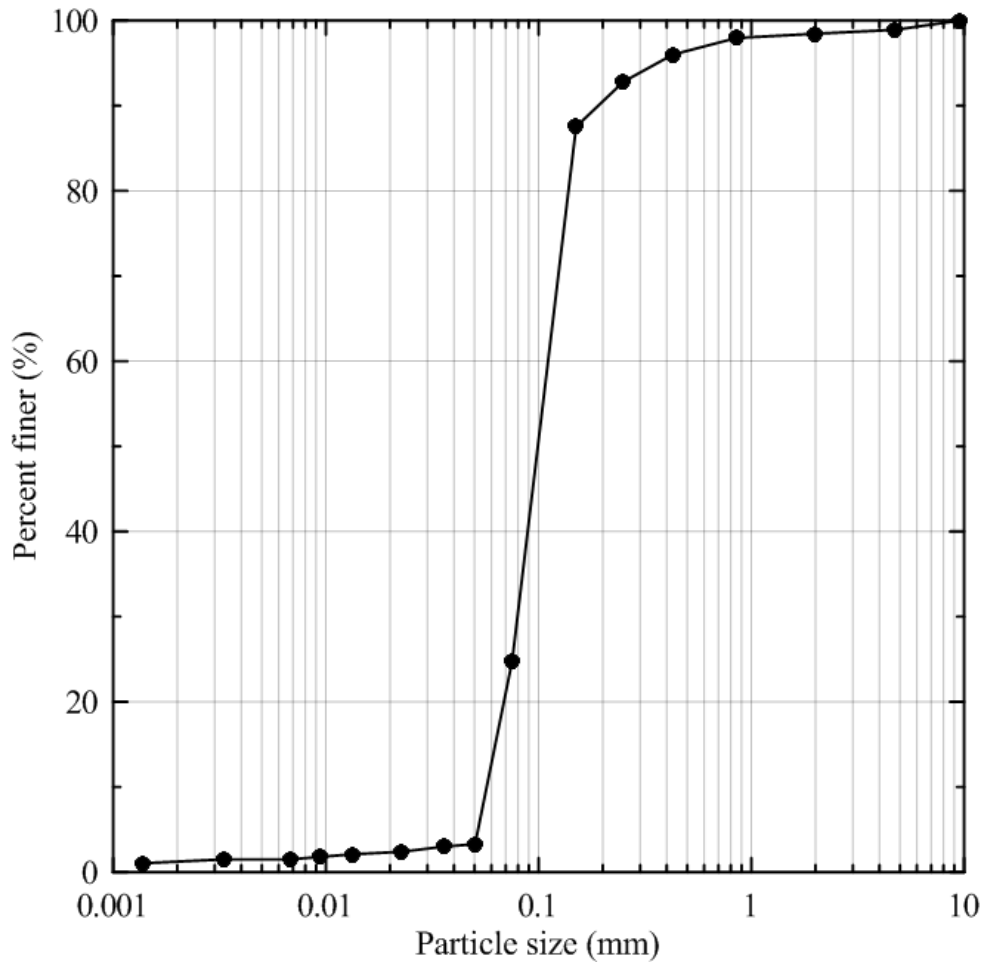


Figure 3.2 Particle size distribution curves for Libyan Sahara sand

3.1.3 Index Properties

The specific gravity (determined according to ASTM D 4318), the maximum void ratio (determined according to ASTM D 4254) and the minimum void ratio (determined according to ASTM D 4253) of the soil are 2.63, 0.951, and 0.633, respectively. The liquid limit could not be determined and the soil is nonplastic. The soil is classified as poorly-graded sand with nonplastic silt (SM), according to the Unified Soil Classification System (USCS) (ASTM D 2487).

3.1.4 Scanning Electron Microscopy

The particle shape and fabric of the Sahara sand sample were examined using a scanning electron microscope (SEM). A microphotograph of the Sahara sample is shown in Figures 3.3, 3.4, 3.5 with magnifications equal to 60, 200 and 800, respectively. It was found that some of the particles were angular particles and most of them were round to sub rounded particles, according to Mitchell and Soga (2005).

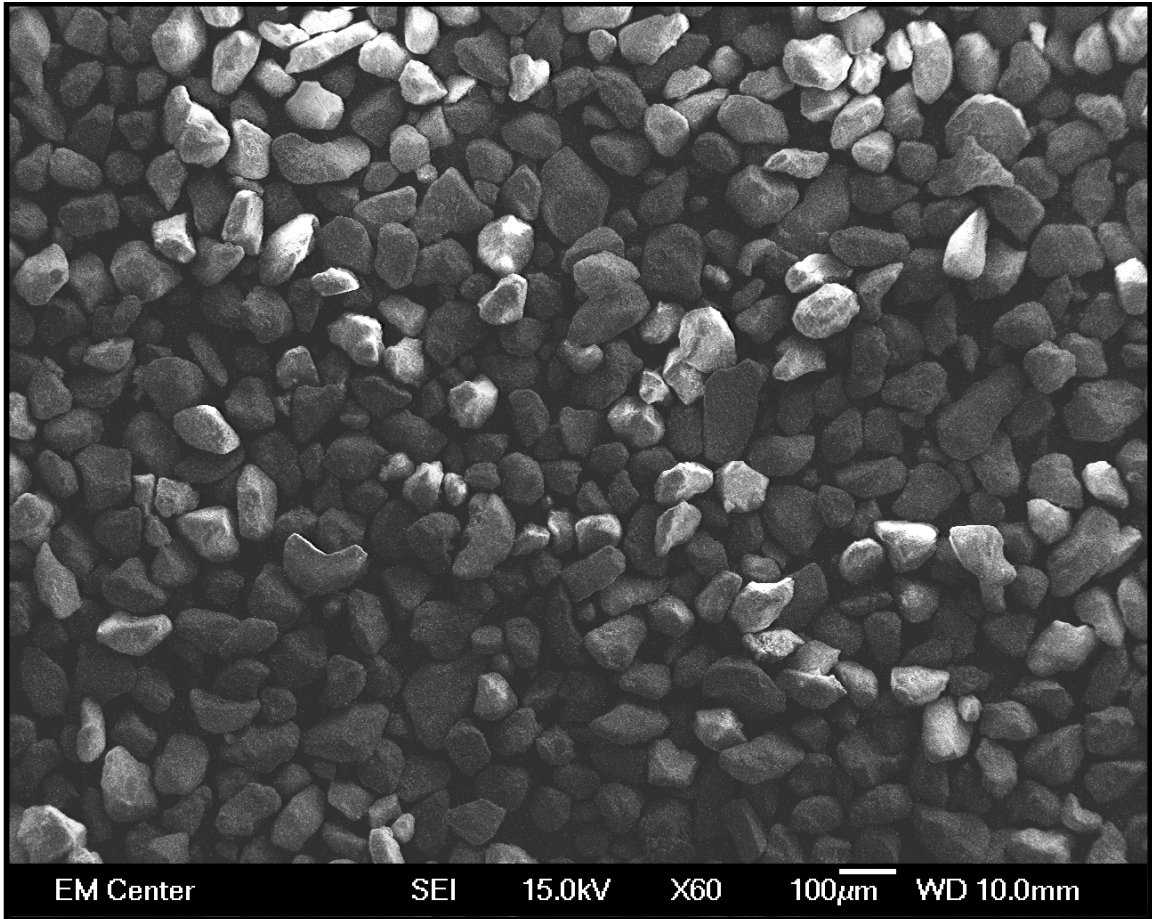


Figure 3.3 SEM microphotograph of Libyan Sahara sand under X60 magnification

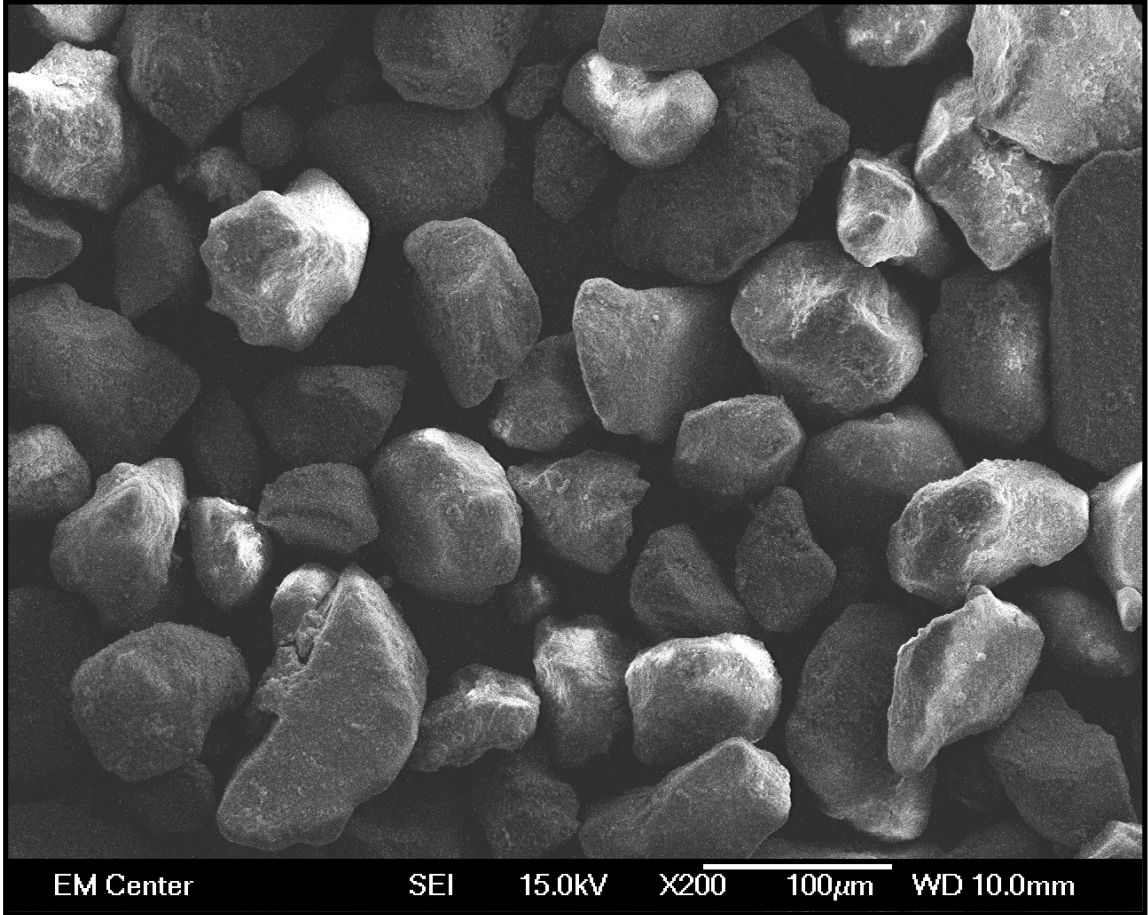


Figure 3.4 SEM microphotograph of Libyan Sahara sand under X200 magnification

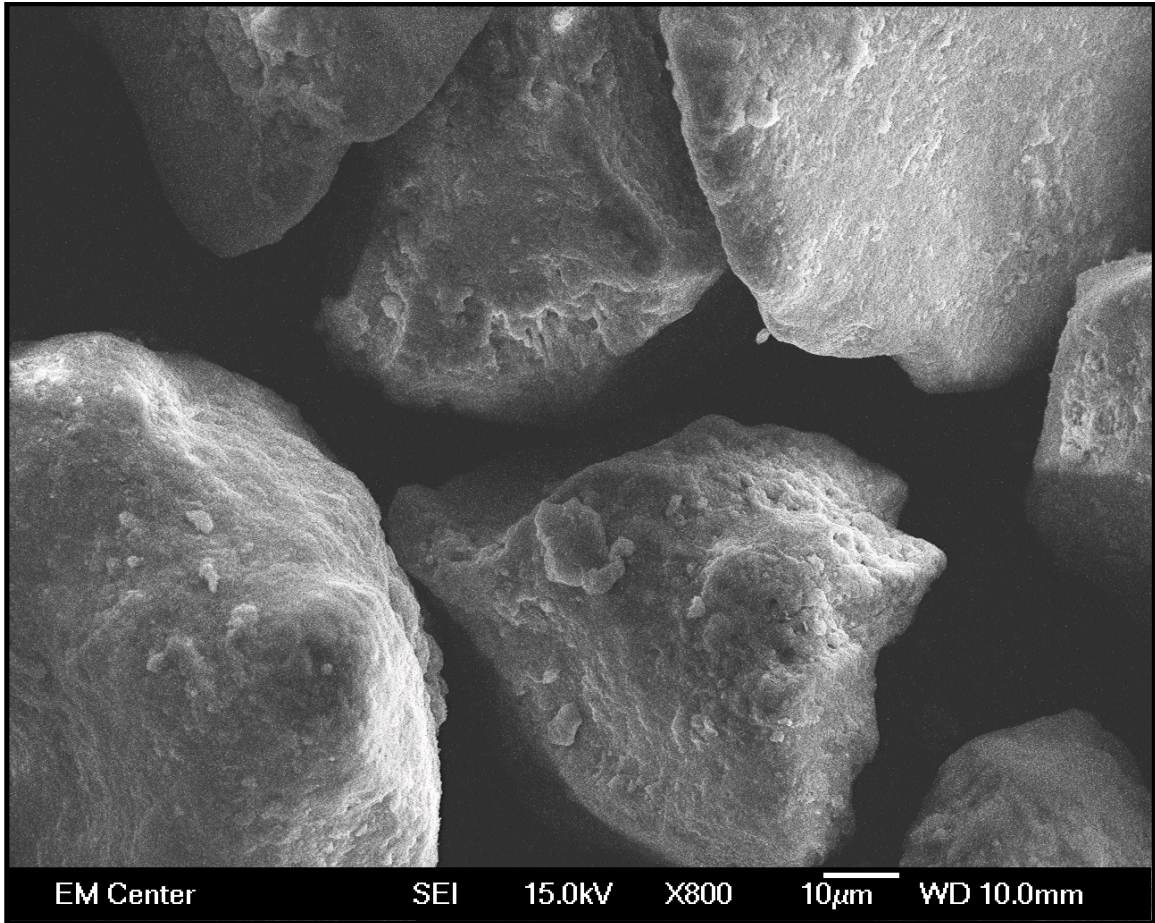


Figure 3.5 SEM microphotograph of Libyan Sahara sand under X800 magnification

3.2 Experimental Methods

3.2.1 Specimen Preparation

In an effort to simulate the natural fabric Libyan aeolian sand deposits, the dry funnel deposition method (Wood et al. 2008) was employed in this study to create homogenous loose specimens. In order to achieve higher densities, the method was slightly modified by using vibration as it is explaining in more details below. The steps employed in the specimen reconstitution procedure consist of the following:

1. The split mold is installed on the base of the triaxial test cell over a 70-mm-diameter and 0.3-mm-thick latex membrane that is secured in the bottom with three O-rings. A porous stone and filter paper are placed at the bottom of the mold before adding the Sahara sand in the mold. A vacuum of 30-kPa is applied between the membrane and the mold wall.
2. To create a loose specimen, the spout of a funnel is initially placed on the bottom of the split mold. Then the Sahara sand is placed into the funnel and the funnel is slowly raised along the specimen axis of symmetry. This allowed the sand to be deposited in a low-energy state without any drop in height. Once the mold is filled, a steel straightedge is used to level the surface of the soil with the top of the mold.
3. To create a medium level of density, a collar is placed on the split mold top, then the spout of a funnel is placed on the bottom of the split mold and the Sahara sand is placed into the funnel and then raised along the specimen axis of symmetry without any drop in height. After that, the entire sample was pressured vertically

by hand using a rigid steel plug to certain depth to achieve an appropriate medium level of relative density.

4. To create a dense specimen, a collar is placed on the split mold top, and the specimen is formed into 5 layers using the dry funnel deposition method. An 80-N surcharge is applied to the top of each lift, and vibration is applied in evenly timed increments to the top of each lift using a hand-held vibrator. One second of vibration was used for the first layer and vibration was increased by one second for each subsequent layer. After that, the collar is removed and the specimen top is gently leveled off with the top of the split mold by a steel straightedge. Figure 3.6 and 3.7 show the apparatuses used to create a dense specimen.
5. After the Sahara sand specimen is formed into the split mold, a filter paper and porous stone are put on top of the specimen. Then, the top cap is placed over the porous stone. The latex membrane is stretched over the top cap and secured with three O-rings. The drainage lines are attached to the top cap at this point.
6. The vacuum holding the membrane against the split mold is removed and then applied to inside of the specimen to create an initial effective confining stress of about 30 kPa before the split mold is removed.
7. The diameter and height of the specimen are measured five times at several locations by using a pi tape and a caliper, respectively, both with resolution of 0.01 mm to compute the initial volume of the specimen.
8. The acrylic cylindrical cell and three threaded rods are set around the specimen. Then, the all top platen is installed and the tension bolt nuts are tightened. After that, the cell is filled with fresh de-aired water. Then, the piston rod is lowered

until it just touches the top cap. The piston locking screw is tightened to prevent any further movement of the piston rod.

9. The cell pressure is applied while simultaneously decreasing the vacuum within the sample to maintain a constant 30-kPa effective stress level at the beginning of the test. Then, triaxial testing proceeds as outlined in the following sections.

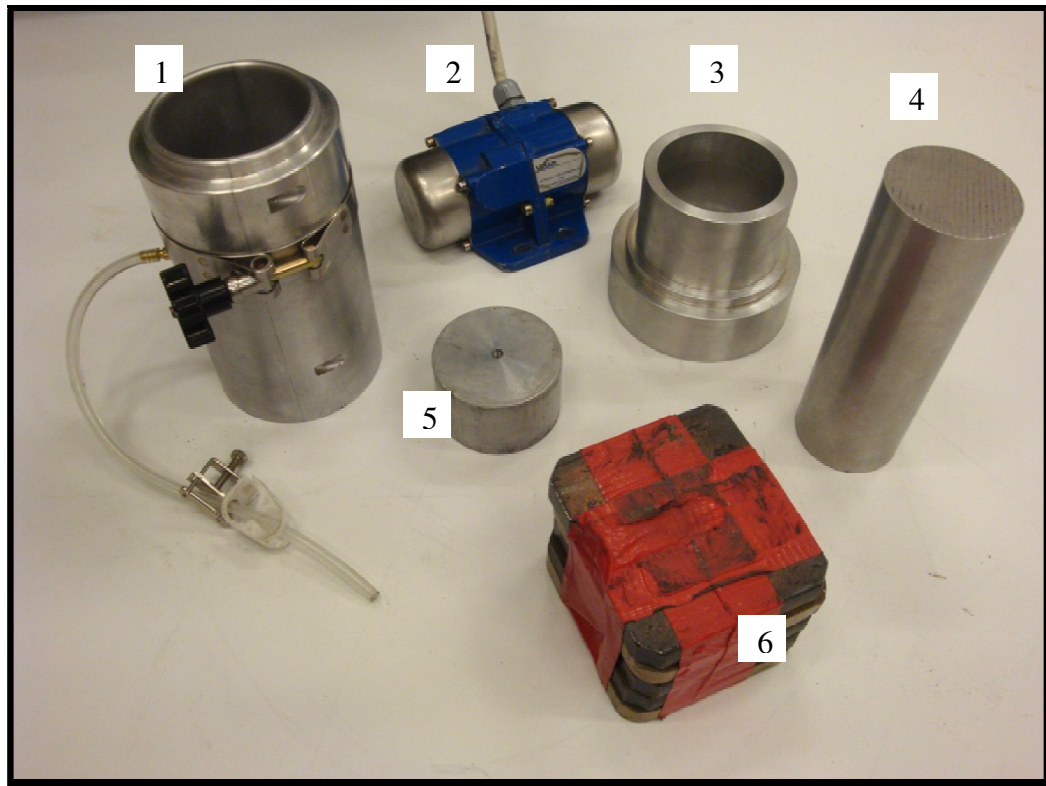


Figure 3.6 (1) Split mold, (2) Hand-held vibrator, (3) Collar, (4) Cylindrical compaction arm, (5) Rigid steel plug, (6) Surcharge



Figure 3.7 Set up of the equipments used to create dense specimen

3.2.2 Specimen Homogeneity

The uniformity of the loose and dense reconstituted specimens tested in this study (both in terms of D_R and FC distributions) was assessed systematically by horizontally slicing the reconstituted specimens. A total of six horizontal slices were spaced evenly along the length of the specimen. The horizontal slices were divided using the collar apparatus, shown in Figure 3.8. All collars were tapered along their edges so that horizontal slices cut with a 0.127-mm-thick steel plates could be created without disturbing the specimens. D_R and FC were measured in five of the collars, representing

the total height of the specimens. The collar apparatus was specifically designed for the purpose of determining the D_R and FC for each slice.

When reconstituting collared specimens, the entire system was placed on a porous stone with filter paper (figure 3.8). In order to reconstitute a specimen, a funnel technique was used. As described earlier, the spout of a funnel was placed on the bottom of the collar apparatus, then the Sahara sand was placed into the funnel and then slowly raised along the specimen axis of symmetry without any drop in height to reconstitute a loose specimen. In order to create a dense specimen, a vibratory technique was used. As mentioned earlier, the samples were split into 4 layers using the dry funnel deposition method, and an 80-N surcharge was applied to the top of each lift and vibration was applied in evenly timed increments to the top using a hand-held vibrator. One second of vibration was used for the first layer and vibration was increased by one second for each subsequent layer.

Before the collared layers were sliced, the porous stone was placed into a water bath, allowing capillary rise to wet the entire specimen. The purpose of the water bath was to allow the specimens to become unsaturated so that they could be handled without the applications of any external confinement or vacuum. Careful handling was employed throughout the procedure to minimize sample disturbance and guarantee that both the D_R and FC would not be altered in the layers during the slicing and removal of each layer.

As discussed earlier, six collar layers were initially used, while D_R and FC were only measured in five collars. The purpose of the sixth uppermost collar was to allow proper settlement of the specimen during capillary rise. After the specimen become

unsaturated, the sixth collar was removed, as it was no longer completely filled with material.

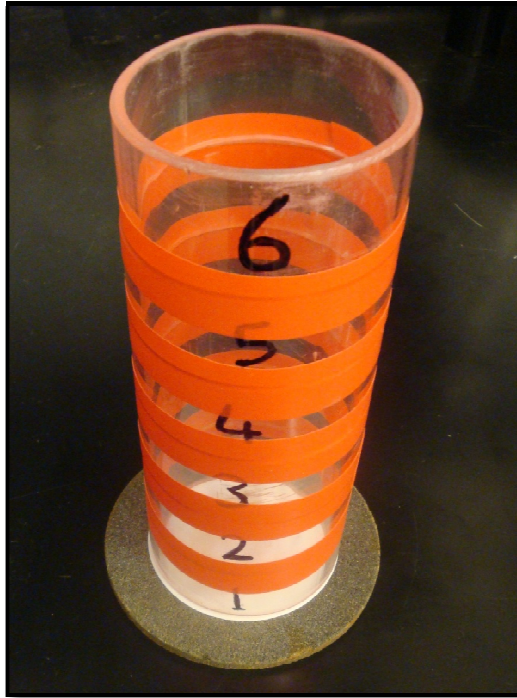


Figure 3.8 collar apparatus for specimen uniformity checks

3.2.3 Triaxial Apparatus

In this research, a triaxial apparatus was employed to study the mechanical behavior of the Libyan Sahara sand. The test apparatus used to perform the triaxial tests included a servo-controlled load frame with digital instrumentation for measuring load, displacement, and pressure. The pressures were applied manually using a pressure panel board, and the volume changes were monitored manually using pipettes. The digital instruments were calibrated to determine the calibration factor, resolution, and accuracy for each instrument. The pressure, load, and displacement transducers were calibrated

with a dead weight apparatus, load ring, and micrometer, respectively. The manufacturer capacity specification, calibration factor, excitation voltage of the ADIO module, accuracy, and real time screen resolution for each instrument are given in Table 3.1.

Table 3.1 Summary of calibration data for instruments

Digital Instrument	Capacity	Calibration Factor	Excitation Voltage of the ADIO module	Accuracy	Resolution
Cell Pressure Transducer	0-1000 kPa	69592.80 kPa/Vs/Ve	10.0140 V	0.12 %	0.07 kPa
Pore Pressure Transducer	0-1000 kPa	69668.23 kPa/Vs/Ve	10.0140 V	0.07 %	0.07 kPa
Force Transducer	0-8896.4 N	2812770.08 N/Vs/Ve	10.0140 V	0.67 %	0.45 N
Displacement Transducer	0-51 mm	51.88 mm/Vs/Ve	10.0140 V	0.09 %	0.0025 mm
Burettes	0-25 mL	NA	NA	NA	0.05 mL

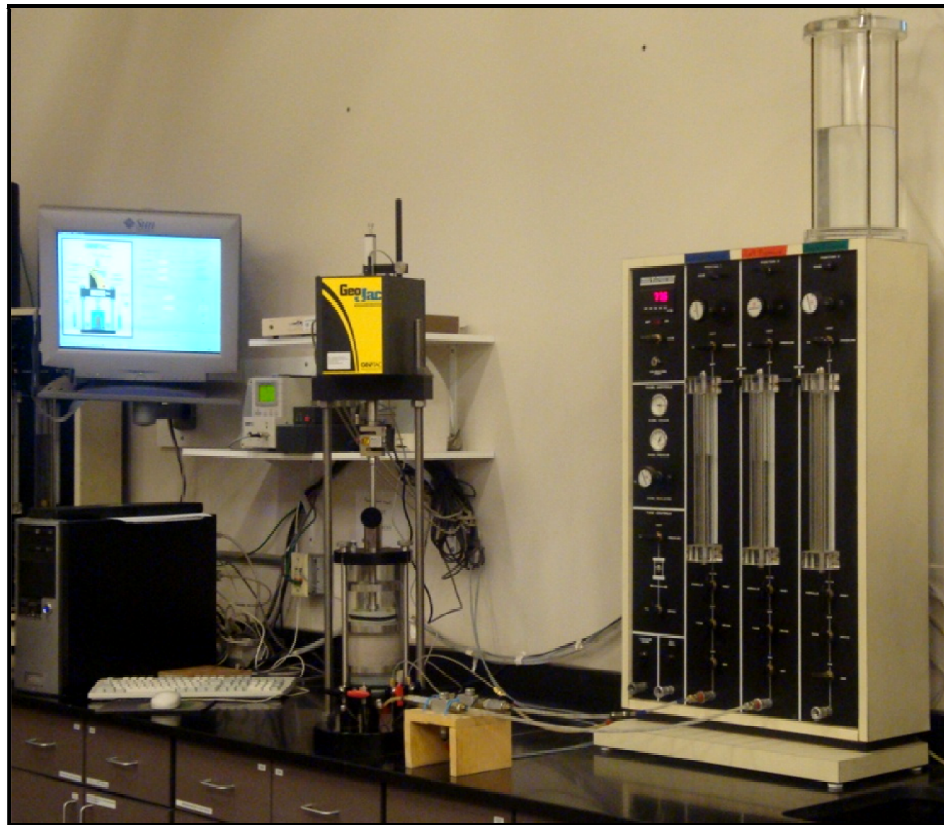


Figure 3.9 Triaxial apparatus used in the study

The procedures used during the triaxial testing program are based on standardized ASTM D 4767 testing procedures for undrained triaxial testing. For drained triaxial testing, well-established techniques originally developed for clean sands were used (Head 1986).

3.2.3.1 Flushing

After the Sahara sand specimens were reconstituted based on the procedure mentioned earlier, the initially-dry specimens were slowly flushed with fresh de-aired water from the bottom to the top of the specimen. For all specimens, a hydraulic gradient less than 1.5 and an effective radial (or confining) stress (σ'_r) equal to 30 kPa was maintained during flushing. In order to eliminate air bubbles from the specimen, a volume of water equal to 20 times the specimen's pore volume was flushed through the specimen during approximately 12 hours.

3.2.3.2 Back Pressure Saturation

After the flushing stage, the back pressure saturation procedure was conducted manually according to Head (1998). Back pressure and cell pressure increments equal to 30 kPa and an initial p' equal to 30 kPa were used at this stage until the pore pressure coefficient B (Skempton 1954) reached a value of 0.99 or higher. Final B values are reported for each triaxial test in Tables 4.2 and 4.3. The axial strain (ϵ_a) was measured for each specimen during both the flushing and back pressure saturation stages using an external LPDT (Linear Potentiometric Displacement Transducer), which was securely connected to the axial actuator and piston rod. The volumetric strain (ϵ_p) was measured

for each specimen during the flushing and back pressure saturation stages using a calibrated burette which was connected to the cell-pressure line.

3.2.3.3 Isotropic Compression

After back pressure saturation, the specimens were subjected to incremental increases in isotropic p' equal to 30, 50, 100, 200, or 400 kPa. Then final isotropic p' levels equal to 100, 200, or 400 kPa were used in the drained and undrained axisymmetric compression tests. The volumetric strains (ϵ_p) were manually recorded during the flushing, back pressure saturation stages using a calibrated burette which was connected to the cell-pressure line. For isotropic compression and shearing (for drained tests) stages, the volumetric strains (ϵ_p) were manually recorded using a calibrated burette which was connected to the back-pressure line. Axial strains (ϵ_a) were also recorded throughout flushing, back pressure saturation, isotropic compression and shearing steps using an external LPDT (Linear Potentiometric Displacement Transducer), which was securely connected to the axial actuator and piston rod.

3.2.4 Drained Triaxial Compression

The main goals in this stage are: (1) determining the intrinsic variables ϕ_c , Q , and R associated with critical state and dilatancy response of Sahara sand; and (2) characterizing the mechanical behavior of this soil under drained condition. Specimens were reconstituted to each loose, medium, and dense initial levels of D_R . Three each group of specimens at a similar D_R level was then consolidated isotropically to levels of

$p' = 100, 200$ and 400 kPa and sheared under drained conditions to levels of axial strains of approximately 27%.

3.2.5 Undrained Triaxial Compression

Consolidated isotropically undrained triaxial tests were conducted to characterize the mechanical response of Sahara sand under undrained condition. Specimens were reconstituted to each loose, medium, and dense initial levels of D_R . Three each group of specimens at a similar DR level was then consolidated isotropically to levels of $p' = 100, 200$ and 400 kPa and sheared under undrained conditions to levels of axial strain of approximately 27%, which corresponds closely to the maximum axial stroke of the triaxial apparatus used in this research.

Both drained and undrained tests were performed under strain-controlled conditions, with an axial strain rate equal to 0.09 %/min to allow full dissipation of excess porewater pressures during drained axisymmetric compression and full equalization of excess pore pressures throughout the specimens during undrained triaxial compression.

3.2.5.1 Area Corrections for Triaxial Results

Triaxial test results were corrected for changes in the cross sectional area according to the framework outlined by La Rochelle et al. (1988). The corrected cross sectional area for tests that show bulging failure, which assumes that the specimen deforms as a right cylinder, is defined by the following equation:

$$A_c = A_o \left(\frac{1 - \varepsilon_p}{1 - \varepsilon_a} \right) \quad \text{Equation 3.1}$$

where A_c = corrected cross sectional area for deformed specimen, A_o = cross sectional area of the specimen after isotropic compression, ε_a = axial strain during axisymmetric compression, and ε_p = volumetric strain during axisymmetric compression.

According to the La Rochelle et al. (1988) framework, for triaxial tests in which the specimen fails along a shear plane, the cross sectional area may be calculated up to peak q using equation 3.1, and after peak q using equation 3.2.

$$A_c = A_p + (A_{ce} - A_p) \left(\frac{\varepsilon_a - \varepsilon_{ap}}{\varepsilon_{ae} - \varepsilon_{ap}} \right) \quad \text{Equation 3.2}$$

where A_c = corrected cross sectional area, A_p = cross sectional area at peak deviator stress, ε_a = axial strain, ε_{ap} = axial strain at peak deviator stress, ε_{ae} = axial strain at the end of the test, and A_{ce} = cross sectional area at the end of the test and is defined by:

$$A_{ce} = \frac{\pi}{4} d_a \cdot d_b \quad \text{Equation 3.3}$$

where d_a and d_b are perpendicular cross sectional specimen axes at the end of the test, which are perpendicular and parallel to the motion of the horizontal projection of the shear plane. All consolidated undrained triaxial specimens tested in this study were observed to have bulging failure, while consolidated drained triaxial specimens were observed to have a combination of bulging and shear plane failures. The primary mechanism of failure for consolidated drained triaxial specimens was bulging with the shear plane appearing just at the end of the test and thus appearing to play only a minor role in the failure mechanism. The late, large-strain shear band does not appear to change the shape of deformed specimens in any significant way, as shown in Appendix B. Therefore a bulging failure correction based on La Rochelle et al. (1988) was applied to all tests.

3.2.5.2 Membrane Corrections for Triaxial Results

Similar to the area correction, triaxial test results were corrected for the effect of membrane restraint according to the framework outlined by La Rochelle et al. (1988). According to La Rochelle et al. (1988), when the membrane is placed around the specimen, it applies a lateral confining pressure which is a function of the elastic modulus and the initial diameters of the membrane and specimen. Following the framework outlined by La Rochelle et al. (1988), the initial confining pressure applied to the specimen by the membrane can be calculated as follows:

$$p_{om} = 2E \left(\frac{d_o - d_{im}}{d_o \cdot d_{im}} \right) \quad \text{Equation 3.4}$$

where: p_{om} = initial confining pressure applied to the specimen by the membrane, E = elastic modulus of the membrane at specific axial strain level, d_o = diameter of specimen at the end of consolidation and d_{im} = initial diameter of the membrane.

The effect of membrane restraint was applied to σ'_a by equation 3.5 as follows:

$$\Delta\sigma'_a = \frac{\pi \cdot d_o \cdot E \cdot \varepsilon_a}{A_c} \quad \text{Equation 3.5}$$

where: $\Delta\sigma'_a$ = decrease in effective axial stress due to membrane reinforcement, d_o = specimen diameter at the end of isotropic compression (m), E = elastic modulus of the membrane at normal strains, ε_a = axial strain (%) and A_c = corrected cross-sectional area of the deformed specimen (m²).

The elastic modulus of the 0.3-mm-thick membrane used in this study was determined according to the procedure outlined by ASTM D 4767, and it equals to 813 kPa.

3.2.6 Bender Element Testing

Bender element tests were performed on the Sahara sand to measure the shear wave velocity V_s at various states in order to estimate the small strain shear modulus (G_{max}). Bender element tests were conducted at the end of each isotropic compression stage over a wide range of mean effective confining stresses, where p' was equal to 30, 50, 100, 200, and 400 kPa. The V_s determinations were performed using a sine input trace with a magnitude of 14-V that corresponds to the system maximum, which gives the clearest waveform, and periods of 0.2 mV. Acquisition of the received wave was obtained using a sampling frequency of 2 MHz and a sampling interval of 10 ms which were selected to provide a received signal with optimal resolution. These tests were performed using 10 stacks. The bender element used was manufactured by GDS Instruments Limited (Hook, Hampshire, United Kingdom).

The shear wave velocity transmitted through the soil was calculated using the tip to tip distance between the bender elements and the measured wave travel time, according to Vigginani and Akinson (1995a). G_{max} values were calculated using the total unit weight of the specimen at the end of each isotropic compression stage, taking into account the volume change during the isotropic compression stages.

3.2.7 Scanning Electron Microscopy

A scanning electron microscope (SEM) was used to examine the surface and geometrical characteristics of Sahara sand particles. Figure 3.8 shows the setup of the SEM device at Colorado State University's Chemistry Department used in this study. The SEM used was the JSM-6500F manufactured by Japan Electron Optics Laboratory

(JEOL Ltd), which is a field emission scanning electron microscope (FESEM) equipped with an In-Lens Thermal Field Emission Electron Gun (TFEG).

The significant magnification abilities of SEM allow grain shape and surface characteristics of the particles to be observed. In order to enhance the signal and increase the resolution, a thin film of gold (about 15-nm) was deposited on the surface (sputter coating).

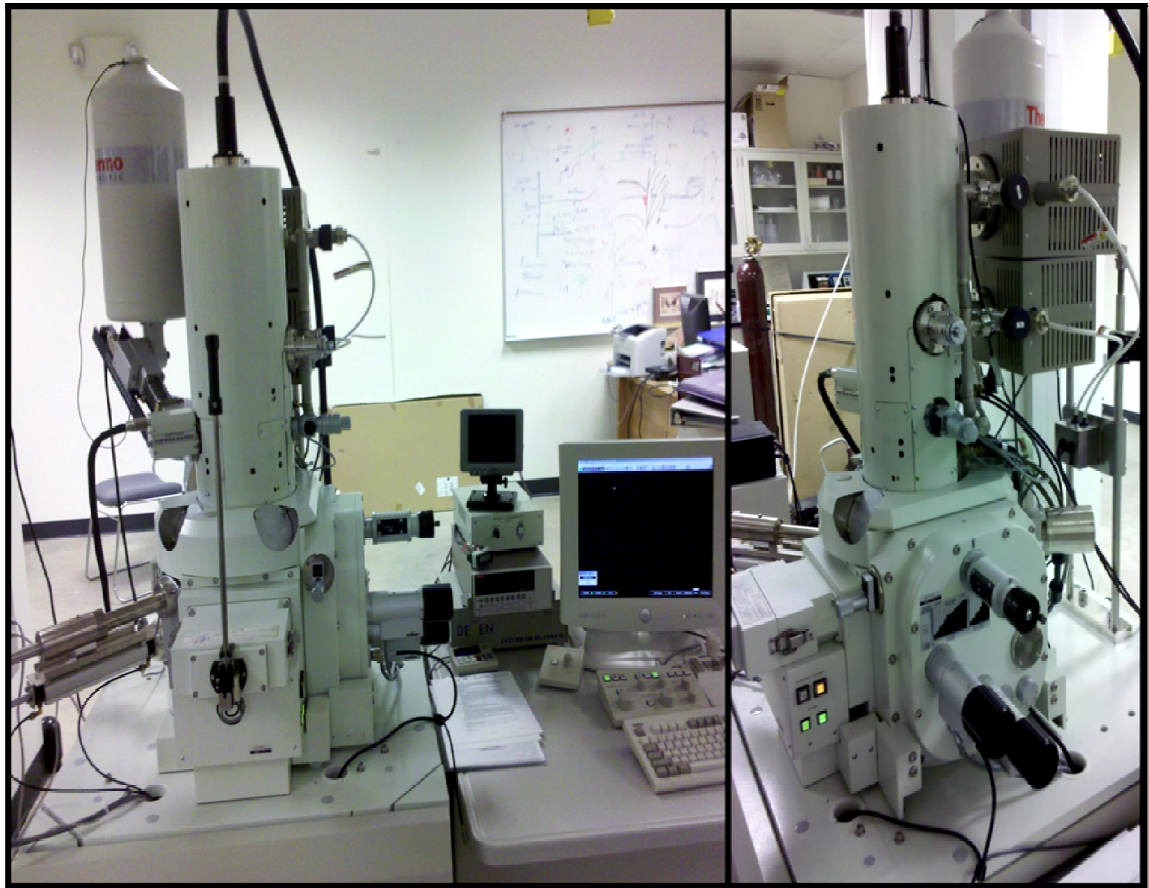


Figure 3.10 Scanning Electron Microscope device used in this study

CHAPTER 4: ANALYSIS OF RESULTS

4.1 Specimen Homogeneity

In the present study, the collars apparatus was employed to evaluate the homogeneity of reconstituted Sahara sand specimens prepared using the specimen preparation method described in Chapter 3. The D_R and FC variations of two loose and two dense Sahara sand specimens reconstituted in several layers are shown in Figure 4.1a and 4.1b, respectively. Table 4.1 shows the mean and the coefficient of variation for both relative density and fines content of each layer for all four specimens tested.

Based on the results shown in Figures 4.1a and 4.1b, the FC and D_R variations across the height of Sahara sand specimens are small. Homogeneity results show the collars apparatus to be very suitable and applicable for the successful reconstitution of uniform and homogeneous Sahara sand specimens in the laboratory.

Table 4.1 Mean and Coefficient of Variation for Loose and Dense Specimens

	Relative Density, D_R (%)		Fines Content, FC (%)	
	Mean	Coefficient of Variation (%)	Mean	Coefficient of Variation (%)
Loose - Specimen 1	18	22	24	2
Loose - Specimen 2	13	20	24	5
Dense - Specimen 1	69	3	25	4
Dense - Specimen 2	69	3	26	5

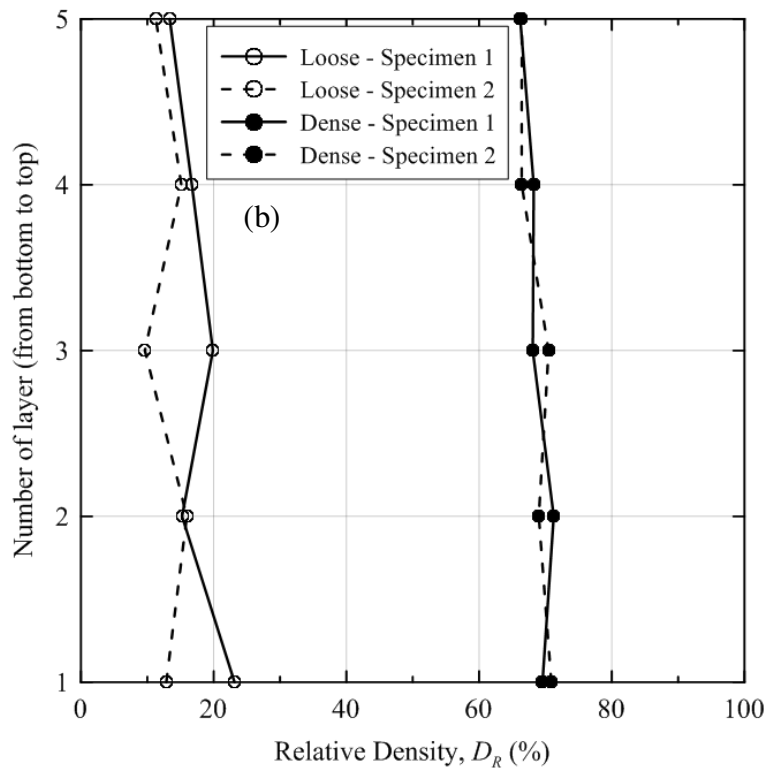
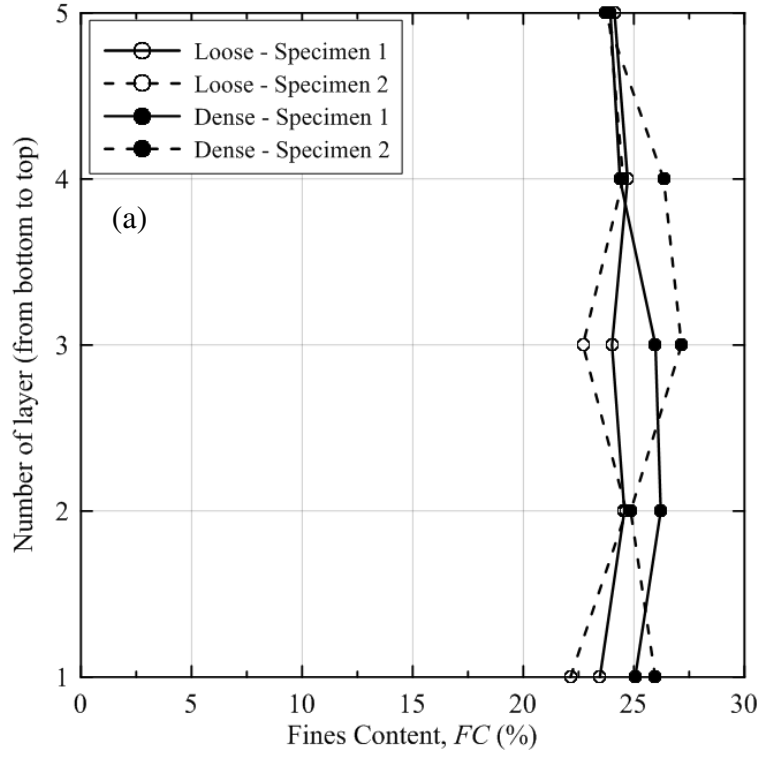


Figure 4.1 Variation of (a) fines content and (b) relative density over the specimen height

4.2 Triaxial Response

4.2.1 Saturation

The minimum BP required to achieve $B \geq 0.99$ varied from about 200 kPa to 500 kPa depending on the initial soil state (loose, medium or dense) and the volume of de-aired water flushed through the specimen prior to BP saturation. The amount of de-aired water flushed through the specimen appeared to have a strong effect on the required BP. Specimens flushed with more than 20 times the specimen's pore volume of de-aired water required the lowest BP and were the easiest to saturate.

4.2.2 Isotropic Compression

After back pressure saturation, specimens were isotropically compressed to a maximum p' equal to 100, 200 or 400 kPa. All tests followed the same isotropic compression steps with the most comprehensive sequence defined by $p' = 30, 50, 100, 200$ and 400 kPa, for specimens isotropically compressed to 400 kPa. Results of isotropic compression are illustrated for Sahara sand specimens in specific volume v versus the natural logarithm of p' space for specimens tested in drained and undrained conditions in Figures 4.2 and 4.3, respectively. As mentioned in Chapter 3, specimen volume changes during flushing and back pressure saturation were measured using a calibrated burette, which was connected to the cell pressure line. A summary of initial, intermediate and final states for all specimens tested are provided in Table 4.2.

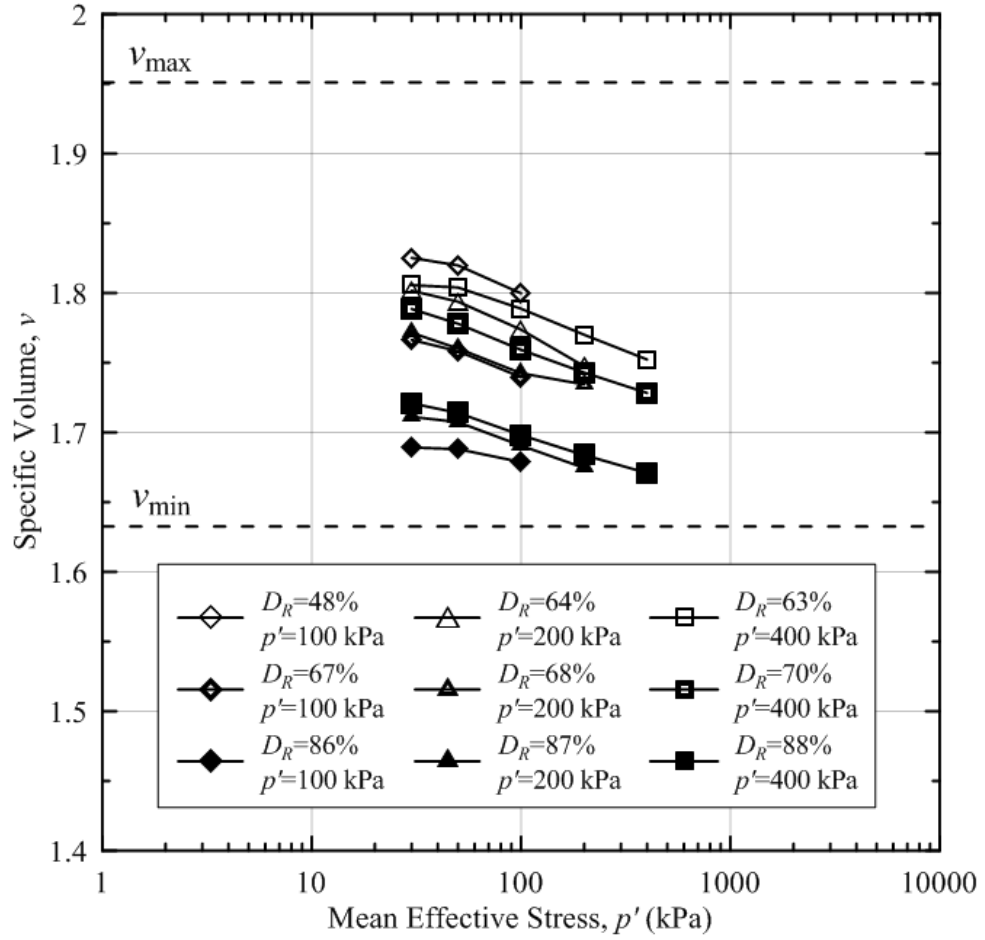


Figure 4.2 Isotropic compression data for Sahara sand specimens. Values of p' and D_R represent the final specimen state at the end of isotropic compression, before drained shearing

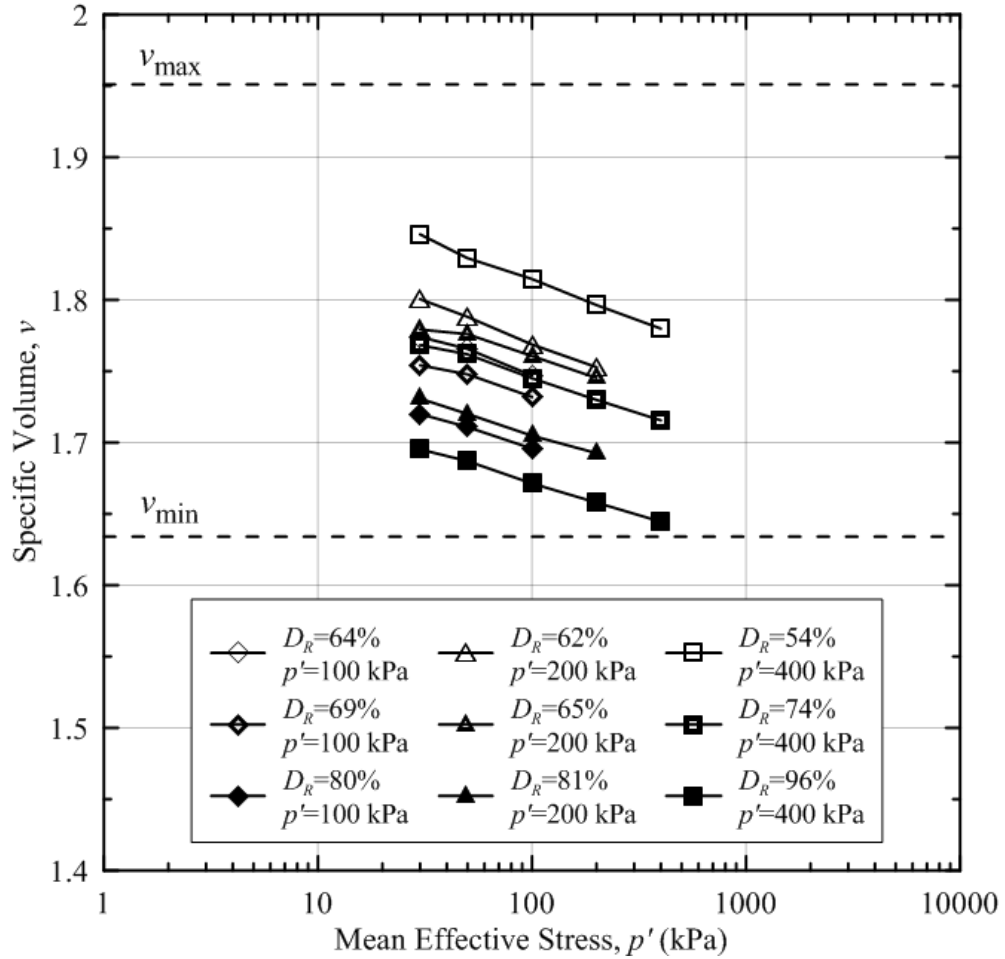


Figure 4.3 Isotropic compression data for Sahara sand specimens. Values of p' and D_R represent the final specimen state at the end of isotropic compression, before undrained shearing

As shown in Figures 4.2 and 4.3, specific volume decreases in log-linear fashion with increases in mean effective stress. Also, the isotropic compression relationships for samples of varying initial specific volume exhibit the same change in specific volume for identical increases in mean effective stress. In other words, isotropic compression lines are parallel. The parallel relationship is only dependent on the initial specific volume and

is expected for granular media. Based on Figures 4.2 and 4.3 the average slope of the isotropic compression trends, k , is 0.0002.

As shown by Atkinson and Bransby (1978), sands reach their respective normal consolidation lines at high values of mean effective stress and behave as though they are normally consolidated. For example, initially loose Chattahoochee River sand sample reached the normal consolidation line at a mean effective stress of approximately 3 MPa, while an initially dense sample of identical sand reached the same normal consolidation line at a mean effective stress of larger than 40 MPa.

4.2.3 Drained Monotonic Loading

Isotropically consolidated drained triaxial tests were conducted over a wide range of combinations of p' and D_R in order to characterize a wide range of mechanical behavior. Specimens were subjected to drained axisymmetric compression to an axial strain ϵ_a of approximately 27%. The strain rate used for all tests was equal to about 0.09%/minute, with the actual value depending upon the final consolidated height of the specimen, which was similar but not constant for all specimens. This strain rate was conservatively determined from the procedure outlined in Head (1998).

Figure 4.4 illustrates the variation of the deviatoric stress q versus axial strain ϵ_a for consolidated isotropically drained triaxial tests of Sahara sand specimens. Critical state was defined for all tests as the final data point at maximum axial strain, which fits to the best estimates that could be made of the critical state conditions of the specimens for each test as they approach a state of constant stress (in terms of p' and q) and specific

volume v with continued axial deformation. Figure 4.5 shows plots of volumetric strain ϵ_p versus ϵ_a for the Sahara sand specimens.

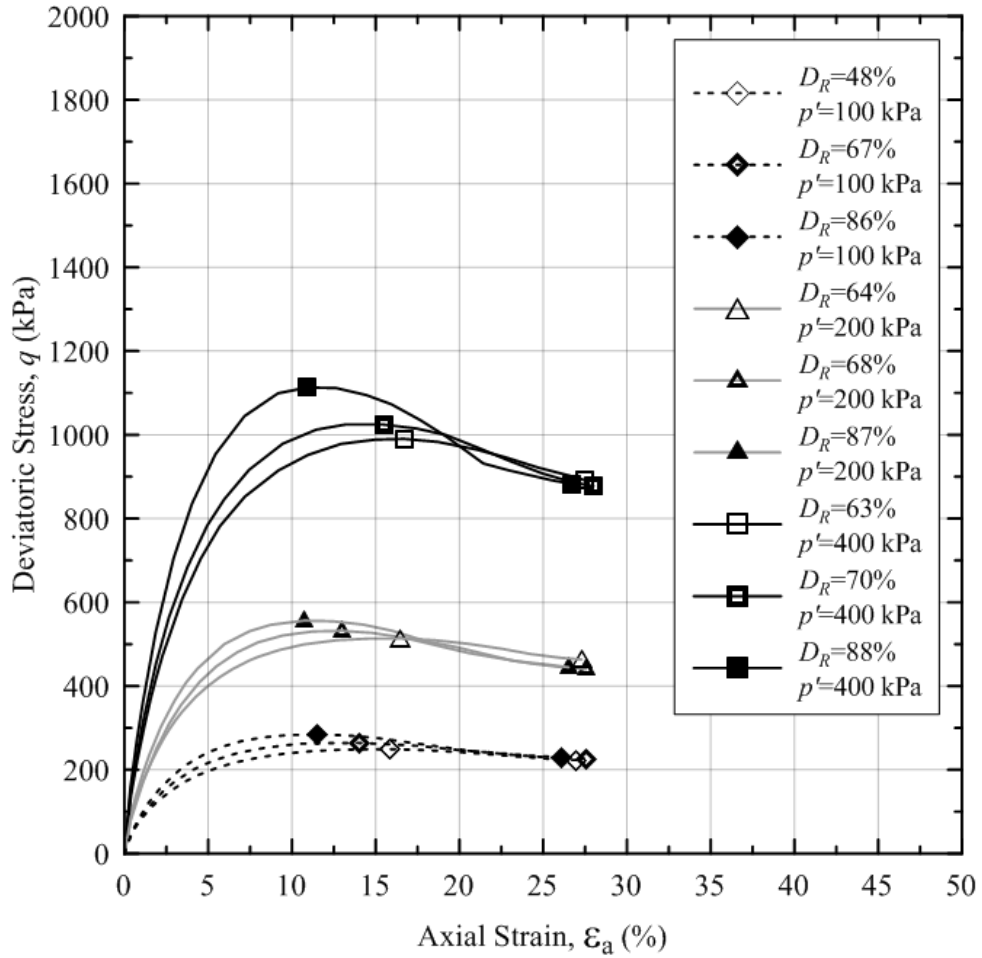


Figure 4.4 Deviatoric stress versus axial strain for isotropically consolidated drained triaxial tests. Values of p' and D_R represent the final specimen state at the end of isotropic compression, before shearing

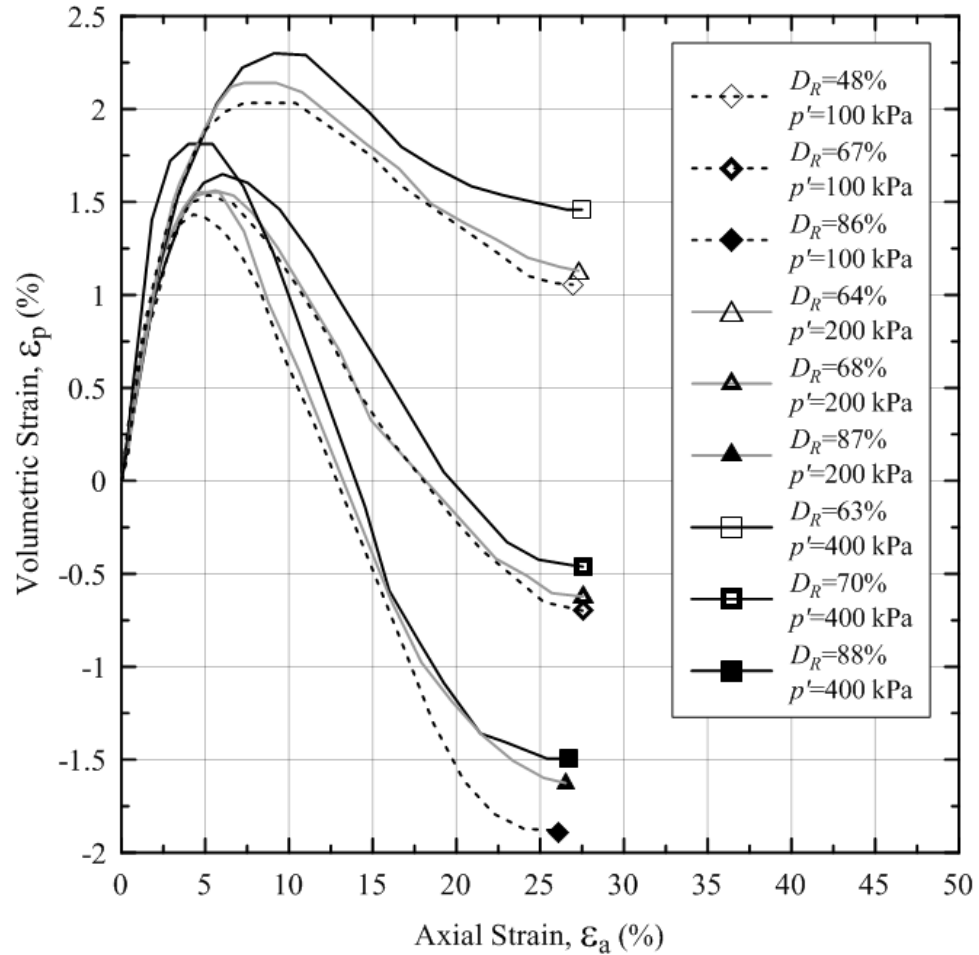


Figure 4.5 Volumetric strain versus axial strain. Values of p' and D_R represent the final specimen state at the end of isotropic compression, before shearing

Based on Figure 4.4 several conclusions can be drawn. Firstly, for a specific level of mean effective stress, loose samples tend to show a more gradual strain hardening behavior in comparison to denser samples. Denser samples have a more compact configuration, allowing a greater deviatoric stress to be mobilized at lower levels of strain. Secondly, peak friction angles are greater and are reached at lower strain levels for denser specimens at all levels of mean effective stress than for looser specimens.

Thirdly, strength and stiffness increase for increasing mean effective stresses and increasing relative density values. Finally, large strain values at critical state show basically identical values of critical state friction angles for similar levels of mean effective stress, which is consistent with the critical state framework, as discussed earlier.

Figure 4.5 in combination with Figure 4.4 allows for a complete analysis of the effects of both mean effective stress and relative density levels on specimens isotropically consolidated and sheared in drained triaxial tests. According to Figure 4.5 dense specimens contract initially and then dilate more than loose specimens. Conversely, looser specimens contract more during the shearing process, for identical levels of mean effective stress. During drained shearing, loose samples are able to contract more due to larger initial void spaces between particles which are eventually filled by adjacent particles at increasing strain levels. Also, specimens of similar relative density subjected to lower levels of mean effective stress dilate more than specimens subjected to high levels of mean effective stress during the shearing process. This is because denser samples require work in order to dilate against the applied effective confining pressure. At high strain levels specimens reach a relatively constant volumetric strain due to the critical state being obtained.

Drained axisymmetric compression results are illustrated in Figure 4.6 in $\ln(p')$ versus v space for Sahara sand specimens.

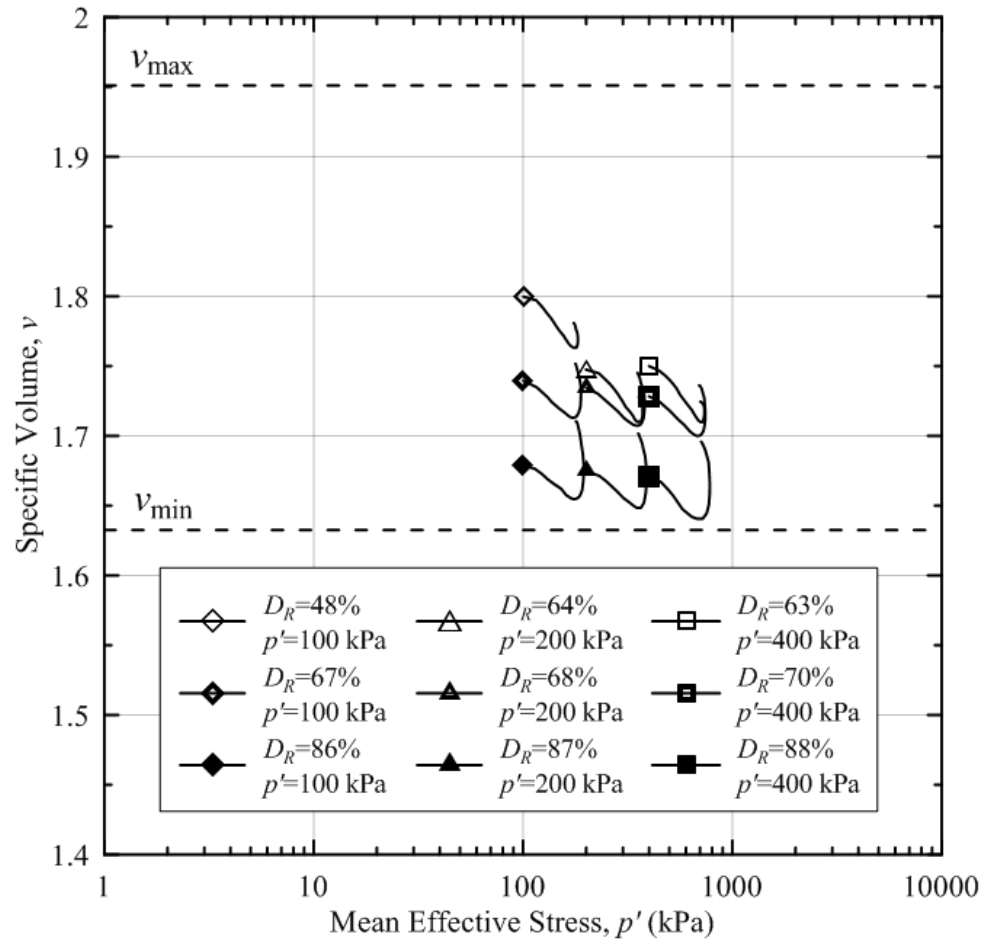


Figure 4.6 Sahara sand specimens in $\ln(p')$ – v space during drained axisymmetric compression

Drained effective stress paths are presented in terms of the stress invariants p' and q for Sahara sand in Figure 4.7.

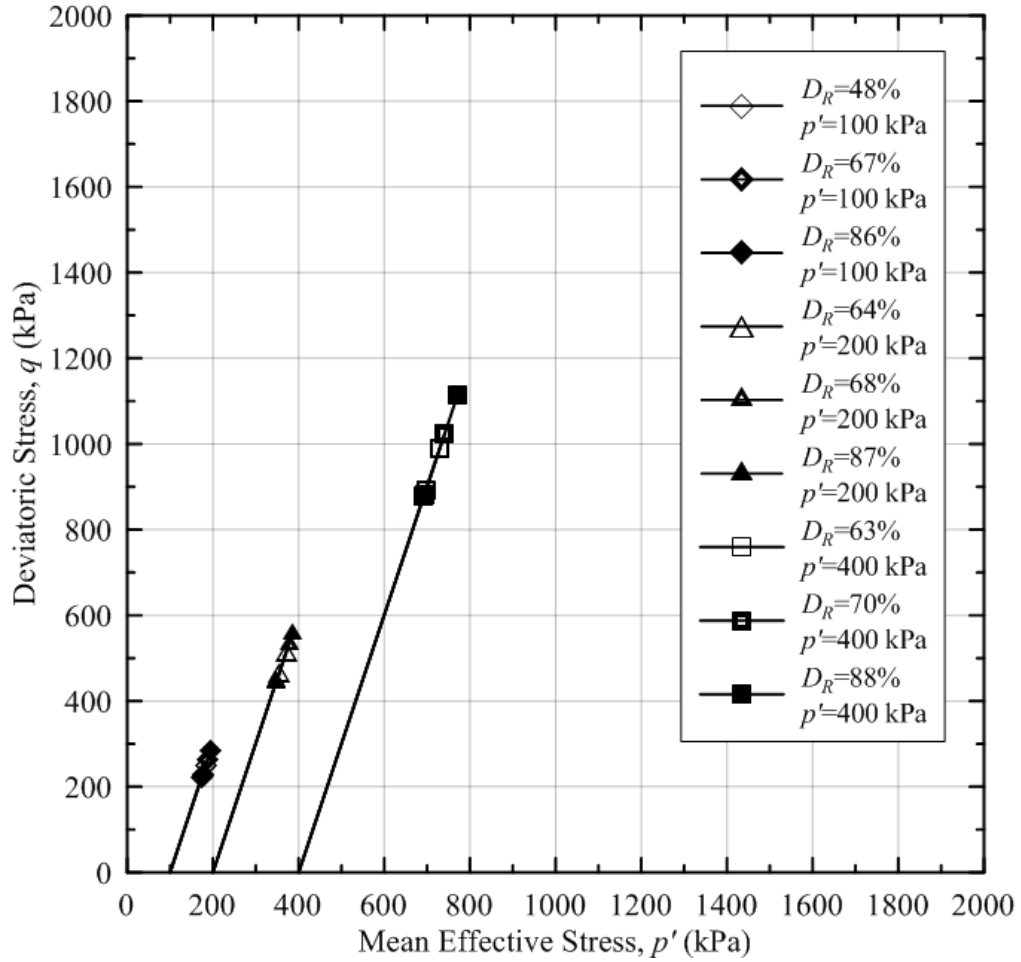


Figure 4.7 Drained effective stress paths. Values of p' and DR represent the final specimen state at the end of isotropic compression, before shearing. The two data points for each test correspond to peak and critical state stress states

Table 4.2 presents the peak and critical state friction angles (ϕ_p and ϕ_c) mobilized in each isotropically consolidated drained triaxial test alongside their corresponding state (in terms of p' and D_R) after specimen setup, after flushing and back pressure saturation, and at the end of isotropic compression (start of axisymmetric compression). All critical state values for p' , q and v were defined in Table 4.2 at the point of maximum shear strain mobilized in the tests and are referred to as p'_{cs} , q_{cs} and v_{cs} . In Table 4.2, $D_{R, Initial}$ = as reconstituted initial D_R , $D_{R, Flush \& BP} = D_R$ after flushing and backpressure saturation, $D_{R, AC} = D_R$ after isotropic compression.

Table 4.2 Results for the drained triaxial tests completed on Sahara sand

Test	p' (kPa)	$D_{R, Initial}$ (%)	$D_{R, Flush \& BP}$ (%)	$D_{R, AC}$ (%)	ϕ_p (deg)	ϕ_c (deg)	v_{cs}	p'_{cs} (kPa)	q_{cs} (kPa)	B
D48-100	100	20	40	48	33.7	31.8	1.78	174	223	0.99
D67-100	100	44	58	67	34.7	32.1	1.75	176	227	0.99
D86-100	100	63	82	86	35.9	32.3	1.71	177	230	0.99
D64-200	200	22	47	64	34.2	32.5	1.73	354	463	0.99
D68-200	200	44	56	68	34.8	31.6	1.75	347	440	0.99
D87-200	200	62	75	87	35.6	31.8	1.70	349	445	0.99
D63-400	400	20	46	63	33.6	31.8	1.73	696	892	0.99
D70-400	400	40	51	70	34.2	31.5	1.74	692	877	0.99
D88-400	400	62	72	88	35.6	31.6	1.70	694	883	0.99
Average						31.9				

Peak and critical state friction angle values range from 33.6° to 35.9° and 31.5° to 32.5°, respectively. The average value for critical state friction angles is 31.9°. Carraro et al. (2004) performed isotropically consolidated drained triaxial compression tests on Ottawa sand with varying nonplastic silt contents. Results displayed an average critical state friction angle of 32.9° for Ottawa sand mixed with 15% non-plastic silt.

4.2.4 Undrained Monotonic Loading

Isotropically consolidated undrained triaxial tests were conducted over a wide range of combinations of p' and D_R in order to characterize a wide range of mechanical response for undrained conditions. Specimens were subjected to undrained axisymmetric compression to an axial strain ϵ_a of approximately 27%. The strain rate was the same as that of the drained triaxial tests. Figure 4.8 shows the variation of the deviatoric stress q versus axial strain ϵ_a for isotropically consolidated undrained triaxial tests of Sahara sand specimens.

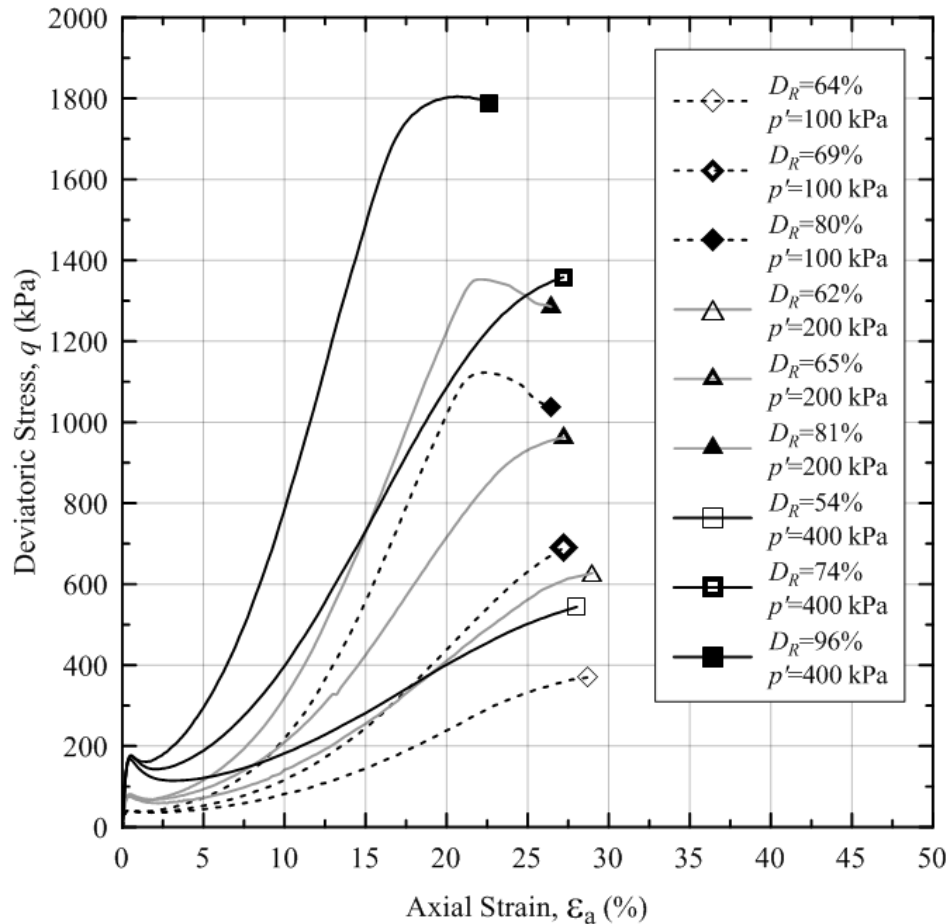


Figure 4.8 Deviatoric stress versus axial strain for consolidated isotropically undrained triaxial tests. Values of p' and D_R represent the final specimen state at the end of isotropic compression, before shearing

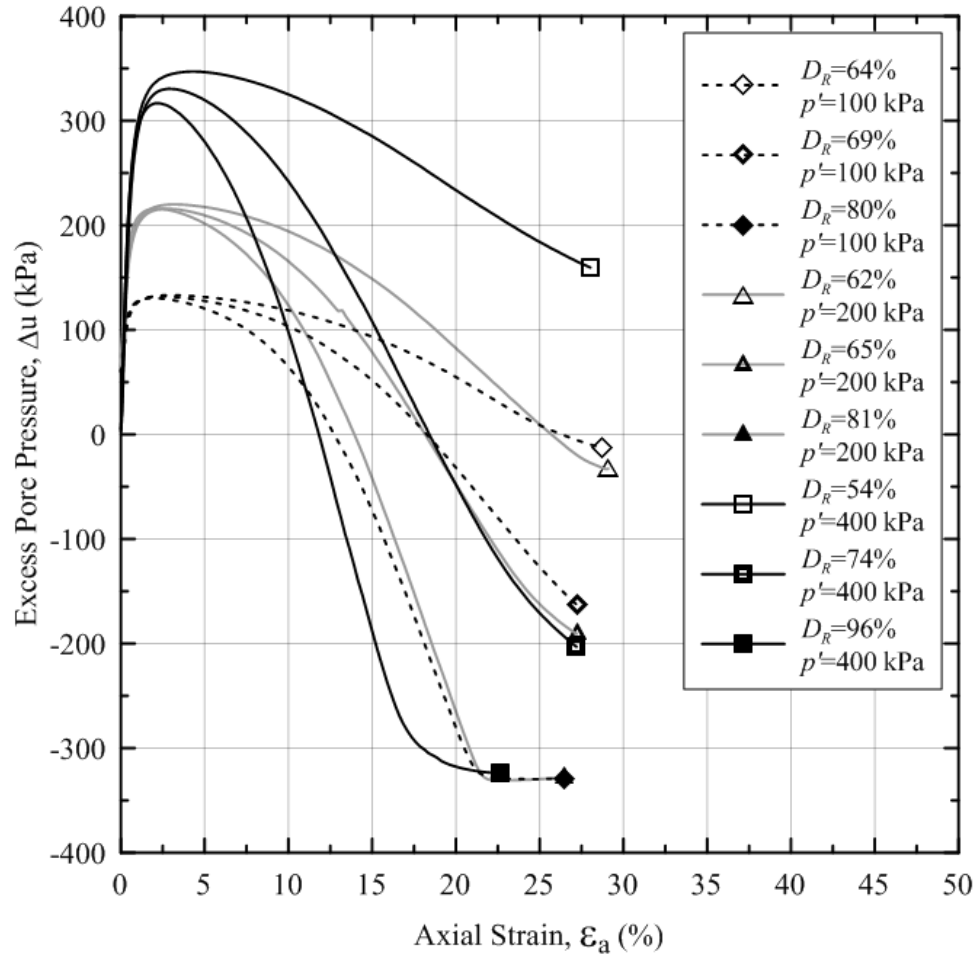


Figure 4.9 Axial strain versus excess pore pressure for consolidated isotropically undrained triaxial tests. Values of p' and D_R represent the final specimen state at the end of isotropic compression, before shearing

Figures 4.8 and 4.9 display the deviatoric stress and excess pore water pressure responses with axial strain for isotropically consolidated specimens sheared in undrained triaxial tests. As shown in Figure 4.8, the undrained, ultimate shear strength increases with both increasing levels of initial mean effective stress and relative density. Excess pore water pressure is developed during undrained shearing because the soil tends toward volume change, but the specimen is unable to alter its volume due to the undrained condition. In undrained shearing, the specimen is confined to a specific volume.

Therefore, the load is partially taken by the pore water leading to pore water pressure changes and altering the mean effective stress carried by the soil particles. In accordance with Figure 4.9, specimens with higher relative densities develop the largest negative excess pore water pressure for all levels of mean effective stress because they would tend to try to dilate the most.

The undrained effective stress paths are presented in terms of the stress invariants p' and q for Sahara sand in Figure 4.10. Most specimens present undrained instability (Murthy et al. 2007) before reaching phase transformation. After phase transformation, all specimens tend toward dilatancy, but they cannot change volume, thus decreasing the excess pore water pressures. The effective stress paths are very similar for all specimens prior to phase transformation, with very similar trends observed up to that point.

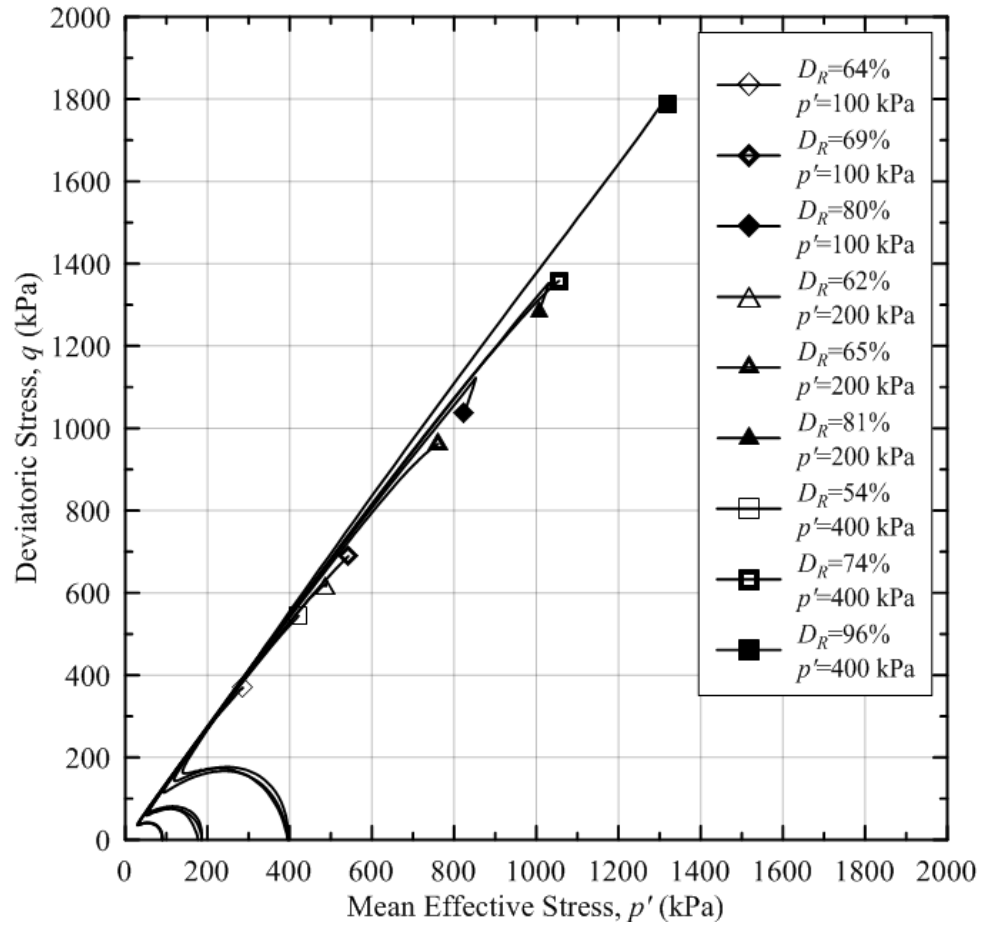


Figure 4.10 Undrained effective stress paths. Values of p' and D_R represent the final specimen state at the end of isotropic compression, before shearing. The data point for each test corresponds to critical state stress states

The results are illustrated in $\ln(p')$ versus v space during undrained shearing for Sahara sand specimens in Figure 4.11. Figure 4.11 displays the entire range of mean effective stress levels subjected to each specimen during the undrained shearing process. Specific volume levels remain constant during undrained shearing due to the testing conditions and the inability of the specimen to change in volume.

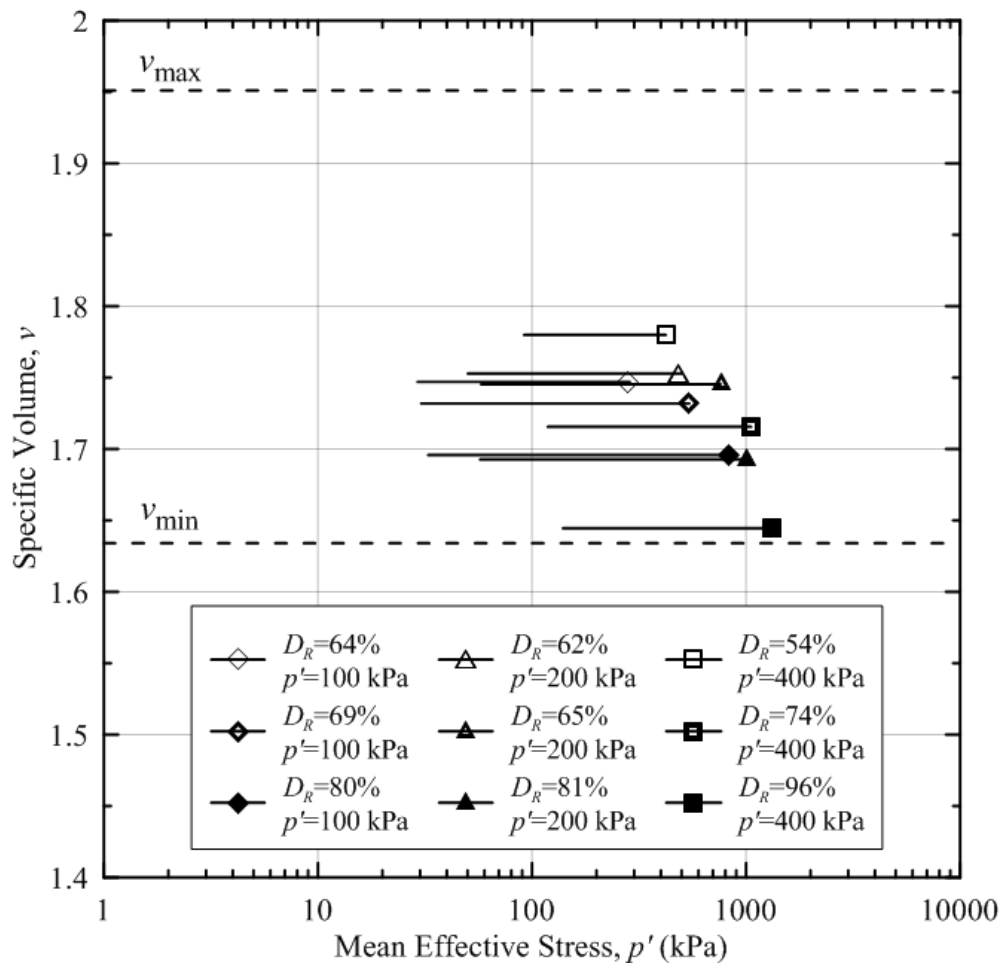


Figure 4.11 Sahara sand specimens in $\ln(p') - v$ space during undrained axisymmetric compression

Table 4.3 presents the critical state friction angles (ϕ_c) mobilized in each individual isotropically consolidated undrained triaxial test alongside their corresponding state (in terms of p' and D_R) after specimen setup, after flushing and back pressure saturation, and at the start of axisymmetric compression.

Table 4.3 Results for the undrained triaxial tests completed on Sahara sand

Test	p' (kPa)	$D_{R, Initial}$ (%)	$D_{R, Flush}$ & BP (%)	$D_{R, AC}$ (%)	ϕ_c (deg)	v_{cs}	p'_{cs} (kPa)	q_{cs} (kPa)	B
U64-100	100	34	56	64	32.1	1.75	286	370	0.99
U69-100	100	48	62	69	31.6	1.73	543	689	0.99
U80-100	100	63	73	80	31.3	1.70	825	1038	0.99
U62-200	200	27	47	62	31.4	1.75	488	616	0.99
U65-200	200	39	54	65	31.5	1.75	761	962	0.99
U81-200	200	57	69	81	31.8	1.69	1006	1285	0.99
U54-400	400	13	33	54	32.1	1.78	421	544	0.99
U74-400	400	41	58	74	32.0	1.72	1055	1358	0.99
U96-400	400	71	81	96	33.6	1.64	1320	1789	0.99
					Average	31.9			

Critical state friction angle values range from 31.3° to 33.6°, with an average value of 31.9°. The critical state from undrained tests is in agreement with that found from drained tests. For comparison, Murthy et al. (2007) performed isotropically consolidated undrained triaxial compression tests on Ottawa sand with 0%, 5%, 10% and 15% of nonplastic silt contents. Results displayed an average critical state friction angle of 30.2°, 30.6°, 31.8° and 34.4° for Ottawa sand mixed with 0%, 5%, 10% and 15% of nonplastic silt, respectively. Also, he found that the critical-state friction angle increases slightly with the addition of a small percentage of silt to the sand. Tests with higher fines contents were not conducted.

4.2.5 Critical State Friction Angle

Critical state values for p' , q and v are all defined for each specific test at the point of maximum axial strain (ϵ_a) and shown in Tables 4.2 and 4.3. The location of the critical state line (CSL) may be estimated from the data points corresponding to the critical states of Sahara sand specimens in $\ln(p')$ - v space (Figure 4.12) and in p' - q space (Figure 4.13). The CSL in p' - q space has a coefficient of determination (R^2) greater than 0.999. On the other hand, the R^2 for the CSL in $\ln(p')$ - v space are much lower at 0.35. The CSL in $\ln(p')$ - v space allows estimation of critical state soil parameters Γ_{cs} and λ_{cs} as the slope and v intercept at $p'=1$ kPa of the CSL (Muir-Wood 1990). The critical state soil parameter M was estimated as 1.28 from the plot of the CSL in p' - q space for all tests. The value of M is also related to the value of ϕ_c for all tests. Results are illustrated in Figure 4.13, where the critical states for all tests are plotted on p' - q diagram. This approach leads to a value of ϕ_c for the Libyan Sahara sand equal to 31.9° . M , Γ_{cs} and λ_{cs} are equal to 1.28, 1.92 and 0.031, respectively.

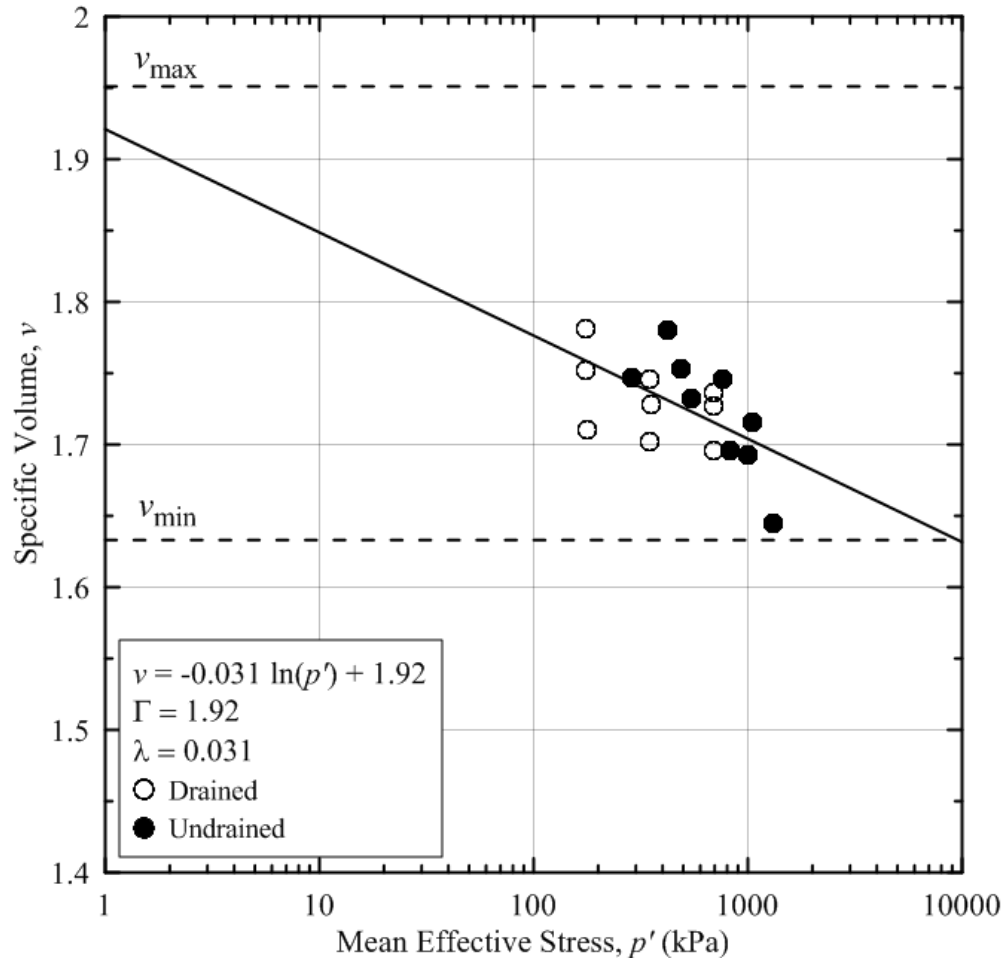


Figure 4.12 *CSL* in $\ln(p') - v$ space for Sahara sand specimens used to determine the critical state parameters Γ_{cs} and λ_{cs}

Figure 4.12 displays specific volume values at respective mean effective stress levels at the end of the shearing stage. The correlation between mean effective stress and specific volume is low ($R^2=0.35$) due to varying initial relative density values during specimen reconstitution.

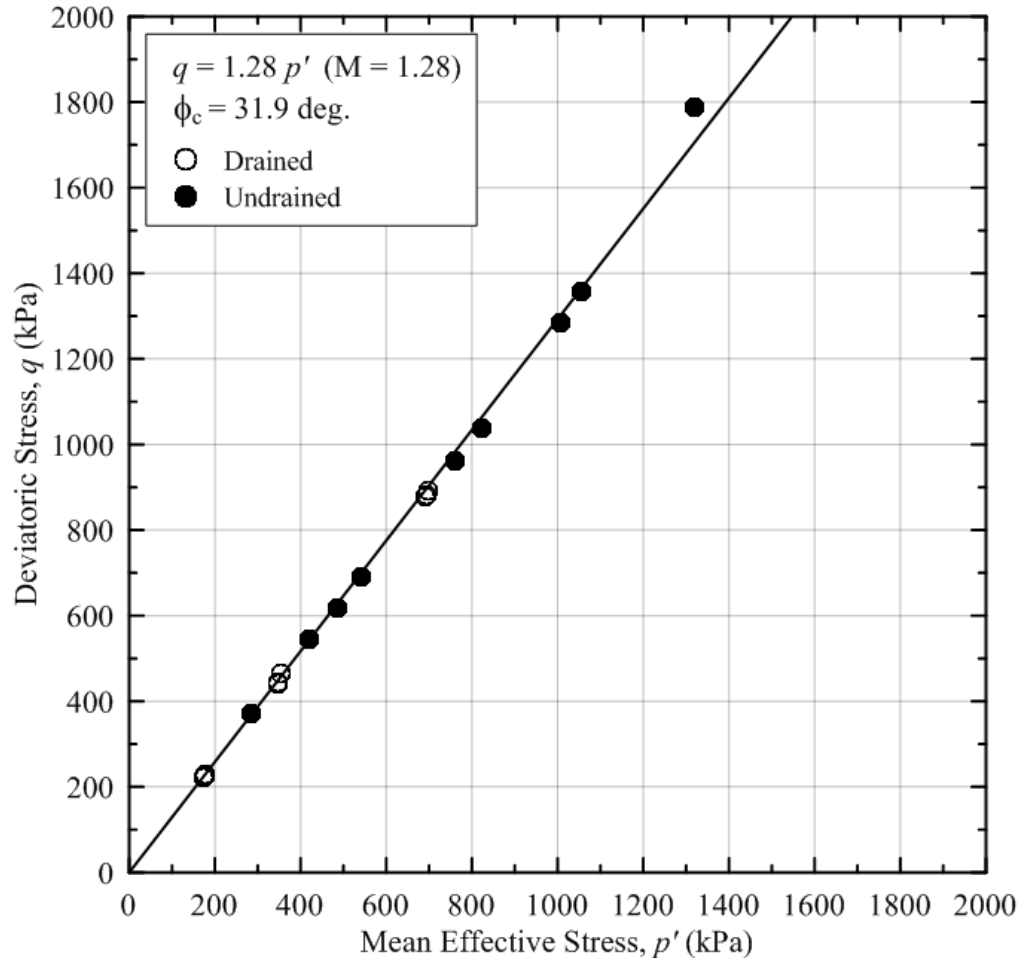


Figure 4.13 CSL in p' - q space for Sahara sand with a linear best-fit value of M and the corresponding value of ϕ_c

Shown in Figure 4.13 are the various deviatoric stress and mean effective stress values for each specimen at the end of shearing. Drained and undrained critical state values are in agreement, and the correlation between all samples is high ($R^2=0.999$). Based on all drained and undrained testing conditions, the value of the critical state friction angle is 31.9° for Libyan Sahara Sand.

4.2.6 Stress-Dilatancy Relationship

Stress-dilatancy relations aim to describe the relationship between the friction and dilatancy angles. Bolton (1986) assessed the stress-dilatancy relationship for various types of clean sands and developed Equation 4.1, which relates ϕ_p mobilized under axisymmetric loading to the state variables D_R and p'_p and the intrinsic parameters of the soil ϕ_c , Q , and R through the relative dilatancy index I_R .

$$I_R = \frac{\phi_p - \phi_c}{3} = I_D \left[Q - \ln \left(\frac{100 \cdot p'_p}{p_A} \right) \right] - R \quad \text{Equation 4.1}$$

where $I_D = D_R(\%)/100$ = relative density after isotropic compression, p'_p = mean normal effective stress at peak strength, p_A = reference stress (=100 kPa) in the same units as p'_p , and Q and R are intrinsic material parameters. This relationship is presented in Figure 4.14 in a slightly modified format as presented by Salgado et al. (2000), where Q and R might be determined from the slope and intercept of the best fit lines going through the data plotted in $I_R + I_D \ln(100 p'_p/p_A)$ versus I_D space. This indicates that the value of Q of Libyan Sahara sand is equal to 8.5 and R is equal to 0.98. For comparison, Bolton (1986) suggested a value of Q equal to 5.5 for chalk, 7 for anthracite, 8 for limestone, and 10 for quartz, and Carraro (2004) found that $R = 1.54$ and $Q = 11.8$ for Ottawa sand with 15% of silt contents. Similar results have been obtained by Salgado et al. (2000) using isotropically consolidated drained triaxial compression tests on Ottawa sand with varying non-plastic silt contents. The experimental data of Salgado et al. (2000) reveals that Q for samples with nonfloating fabric increases with addition of 5% silt and then drops as the silt content is increased further and never returns to the value for clean sand.

Equation 4.1 was used to predict ϕ_p for Sahara sand. Table 4.5 illustrates ϕ_p measured in each test compared to the ϕ_p predicted using equation 4.1. The term $\Delta\phi_p$ shown in Table 4.5 represents the difference between the measured and predicted values of ϕ_p for each test. Results show a maximum absolute difference in the predicted values of ϕ_p less than 1.7 degrees.

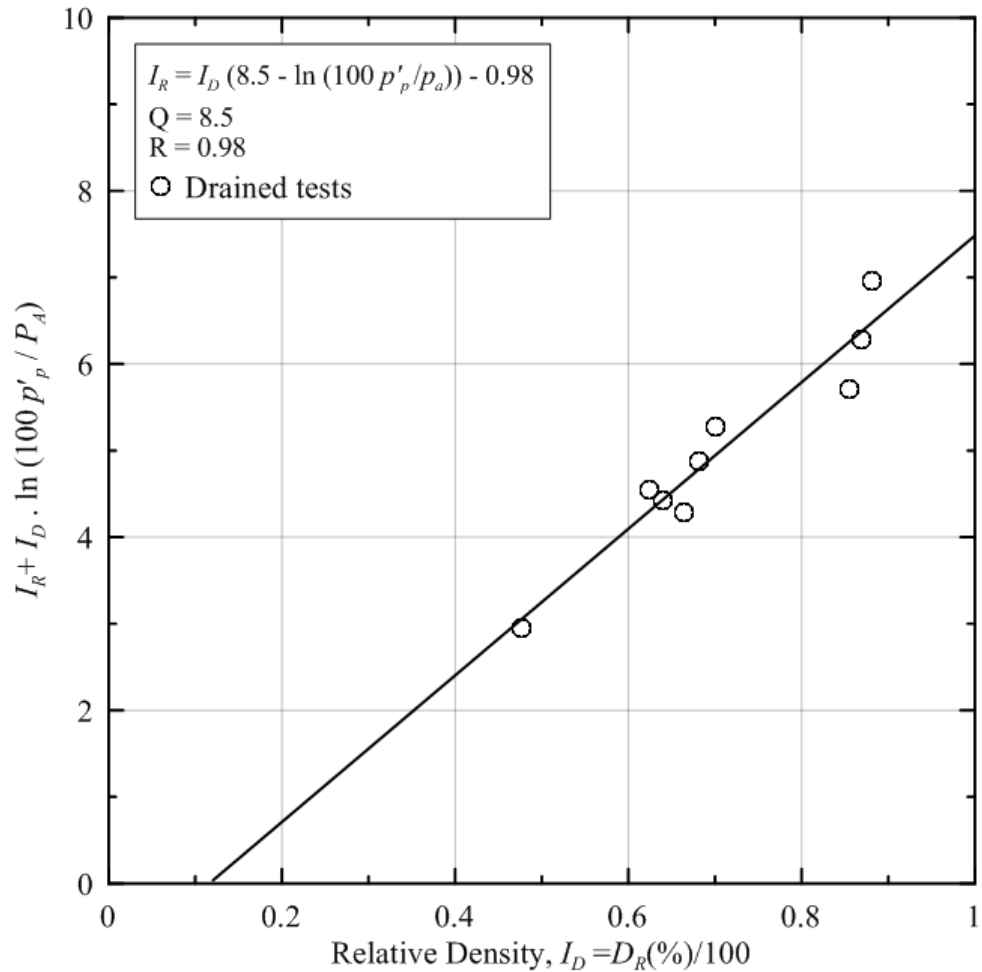


Figure 4.14 Visual illustration of best-fit Q and R values for drained triaxial tests on Libyan Sahara sand

Table 4.5 Comparison of values of ϕ_p predicted using Equation 4.1 with values of ϕ_p measured in individual tests for Sahara sand

		ϕ_c	Q	R		
		31.9°	8.50	0.98		
Test	p_p' (kPa)	I_D	ϕ_p (predicted)	ϕ_p (measured)	$\Delta\phi_p$	
D48-100	183	0.48	33.6	33.7	-0.1	
D67-100	192	0.67	35.4	34.7	0.7	
D86-100	201	0.86	37.1	35.9	1.2	
D64-200	368	0.64	33.9	34.2	-0.3	
D68-200	371	0.68	34.2	34.8	-0.6	
D87-200	385	0.87	35.5	35.6	-0.1	
D63-400	710	0.63	32.5	33.6	-1.1	
D70-400	718	0.70	32.9	34.2	-1.3	
D88-400	737	0.88	33.9	35.6	-1.7	

4.2.7 Comparative Analysis of Specimens of Sahara sand with and without Fines

While a systematic analysis of the effect of FC on soil behavior was out of scope, a basic comparative analysis was performed to determine variation of the strength characteristics of Libyan Sahara sand by removing the fine particles from the host sand. Fine particles were removed according to ASTM D1140. Reconstitution techniques were identical for specimens with and without fines. Both specimens were tested under drained isotropically consolidated conditions in the same triaxial apparatus, at the same level of mean effective stress equal 400 kPa, and similar levels of relative density. The relative density of the specimen with fines was 88%, and the relative density of the specimen without fines was 82% (maximum and minimum void ratios of the clean sand were determined according to ASTM D 4254 and ASTM D 4253, respectively, and are equal to 0.945 and 0.624, respectively).

As shown in Figure 4.15, the critical state is virtually identical for both specimens. The peak friction angle for the specimen with fines was slightly larger than the peak friction angle of the specimen without fines. Table 4.6 displays the values for the peak and critical state friction angles. As shown in Figure 4.16, the specimen without fines tended to dilate a bit more with increasing axial strain than the specimen with fines upon shearing. A similar relationship in dilative behavior for specimens of varying fines content was shown by Carraro et al. (2004).

Table 4.6 Results for the drained triaxial tests completed on Sahara sand

Test	p' (kPa)	FC	$D_{R, Initial}$	$D_{R, Flush \& BP}$	$D_{R, AC}$	ϕ_c	ϕ_p	p'_{cs} (kPa)	q_{cs} (kPa)
D85-400	400	0%	59%	72%	85%	31.4°	35.4°	691	872
D88-400	400	25%	62%	72%	88%	31.6°	35.6°	694	883

As discussed by Salgado et al. (2000) the addition of nonplastic silt from 0 to 20% increase both ϕ_c and ϕ_p . Salgado et al. (2000) also concluded that for fines contents above 20% an inverse relationship is displayed with decreasing ϕ_c as the floating fabric begins to dominate the behavior. Also, ϕ_p decreases for fines content above 20% because of a decrease in ϕ_c and decrease in dilatancy. Due to the relatively large percentage of fines included in Libyan Sahara Sand, it is likely floating fabric is playing a large role in the overall behavior. The high fines content may explain the small deviation in both ϕ_c and ϕ_p for samples of Libyan Sahara sand with and without fines.

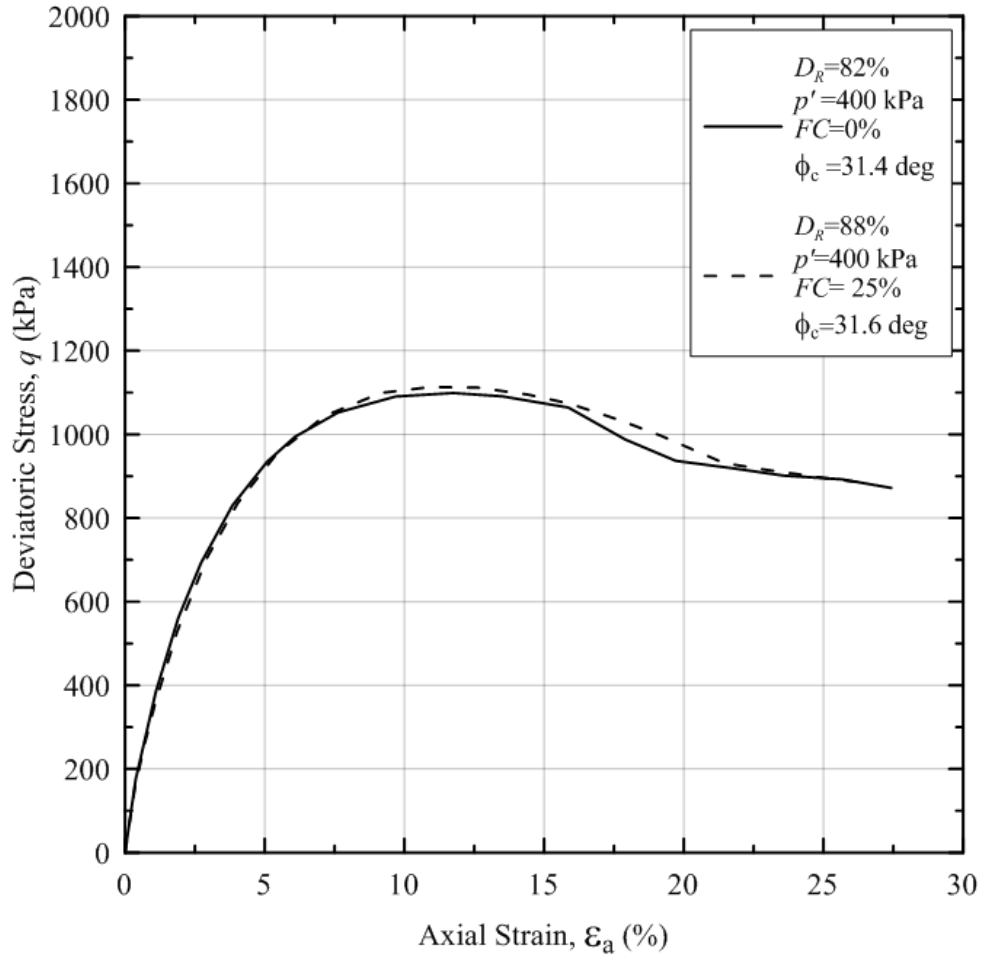


Figure 4.15 Deviatoric stress versus axial strain for consolidated isotropically drained triaxial tests. Values of p' and D_R represent the final specimen state at the end of isotropic compression, before shearing

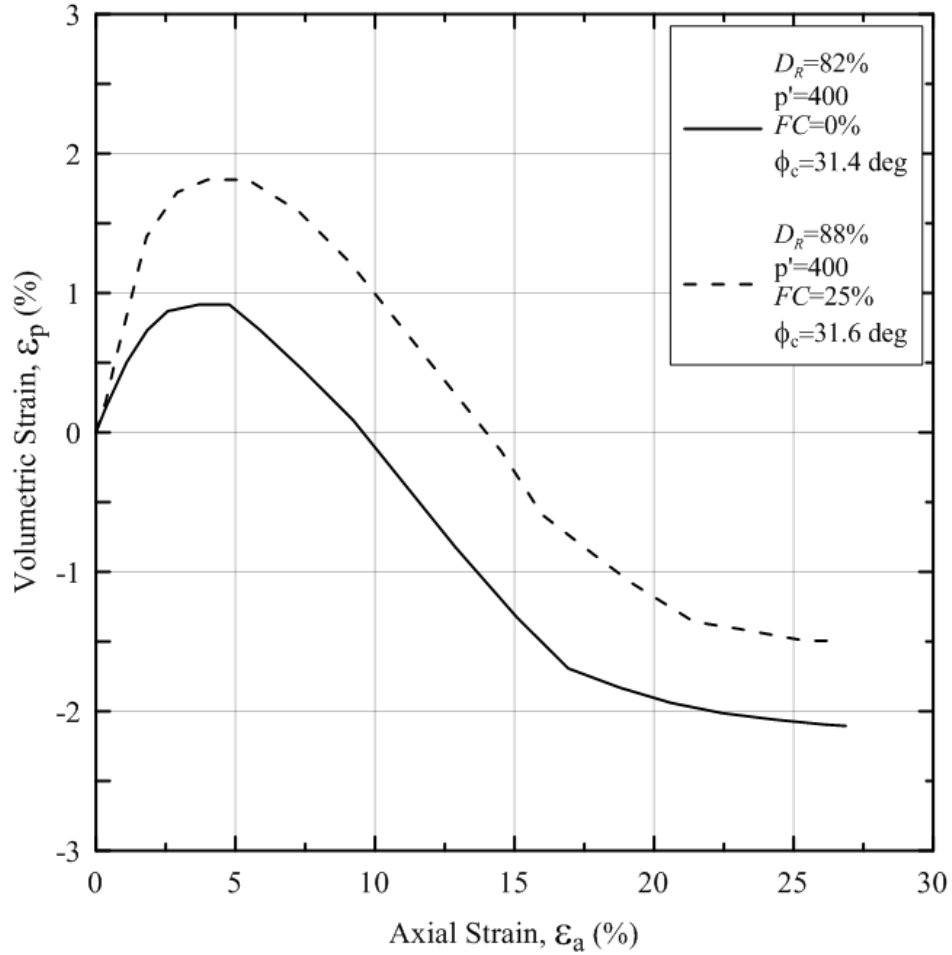


Figure 4.16 Volumetric strain versus axial strain. Values of p' and D_R represent the final specimen state at the end of isotropic compression, before shearing

4.3 Small-Strain Stiffness

Bender element testing was performed in the present study to measure the shear wave velocity V_s at various states in order to estimate the maximum shear modulus G_{\max} of the Sahara sand, as discussed in Chapter 2. Five bender element tests were carried out at five levels of mean effective stress for each state (loose, medium, and dense). The data collected for Sahara sand is shown in Table 4.7. Figure 4.17 shows the overall stiffness degradation response from very small- to large-strain ranges.

Table 4.7 Shear wave velocity and shear modulus for loose, medium, and dense specimen

p' (kPa)	Shear Wave Velocity, V_s (m/s)			Maximum Shear Modulus, G_{max} (MPa)		
	$D_R=33-54\%$	$D_R=58-74\%$	$D_R=81-96\%$	$D_R=33-54\%$	$D_R=58-74\%$	$D_R=81-96\%$
30	127.1	132.0	132.7	30.4	33.5	34.5
50	142.1	149.8	151.2	38.2	43.2	44.9
100	178.8	186.4	188.2	60.8	67.1	70.0
200	216.5	224.9	228.0	89.3	98.3	103.0
400	256.3	260.7	263.8	125.8	132.4	138.8

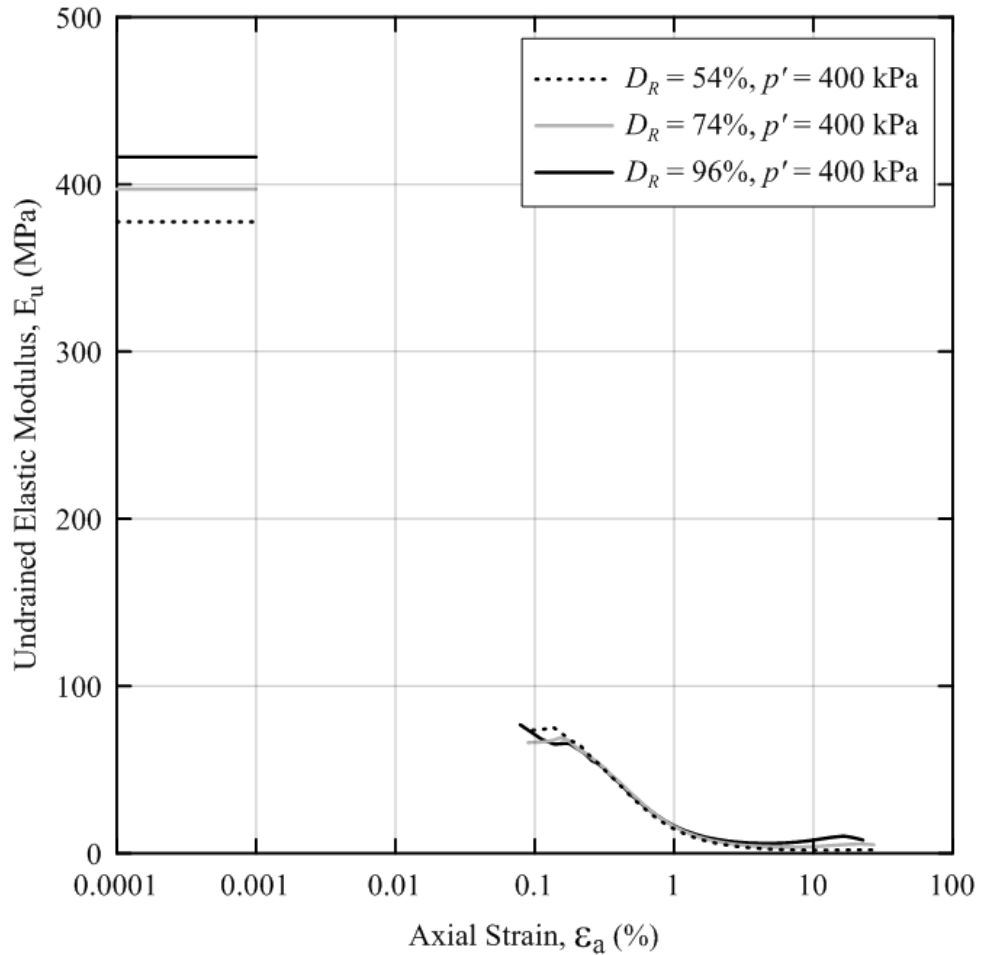


Figure 4.17 Stiffness degradation response of Libyan Sahara sand in undrained triaxial compression at mean effective stress of $p' = 400$ kPa

The shear wave velocity and maximum shear modulus were plotted against the mean effective stress as shown in Figure 4.18 and 4.19, respectively. The shear wave velocity and the maximum shear modulus increase as the mean effective confinement is increased for loose, medium, and dense specimens. Also, as density increases, both shear wave velocity and maximum shear modulus increase.

According to Salgado et al. data, Equation 4.2 was employed to fit the data from the bender element tests on Sahara sand. Research by Iwasaki and Tatsuoka (1977) indicated that $e_g = 2.17$ can be used in Equation 4.2 for a wide variety of angular and subangular sands. Thus e_g was assumed to equal 2.17, and the values of C_g and n_g in Equation 4.2 were found through regression analysis. The intrinsic variables C_g and n_g related to the very small strain stiffness of the Libyan Sahara sand were found to be equal to 548 and 0.51, respectively.

$$\frac{G_{max}}{p_A} = C_g \frac{(e_g - e)}{1 + e} \left(\frac{p'}{p_A} \right)^{n_g} \quad \text{Equation 4.2}$$

where C_g , e_g , and n_g = regression constants that depend solely on the soil (intrinsic soil variables); p' = mean effective stress = $(\sigma'_1 + 2\sigma'_3)/3$; p_A = reference stress in the same units as p' ; and e = global void ratio. Salgado et al. (2000) found that Equation 4.2 works very well for both clean and silty sand.

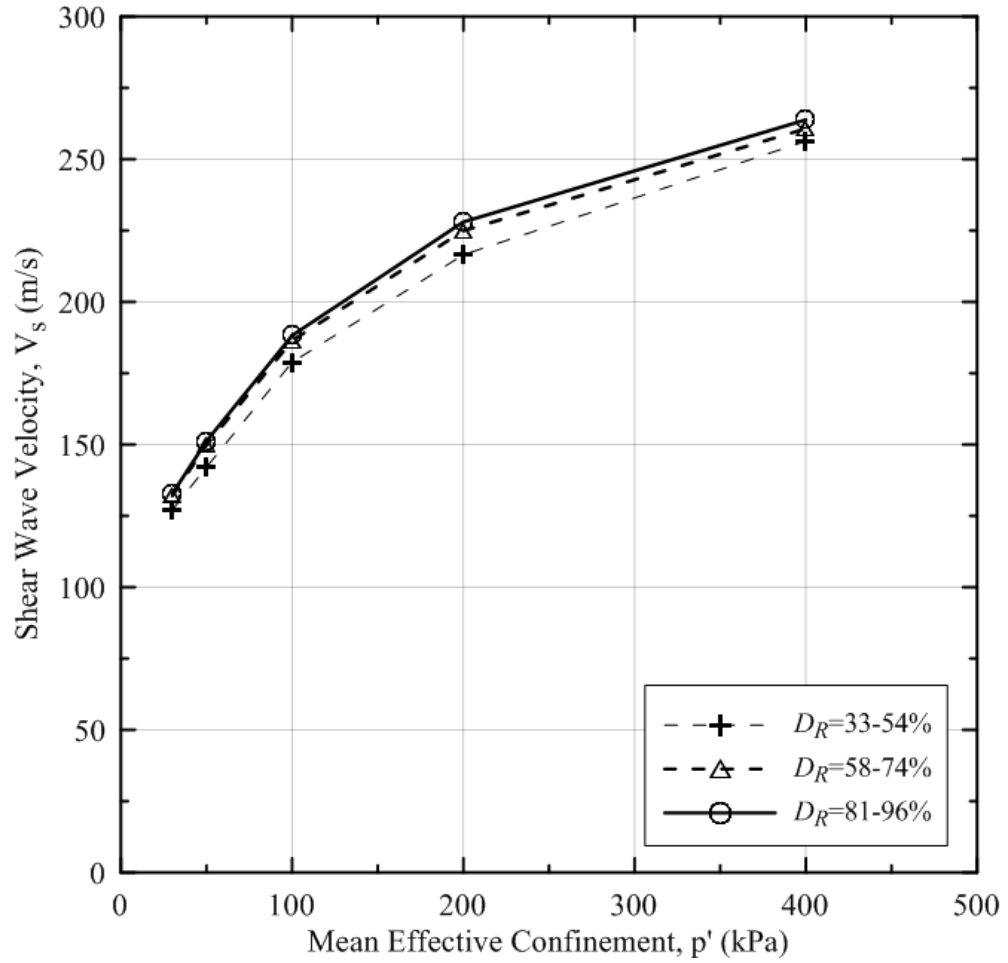


Figure 4.18 Shear wave velocities with mean effective confinement for loose, medium, and dense specimens

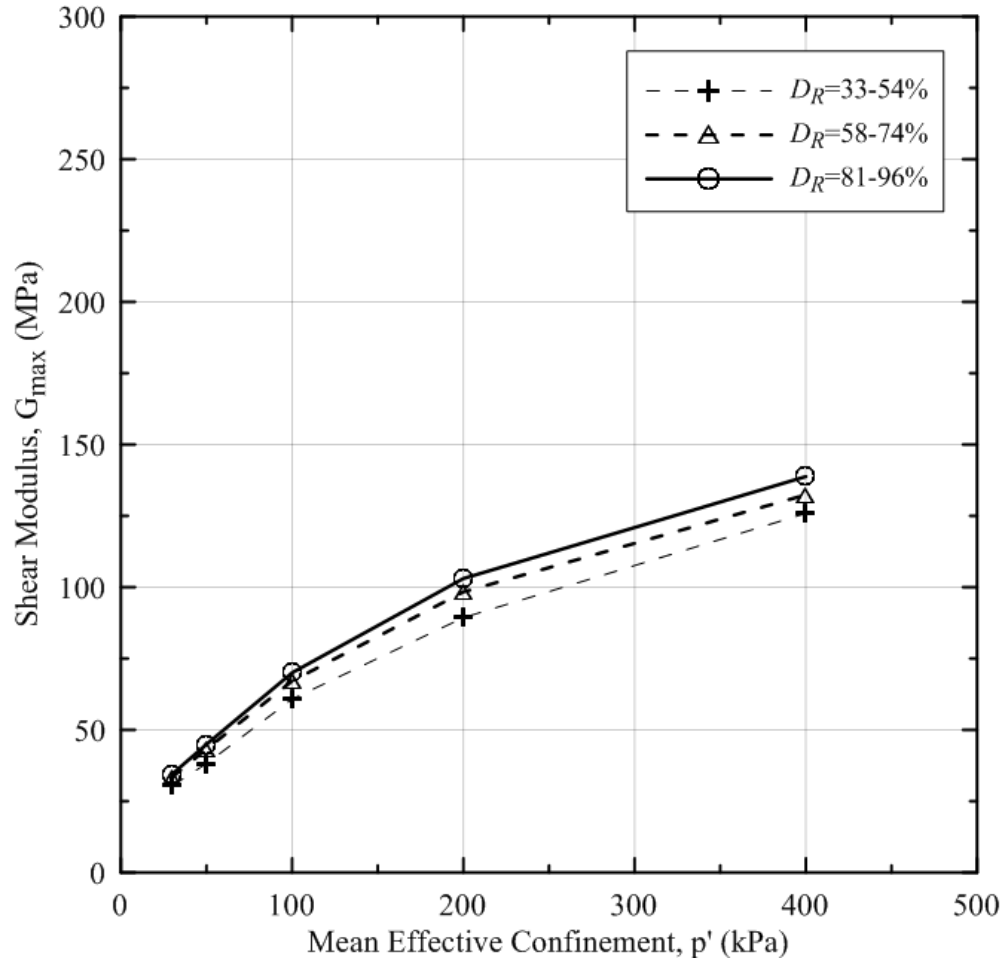


Figure 4.19 Shear modulus with mean effective confinement for loose, medium, and dense specimens

4.4 Scanning Electron Microscopy

The scanning electron microscope (SEM) was employed in the present study to observe the particle shape, surface texture, and fabric of the Sahara sand containing nonplastic silt at a microscopic level. Figure 3.5 demonstrates that the surface of Sahara sand grains is not smooth, and some of the particles are angular particles, and most of them are round to sub round particles, according to Mitchell and Soga (2005).

The experimental data of Carraro (2009) reveals that the addition of angular nonplastic silt to the host Ottawa sand increases both the peak and critical-state friction angles of the soil, which indicates that the mixture becomes more dilative than clean sand. This shows the importance of the role played by the soil fabric and structure both on the mechanical response of geomaterials and on the assessment of the amount of dilatancy for a given type of sand.

Based on the particles' shape and the type of fines, it is possible to make an educated guess about the mechanical behavior of the soil. The issue of one type of sand being more dilative than another type of sand can be attributed to particle shape and surface texture.

CHAPTER 5: CONCLUSIONS AND RECOMMENDATIONS

5.1 Conclusions

A systematic fundamental study was conducted to evaluate various aspects of the mechanical behavior of a Sahara sand from Libya. The Sahara sand used in this study was sampled and collected from Tripoli, in northwestern Libya. The sand is classified as poorly-graded sand with nonplastic silt (SM), according to the Unified Soil Classification System (USCS) (ASTM D 2487). The fines content of the sand is equal to 25%. The drained and undrained responses, small-strain stiffness, critical-state, dilatancy, and fabric of Sahara sand were studied through a variety of experimental protocols. The main conclusions taken from this study are summarized in the following sections.

5.1.1 Specimen Preparation

The Dry Funnel Deposition (DFD) technique outlined by Wood et al. (2008) was employed in this study to create homogenous and uniform specimens. The major advantages of this method are: (1) DFD is simple, yet consistent and reliable (Wood et al. 2008); (2) DFD specimens show a smaller degree of segregation (Wood et al. 2008). The method used in this study also allowed reconstitution of uniform, homogenous specimens of the silty sand tested with fabric similar to the fabric of the natural aeolian deposits in the Sahara desert. The uniformity of the reconstituted specimens was studied in terms of both D_R and FC variations across the specimen height using the collar apparatus

developed during this study. The coefficients of variation of D_R for loose specimens were about 22% and 20% for trial 1 and 2, respectively, and the coefficients of variation of D_R for dense specimen were about 2.7% and 3.1% for trial 1 and 2, respectively. The coefficients of variation of FC for loose specimens were about 2.1% and 4.7% for trial 1 and 2, respectively, and the coefficients of variation of FC for dense specimen were about 3.9% and 5.3% for trial 1 and 2 respectively. Homogeneity results show the collars apparatus to be very suitable and applicable for the successful reconstitution of uniform and homogeneous Sahara sand specimens in the laboratory.

5.1.2 Isotropic Compression

Isotropic compression results display parallel decreases in specific volume with increases of mean effective stress, dependent only on the initial specific volume, and natural log linear decreases in specific volume with varying increases of mean effective stress.

5.1.3 Drained Monotonic Response

Loose specimens show gradual increase in shear stresses as the axial strain increases (strain hardening) and tend to contract. On the other hand, dense specimens show a rapid increase in shear stress reaching a peak value at low axial strains, compared to the loose specimens, and then show a decrease in shear stress with increasing axial strain (strain softening). Dense specimens contract initially and then dilate until a critical state is attained.

As the mean effective stress increases, the loose specimens contract because the soil densifies upon shearing and the volume of the soil decreases, whereas dense specimens exhibit a relative decrease in volume expansion because work is required to cause the soil to expand against the effective confining stress. In addition, the specimen with 0% fines tends to contract less and/or dilate more with increasing axial strain than the specimen with 25% fines at the same level of D_R and p' .

5.1.4 Undrained Monotonic Response

During undrained axisymmetric compression, loose specimens exhibit an increase in excess porewater pressure (positive excess porewater pressure), while dense specimens exhibit a decrease in excess porewater pressure (negative excess porewater pressure). The changes in excess porewater pressure occur because the void ratio does not change during undrained loading and the volume of the specimens remains constant. Thus, tendencies towards volumetric deformation translate into corresponding changes in excess pore pressures.

5.1.5 Small-Strain Stiffness

The shear wave velocity and the maximum shear modulus increase as the mean effective stress is increased for loose, medium, and dense specimens. Also, as density increases, both shear wave velocity and maximum shear modulus increase, which is a typical behavior of granular materials.

5.1.6 Intrinsic Parameters of Libyan Sahara sand

Based on all drained and undrained testing conditions, the value of the critical state friction angle was found to be equal to 31.9° for Libyan Sahara sand. The critical state friction angle from drained tests is in agreement with that found from undrained tests. These results agree well with the plots of the *CSL* in $p' - q$ space which gives a value of $M = 1.28$ which is related to the value of ϕ_c for all tests.

The values of Q and R of Libyan Sahara sand were determined to be equal to 8.5 and 0.98, respectively. These values of Q and R are similar to the values presented by Bolton (1986). These values of Q and R also allow an accurate estimation (± 1.7 degrees) of the peak friction angle for Libyan Sahara sand at any given state in terms of D_R and p' . The values of the peak state friction angle for the specimens tested range from 33.6° to 35.9° .

The *CSL* in $\ln(p')-v$ space allows estimation of critical state soil parameters Γ_{cs} , k and λ_{cs} as the slope and v intercept at $p'=1$ kPa of the *CSL* (Muir-Wood 1990) and were found to be equal to 1.92, 0.0002 and 0.031, respectively.

The intrinsic variables C_g and n_g related to the very small strain stiffness of the Libyan Sahara sand were found to be equal to 548 and 0.51, respectively, while e_g was assumed to be equal to 2.17 (Iwasaki and Tatsuoka 1977).

5.1.7 Scanning Electron Microscopy

The scanning electron microscope (SEM) was employed in the present study to analyze the particle shape, surface texture, and fabric of the Sahara sand containing

nonplastic silt on a microscopic level. Figure 3.5 demonstrates that the surface of Sahara sand grains is not smooth. Some of the particles are angular particles and most of them are round to sub round particles (Mitchell and Soga 2005).

5.2 Suggestions for Future Work

According to the results from this systematic study, the following topics are suggested for future studies on the mechanical behavior of Libyan Sahara sand:

1. Investigate various specimen reconstitution techniques to characterize the monotonic behavior of Sahara sand under stress conditions.
2. Determine the correlation between in-situ test measurements (such as cone penetration resistance) and the intrinsic parameters and state variables for the Libyan Sahara sand.
3. Conduct further studies with Libyan Sahara sand from various sampling locations.
4. Evaluate stabilization techniques to enhance strength and stiffness of the tested Libyan Sahara sand. Stabilization techniques could include mixing various amounts of pozzolanic materials, such as natural clay, cement or ash.
5. Study the influence of the degree of saturation or other parameters on the behavior of the unsaturated Libyan Sahara sand.

LIST OF REFERENCES

- AL Farrah, N. A., Martens, K., Walraevens, K. (2011). "Hydrochemistry of the upper miocene-pliocene-quaternary aquifer complex of jifarah plain, NW-Libya." *Geologica Belgica*, 14/3-4, 159-174
- Anandarajah, A. (2004). "Sliding and rolling constitutive theory for granular materials." *J. Eng. Mechanics.*, ASCE 130, No. 6, 665-680.
- Anketell, J.M. and Ghellali, S.M. (1991). "Quaternary fluvio-aeolian sand, silt and alluvial gravel deposits of northern Libya - event stratigraphy and correlation." *Journal of African Earth Sciences* 13(3-4):457-469.
- Atkinson, J. H. (2000). "Non-linear soil stiffness in routine design." *Geotechnique*, 50(5), 487-508.
- Budhu, M. (2007). "*Soil Mechanics and Foundations*." John Wiley & Sons, Inc.
- Bolton, M. D. (1986). "The strength and dilatancy of sands." *Geotechnique*, 36(1) 65-78.
- Bowles, J. E. (1997). "*Foundation Analysis and Design*." Mc Graw-Hill Book Co. New York.
- Carraro, J.A.H. (2004). "Mechanical Behavior of Silty and Clayey Sands", PhD Thesis, Purdue University, West Lafayette, Indiana.
- Carraro, J.A.H., Prezzi, M. (2008) "A New Slurry –Based Method of Preparation of Specimens of Sand Containing Fines." *Geotechnical Testing Journal*, 31(1), 1-11.
- Carraro, J. A. H., Prezzi, M., Salgado, R. (2009) "Shear Strength and Stiffness of Sands Containing Plastic or Nonplastic Fines." *Journal of Geotechnical and Geoenvironmental Eng.*, ASCE, 135(9), 1167-1178.
- Casagrande, A. (1975). "Liquefaction and Cyclic Deformation of Sands - A Critical Review," Proceedings of the Fifth Pan American Conference on Soil Mechanics and

Foundation Engineering, Buenos Aries, Argentina (also Harvard Soil Mechanics Series No. 89).

Conant, L. C. & Gondarzi, C. H. (1970): Geologic Map of Libya, 1:2,000,000.- Geol. Surv. Washington.

Dyvik, R., and Madshus, C. (1985). "Lab measurements of Gmax using bender elements." *Advances in the art of testing soils under cyclic conditions*, Detroit, MI, 186-196.

Frost, J. D., Park, J.-Y. (2003). "A Critical Assessment of the Moist Tamping Technique." *Journal of Geotechnical Testing*, 26(1),1-20

GAZETAS, G. (1982). "Shear vibrations of vertically inhomogeneous earth dams." *International Journal for Numerical and Analytical Methods in Geomechanics*,6 (1), 219-241.

Ghionna, V.N., Porcino, D. (2006). "Liquefaction Resistance of Undisturbed and Reconstituted Samples of a Natural Coarse Sand from Undrained Cyclic Triaxial Tests." *Journal of Geotechnical and Geoenvironmental Engineering*, 132 (2), 194-202

Ham, A. (2007). "Libya." Lonely Planet Publications Pty Ltd, Victoria, Australia.

Hardin, B. O., and Richart, F. E. j. (1963). "Elastic wave velocities in granular soils." *Journal of Soil Mechanics and Foundation Division*, 89(1), 33-65.

Head, K. H. (1998). "Manual of Soil Laboratory Testing." Effective Stress Tests, John Wiley & Sons Ltd, West Sussex, England.

Ishihara, K. (1996). "Soil behavior for earthquake geotechnics." Oxford University Press.

Ishihara, K., Sodekawa, M., and Tanaka, Y. (1978). "Effects of overconsolidation on liquefaction characteristics of sands containing fines." *Dynamic Geotechnical Testing*, ASTM, 246-264.

Ishihara, K. (1993). "Liquefaction and flow failure during earthquakes." *Geotechnique*, 43(3): 351-415.

Iwasaki, T., and Tatsuoka, F. (1977). "Effects of grain size and grading on dynamic shear moduli of sands." *Soils and Foundations*, 17(3), 19-35.

Jang, D. J., and Frost, J.D. (1998). "Sand structure differences resulting from specimen preparation procedures." *In Proceedings of the Specialty Conference on Geotechnical Earthquake Engineering and Soil Dynamics, Seattle, Wash., American Society of Civil Engineers*, Vol. 1, PP. 234-245

Kuerbis, R., Vaid, Y.P. (1988). "Sand Sample Preparation - The Slurry Deposition Method." *Soils and Foundations*, 28(4), 107-118.

Lade, P.V., and Yamamuro, J.A. (1997). "Effects of nonplastic fines on static liquefaction of sands." *Canadian Geotechnical Journal*, 34(6): 918-928.

Mitchel, J.K. and Soga, K. (2005). "Fundamentals of Soil Behavior." John Wiley & Sons, Inc., Hoboken, NJ.

Mulilis, J. P., Chan, C. K., and Seed, H. B. (1975). "The effects of method of sample preparation on the cyclic stress strain behavior of sands." Rep. No. UCB/EERC/75/18, Earthquake Engineering Research Center, Univ. of California at Berkeley, Berkeley, Calif.

Mulilis, P.J., Seed, B.H., Chan, C.K., Mitchell, J.K., Arulanandan, K. (1977). "Effects of Sample Preparation on Sand Liquefaction." *Journal of the Geotechnical Division*, 103 (GT2), 91-108

Murthy, T. J., Loukidis, D., Carraro, J. A. H., Prezzi, M., Salgado, R. (2007) "Undrained monotonic response of clean and silty sands." *Geotechnique*, 57(3), 273-288.

Oda, M., Koishikawa, I., and Higuchi, T. (1978). "Experimental study of anisotropic shear strength of sand by plane strain test." *Soils and Foundations*, 18(1), 25-38.

Pye, K. and Tsoar, H. (2009) "Aeolian sand and sand dunes." Springer, Verlag Berlin Heidelberg, Germany.

Rowe, P. W. (1962). "The stress-dilatancy relation for static equilibrium of an assembly of particles in contact." *Proc. R. Soc.*, 500-527.

Salgado, R., Bandini, P., and Karim, A. (2000). "Shear Strength and stiffness of Silty Sand." *Journal of Geotechnical and Geoenvironmental Engineering*, 126(5), 451-462.

- Schlüter, T. (2006). "Geological Atlas of Africa, with Notes on Stratigraphy, Tectonics, Economic Geology, Geohazards and Geosites of Each Country." Berlin: Springer, 148-151.
- Schofield, A. and Wroth, P. (1968). "Critical State Soil Mechanics." Cambridge University Press, London.
- Skempton, A.W. (1954) "Pore-pressure Coefficients A and B." *Geotechnique*, 4(4), 143-147.
- Tawadros, E.E. (2001). "The geology of Egypt and Libya." A.A. Balkema, Rotterdam, 166-169.
- Thevanayagam, S., Shenthan, T., Mohan, S., and Liang, J., 2002, "Undrained Fragility of Clean Sands, Silty Sands, and Sandy Silts." *J. Geotech. Geoenviron. Eng.*, Vol. 128, No. 10, pp. 849-859.
- Vaid, Y.P., Sivathayalan, S., Stedman, D. (1999). "Influence of Specimen-Reconstituting Method on the Undrained Response of Sand." *Geotechnical Testing Journal*, 22(3), 187-195.
- Vaid, Y. P. (1994). "Liquefaction of silty soils." *Ground failures under seismic conditions*, Atlanta, GA, 1-16.
- Vaid, Y. P., and Negussey, D. (1988). "Preparation of reconstituted sand specimens." *Advanced triaxial testing of soil and rock*, 405-417.
- Vaid, Y.P., Sayao, A. (1995). "Proportional Loading Behavior of Sand under Multiaxial Stresses." *Soils and Foundations*, 35(3), 23-29.
- Viggiani, G. and Atkinson, J.H. (1995b). "Interpretation of Bender Element Tests." *Geotechnique*, 45(1), 149-154.
- Viggiani, G. and Atkinson, J.H. (1995a). "Stiffness of Fine-Grained Soil at Very Small Strains." *Geotechnique*, 45(2), 249-265.
- Wood, F. M., Yamamuro, J.A., Lade, P.V. (2008). "Effect of depositional method on the undrained response of silty sand." *Canadian Geotechnical Journal*, 45, 1525-1537.

Yamamuro, J.A., Wood, F.M. (2004). "Effect of Depositional Method on the Undrained Behavior and Microstructure of Sand with Silt." *Soil Dynamics and Earthquake Engineering*, 24, 751-760.

Yamamuro, J.A., Wood, F.M., and Lade, P.V. (2008). "Effect of depositional method on the undrained response of silty sand." *Canadian Geotechnical Journal*. J. 45: 1525-1537

Yamamuro, J.A., and Lade, P.V. (1997). "Static Liquefaction of very loose sands." *Canadian Geotechnical Journal*, 34(6): 905-917.

Yamamuro, J.A., and Covert, K.M. (2001). "Monotonic and cyclic liquefaction of very loose sands with high silt content." *Journal of Geotechnical and Geoenvironmental Engineering*, 127(4): 314-324.

Zlatovic, S., and Ishihara, K. (1997). "Normalized behavior of very loose non-plastic soils: effects of fabric." *Soils and Foundations*, 37(4): 47-56.

APPENDIX A – TRANSDUCER CALIBRATION

An intensive calibration program was carried out before the testing program began to ensure the highest quality results would be obtained with the equipment used. A summary of calibration results is presented in Table 3.1 while this appendix presents all data and results from this calibration program.

A.1 Pressure Transducers

Two pressure transducers were employed in all triaxial tests presented in this manuscript. The cell water pressure transducer was used to measure the total confining stress (σ_c) and the pore-pressure transducer was used to measure both back-pressure (u_b) and pore-water pressure (u) in all triaxial tests. Figures A.1 and A.2 show the relationship between signal voltage and the pressure applied by standard pressure measurement device. Table A.1 illustrates accuracy, resolution, excitation voltage, and calibration factors determined for each transducer.

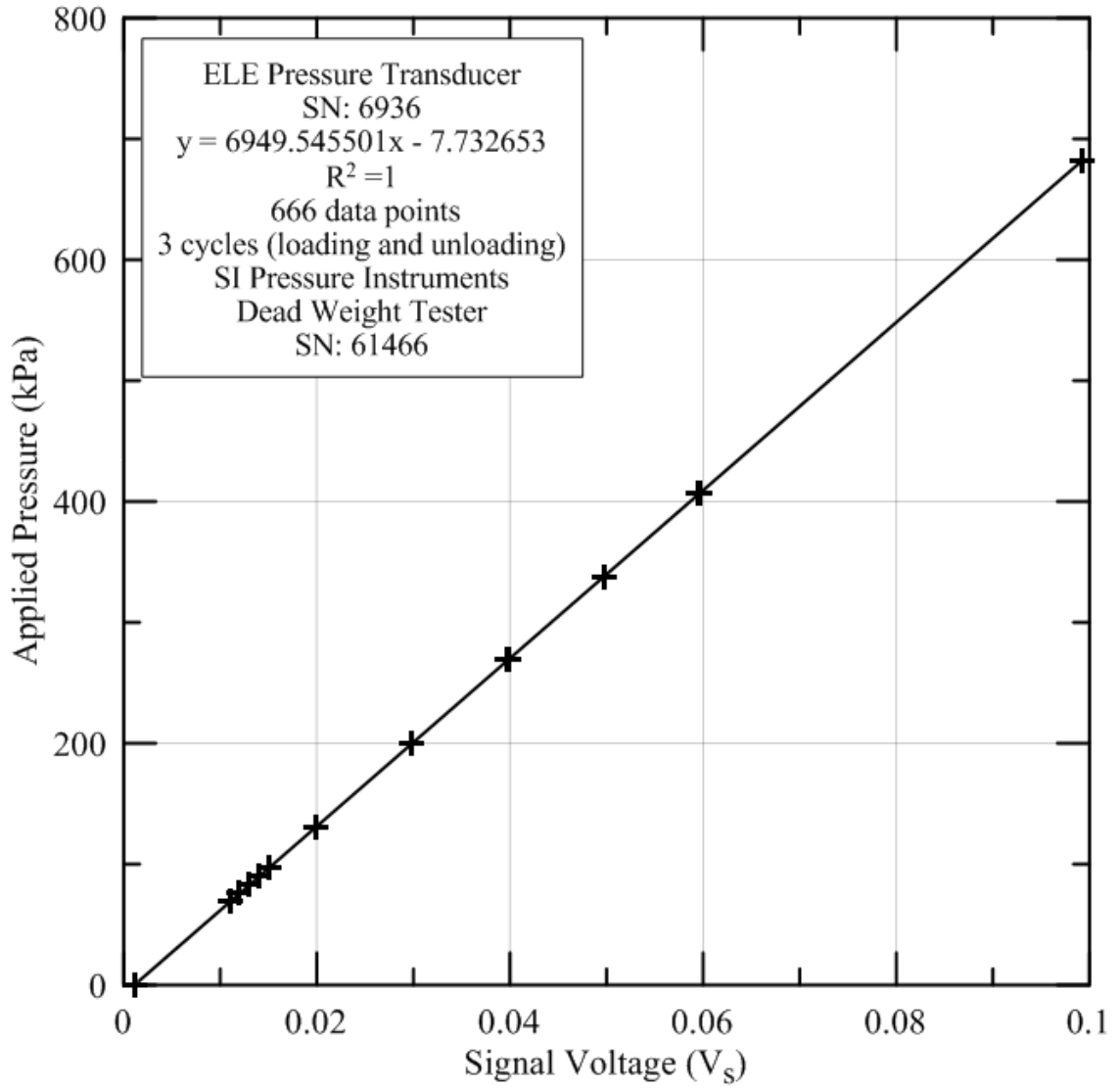


Figure A.1 Calibration plot for cell pressure transducer

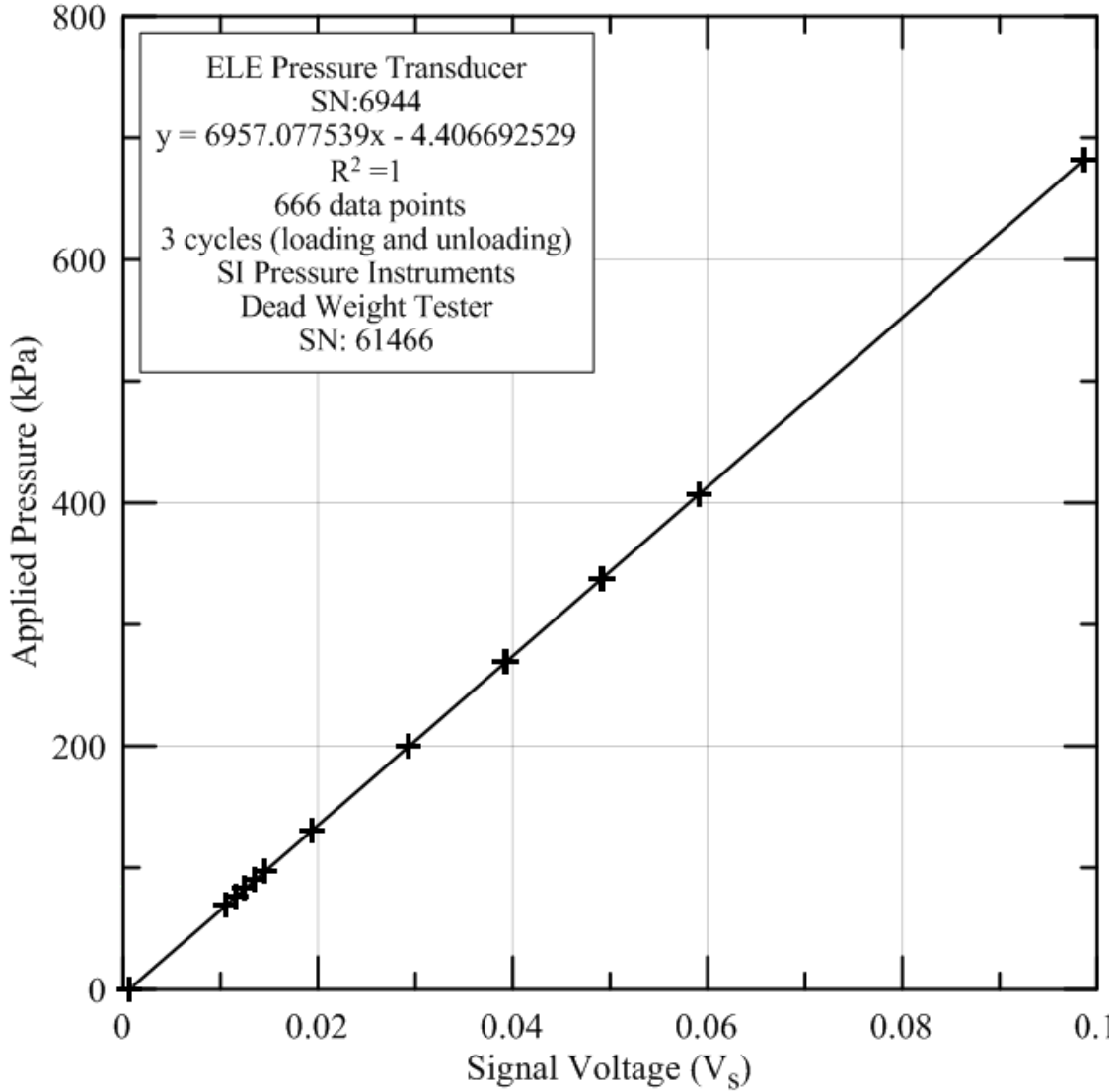


Figure A.2 Calibration plot for pore water pressure transducer

Table A.1 Pressure transducer calibration results

	Cell Pressure Transducer	Pore Water Pressure Transducer
Accuracy (%)	0.12	0.07
Resolution (kPa)	0.07	0.07
Excitation Voltage, V_e (V)	10.014	10.014
Calibration Factor (kPa/ V_s/V_e)	69592.80	69668.23

A.2 Force Transducer

In order to measure deviatoric loads applied to specimens during axisymmetric compression, a force transducer was used. Figure A.3 shows the relationship between signal voltage and the load applied by a 9-kN proving ring (See A.6.2). Table A.2 illustrates accuracy, resolution, excitation voltage, and calibration factors determined for the load transducer.

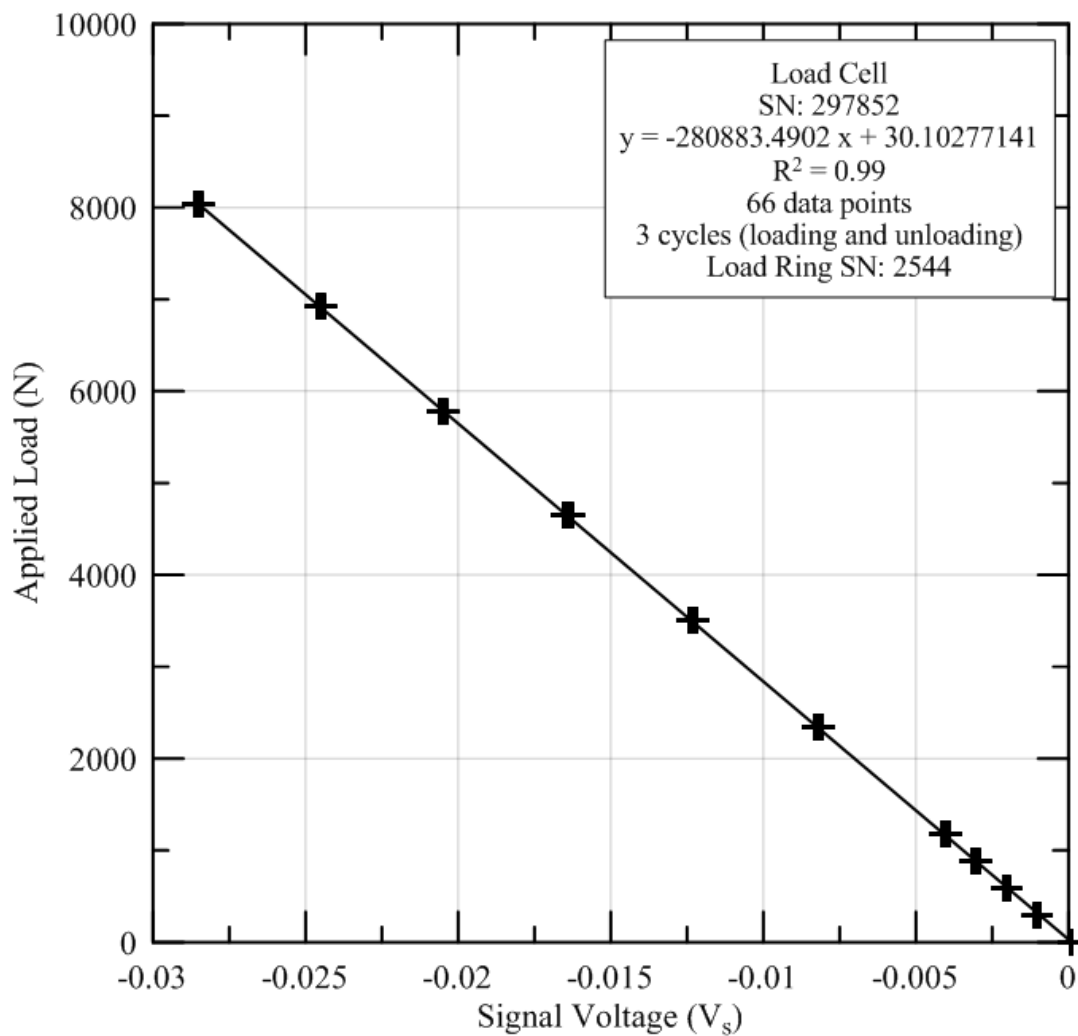


Figure A.3 Calibration plot for the deviatoric load transducer

Table A.2 Calibration data for the Deviatoric Load Transducer

Accuracy (%)	0.67
Resolution (N)	0.45
Excitation Voltage, V_e (V)	10.014
Calibration Factor ($N/V_s/V_e$)	2812770.08

A.3 Displacement Transducer

Axial displacements were measured throughout testing for all triaxial specimens presented in this study using an external LPDT (Linear Potentiometric Displacement Transducer). Figure A.4 shows the relationship between the signal voltage (V) and displacement (mm) measured by a standard displacement measurement device (See A.6.3). Table A.3 presents accuracy, resolution, excitation voltage, and calibration factors determined for the displacement transducer.

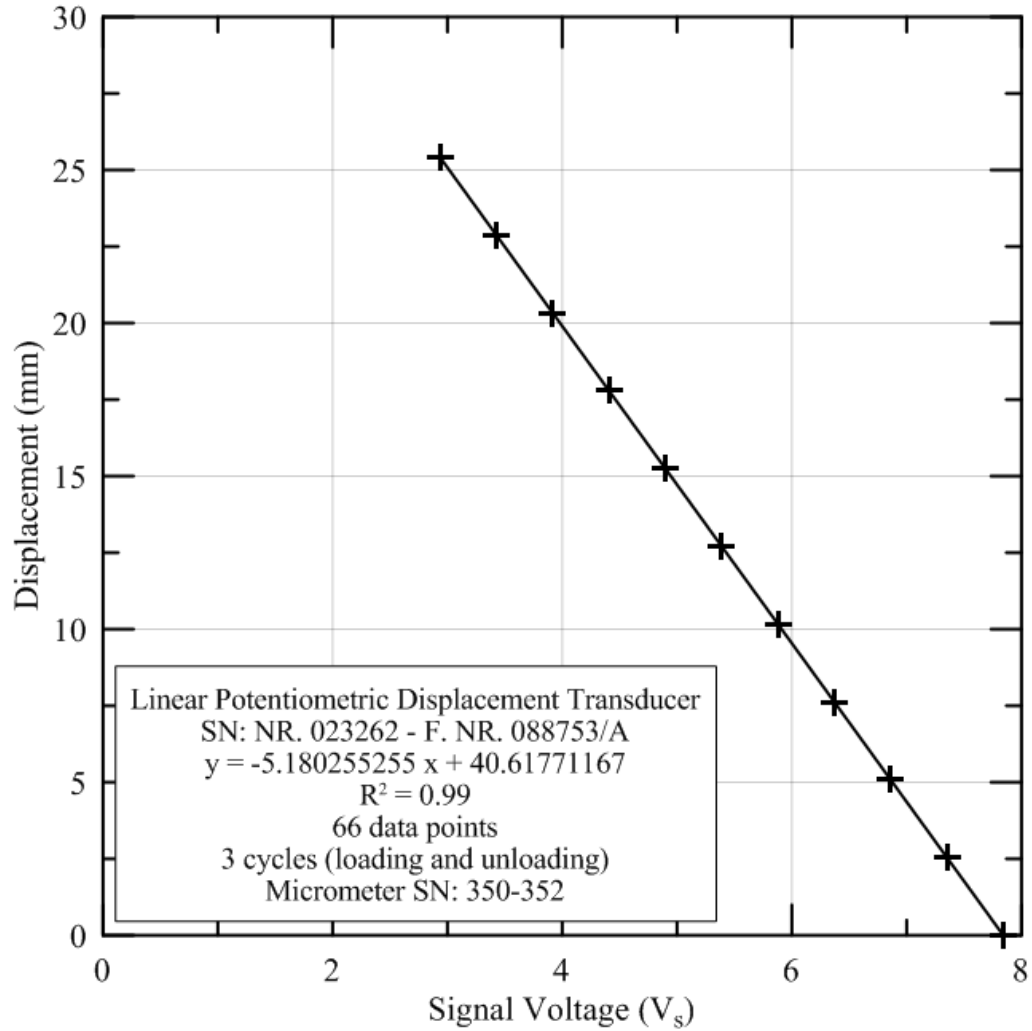


Figure A.4 Calibration plot for the axial displacement transducer

Table A.3 Calibration data for the Axial Displacement Transducer

Accuracy (%)	0.09
Resolution (mm)	0.0025
Excitation Voltage, V_e (V)	10.014
Calibration Factor (mm/ V_s/V_e)	51.88

A.4 Volume Change Transducers

Volume change burettes were employed to measure specimen volume changes during isotropic and axisymmetric compression. In order to evaluate the influence of pressure on the volume of the burette, the volumes of the burettes were calibrated at pressures of 0, 300, and 600 kPa. These tests show that change in the measured volume change due to changes in pressure applied to the burette through the air-pressure regulators is less than 0.01% of a typical specimen volume (~538 mL). Measurements were also taken over a period of 48 hours at the highest pressure levels to find how the time dependent creep might affect volume changes in the burette due to applied pressures. This data also suggests that creep in the burettes is less than 0.01 of a typical specimen volume (~538 mL).

A.5 Triaxial Cell Volume Calibration

When the triaxial cell pressure is increased, the cell walls expand. This introduces an error in the sample volume change measurements using the cell pressure line. The calibration of triaxial cell volume was conducted according to the procedure outlined in Head (1998). The cell pressure ranges from 0-700 kPa for short and long term. The time between each cell pressure increment and cell volume reading was approximately 5 minutes. Figures A.5 and A.6 present regular triaxial cell volume changes with pressure changes and time, respectively. Figures A.7 and A.8 present bender element triaxial cell volume changes with pressure changes and time, respectively.

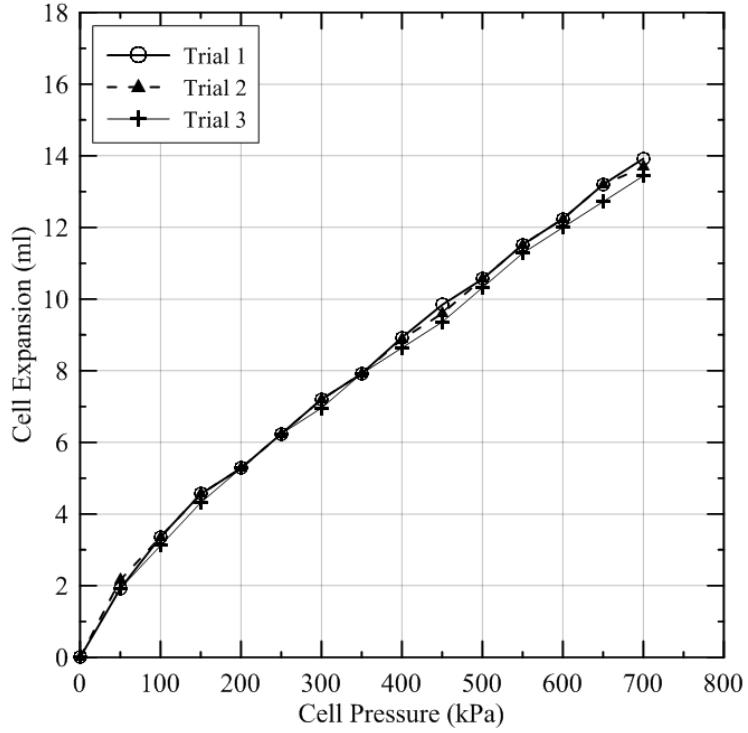


Figure A.5 Regular triaxial cell volume changes with pressure changes (short term)

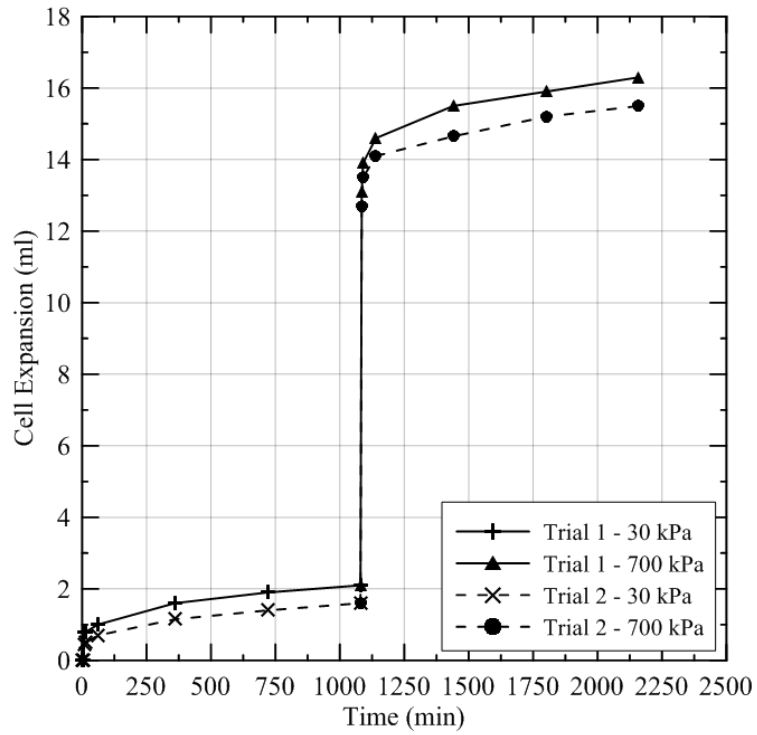


Figure A.6 Regular triaxial cell volume changes with time (long term)

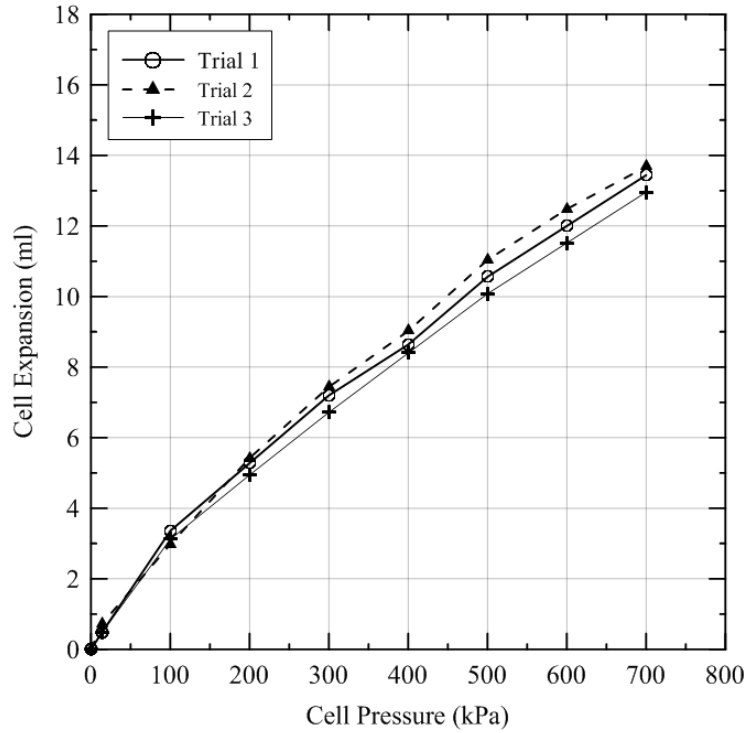


Figure A.7 Bender element cell volume changes with pressure changes (short term)

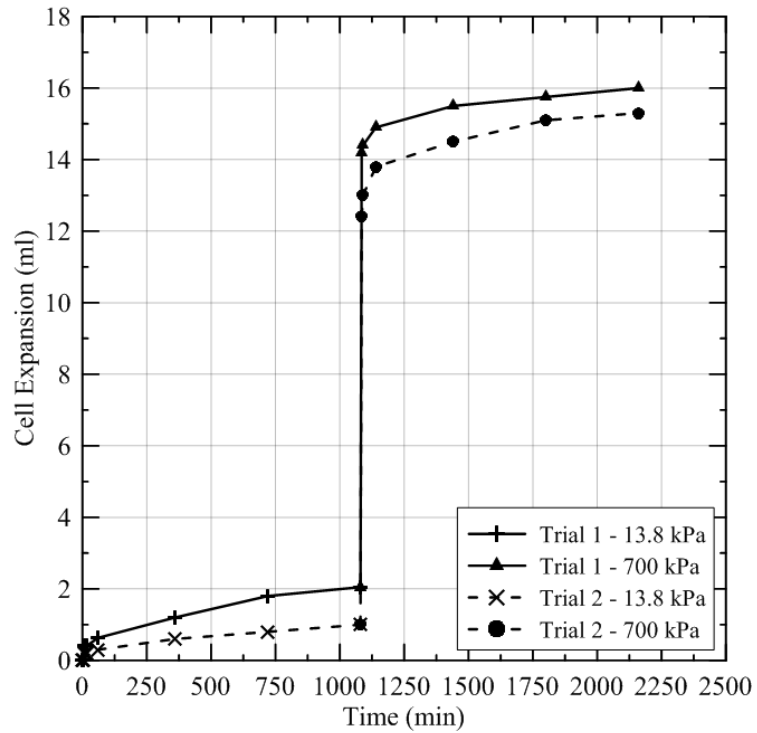


Figure A.8 Bender element cell volume changes with time (long term)

A.6 Standard Measuring Devices Used for Transducer Calibrations

The accuracy of calibration depends on the accuracy of the standard measuring device. The following standard measuring devices were employed to complete the calibrations described earlier in Sections A.1-A.4.

A.6.1 Standard Measuring Device for Pressure Transducer Calibration

Pressure transducer calibration was carried out using a 3500 kPa capacity dead weight tester manufactured by SI Pressure Instruments, UK. The accuracy of this dead weight tested is reported by the manufacturer as being equal 0.025%.

A.6.2 Standard Measuring Device for Force Transducer Calibration

Force transducer calibration was carried out using a 9-kN proving ring manufactured by Clockhouse. The accuracy and resolution of this proving ring reported by the manufacturer as being equal to 1% and 0.5 kN, respectively.

A.6.3 Standard Measuring Device for Displacement Transducer Calibration

Displacement transducer calibration was carried out using a micrometer manufactured by Mitutoyo Corporation, USA. The accuracy and resolution of this micrometer are reported by the manufacturer as being equal to 0.004% and 0.001 mm, respectively.

A.6.4 Standard Measuring Device for Volume Transducer Calibration

Volume change burettes were calibrated by determining the volume of water exiting the burette for each measurement increment. The volume change burettes contain 250 total increments and the measurement increments for calibration were 50 burette increments over the entire range of the burette (i.e. 5 data points for each burette). A linear best fit through these 5 data points gives a calibration factor which was used to convert a change in water level measured in terms of burette increments into a change in the volume of water in burette.

A.7 Elastic Modulus of Triaxial Specimen Membranes

The modulus of elasticity of the membrane used for triaxial specimen was determined according to the procedure outlined in Head (1998). Table A.4 presents the relevant dimensions of the membrane strips tested. Tables A.5 and A.6 shows the calibration data for the membrane.

Table A.4 Dimensions of membrane strips used to evaluate the elastic modulus of the membranes

	Membrane
Thickness (mm)	0.3
Width (mm)	0.0197
Area (mm ²)	0.0118
Membrane Diameter (mm)	70

Table A.5 Data used to determine the modulus of elasticity for the membrane

	Mass Applied (g)	Length (mm)	E (kPa)	ϵ (%)
Trial 1	0	33.52	-	0
	70.26	35.50	969.7	5.9
	140.56	37.82	893.3	12.1
	210.86	41.27	743.5	20.5
	281.16	43.93	738.0	25.2
Trial 2	0	34.38	-	0
	70.28	36.64	871.6	6.6
	140.58	38.95	862.2	12.5
	210.88	41.44	837.2	18.1
	281.23	44.57	773.5	24.6
Trial 3	0	33.84	-	0
	70.28	36.06	873.3	6.6
	140.56	38.70	797.9	13.5
	210.89	41.20	790.5	19.0
	281.19	44.55	724.3	26.0
Trial 4	0	33.81	-	0
	70.28	36.12	838.6	6.8
	140.55	38.70	792.2	13.5
	210.88	41.31	775.0	19.4
	281.23	44.47	727.2	25.8

APPENDIX B – Libyan Sahara Sand at Start and End of Shearing

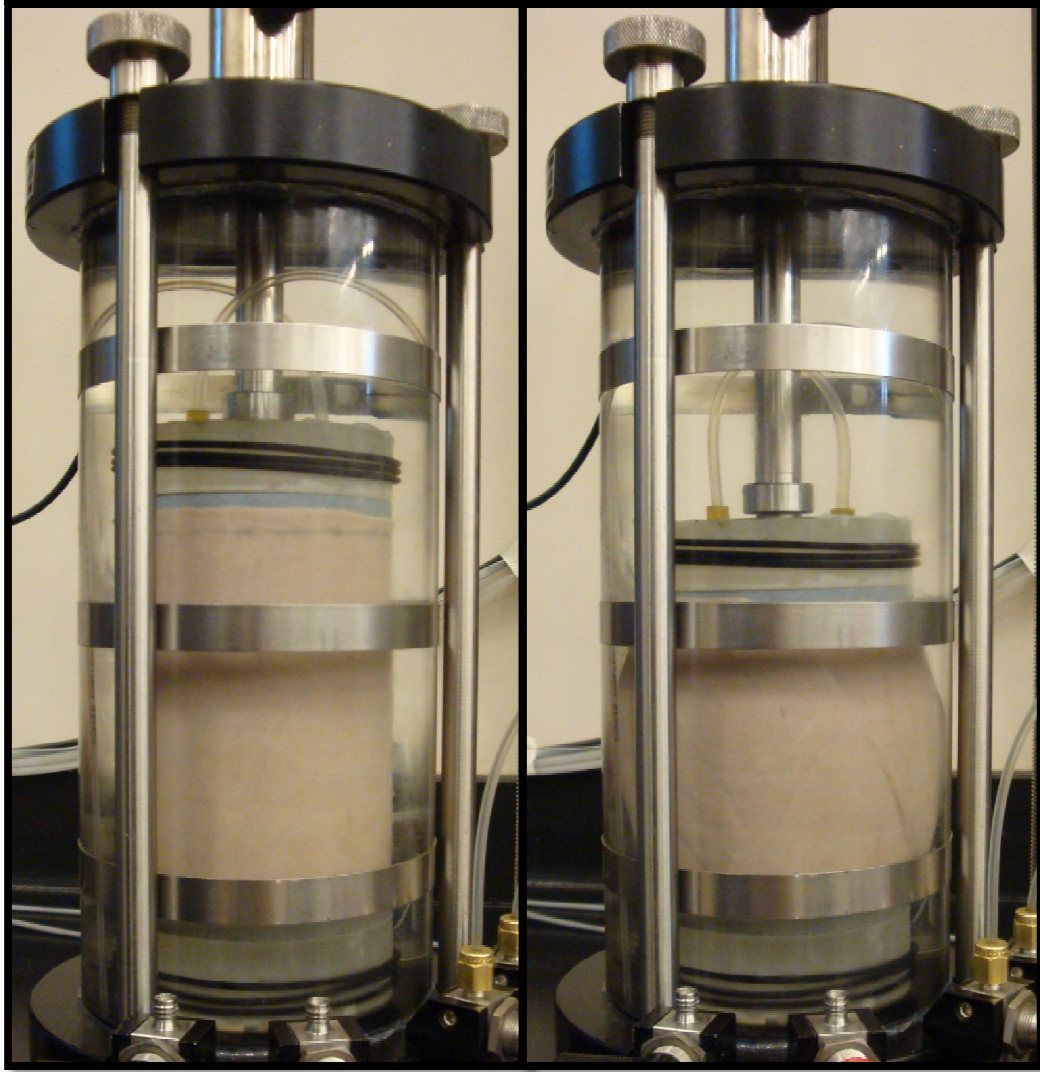


Figure B.1 Consolidated drained triaxial specimen at start and end of shearing ($D_R = 88\%$ and $p' = 400\text{kPa}$)

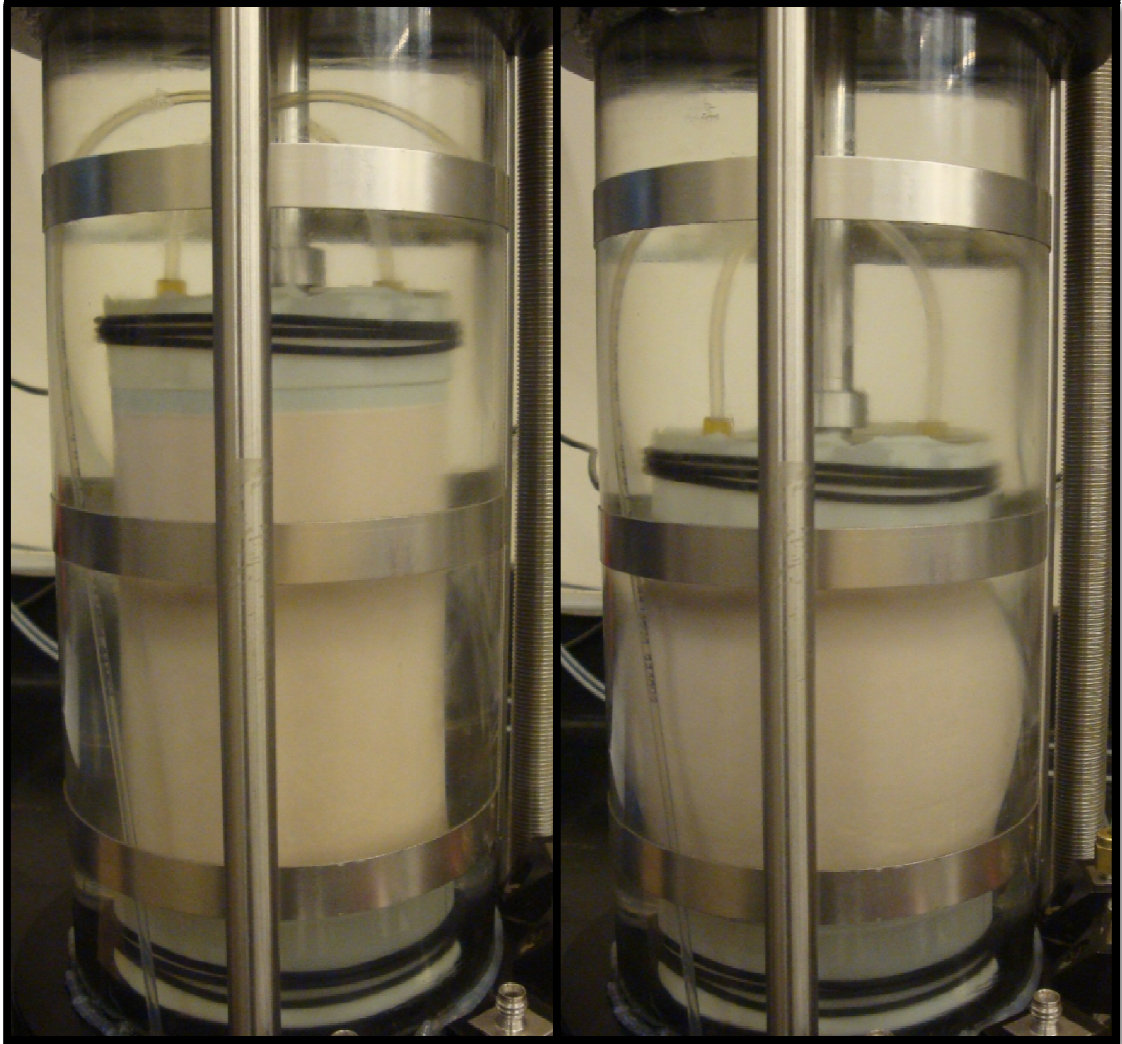


Figure B.2 Consolidated undrained triaxial specimen at start and end of shearing ($D_R = 62\%$ and $p' = 200\text{kPa}$)